Portable Atom Interferometry: Investigation on Magnetic Shielding Techniques for Compact Quantum Sensors

by

Georgios Voulazeris

A thesis submitted to
The University of Birmingham
for the degree of
DOCTOR OF PHILOSOPHY

Ultracold Atoms Group
School of Physics and Astronomy
College of Engineering and Physical Sciences
The University of Birmingham

May 2018

To my family

CONTENTS

LIST OF FIGURES

LIST OF TABLES

Abstract

Focus of this thesis are the magnetic shielding aspects of a mobile atom interferometer, developed under the Gravity Gradient Technologies and Opportunities Programme (GGtop). This system has been used as a test bed for new compact technologies with the aim to perform outdoor gravity gradient measurements. A finite element analysis model was used for optimising magnetic shielding design, aiming to reach a field attenuation factor of the order of 10^3, by mu-metal. The research was extended to alternative shielding techniques with the intention to push current technology towards next generation portable atomic sensors. Initially, Metglas foil was used to create lightweight cylindrical shielding housings. The performance goal was approached by a total of 37 foil wrappings around two coaxial cylinders. However, material inhomogeneities affected the magnetic field uniformity. The second approach exploits additive manufacturing of permalloy-80 for 3D-printing compact shielding structures. Process optimisation was undertaken by fabricating approximately 70 small bulk samples under different printing parameters, while 6 cylindrical shield prototypes were produced for preliminary shielding tests. Application of post heat treatments enhanced shielding effectiveness by a factor of up to ~ 15, indicating that a performance closer to mu-metal could potentially be reached by further process optimisation.

ACKNOWLEDGEMENTS

I would like to express my gratitude to Prof. Kai Bongs, head of the Quantum Matter Group, for the opportunity he offered me to join the Cold Atoms Group at the University of Birmingham and his guidance throughout this project. Also, I wish to thank my second senior supervisor Dr. Vincent Boyer and supervising post-docs Dr. Tristan Valenzuela Salazar, Dr. Michael Holynski and Dr. Yu-Hung Lien for their valuable every day support and advise. In addition, I would like to thank my fellow PhD students Andrew Hinton and Alexander Niggebaum for all their help and motivation during our cooperation in the lab, as well as the rest of the interferometry team. Furthermore, a lot of ideas and know-how were shared with the fellow members of the iSense team, Jonathan Malcolm, Clemens V. Rammeloo and Lingxiao Zhu. My thanks also goes to the rest of the group for the knowledge sharing and friendly environment they created.

I would also like to express my thanks to Prof. Moataz Attallah and his team at the Metallurgy & Materials department of the University, as well as Magnetic Shields Ltd. for all of their help and nice collaboration during the project on additive manufacturing.

Finally, this project has received funding from the European Unions Seventh Framework Programme for research, technological development and demonstration under grant agreement no [317485].

CHAPTER 1

INTRODUCTION AND MOTIVATION

The advances in the field of experimental atomic physics over the course of the last decades have enabled the emergence of a new field of technology based on atoms. One of the outcomes of this is the development of a new classification of sensors, referred to as *atomic sensors*. Such devices typically exploit laser cooling, trapping and manipulation of atoms for achieving high precision measurements. Atom interferometers, atomic clocks and atomic magnetometers are some examples in this category. These sensors are attributed with some significant advantages when compared to their classical counterparts.

Many classical sensors use mechanical components which are subjected to wear and mechanical tolerances. These factors resulting from repeated use cause drifts that cannot be avoided. For example, in the case of a classical gravity sensor such components could be a mechanical test mass, suspended from a spring or in free fall. In addition, measurement-critical fabricated components, like the proof masses or mechanical springs in this example, cannot be identical on an industrial scale. Therefore, the results derived from different units making the same measurement will also depend on the sum of the tolerances between each unit. In contrast, atomic sensors use atoms as test particles which have well defined properties such as mass, energy level structure and charge that do not vary or degrade over time. At the moment, atomic sensors are predominantly developed in research institutes and are mostly used in fundamental research, with a few other manufacturers [1, 7, 8] aiming towards commercial use for end-user applications. One of the most significant remaining challenges in bringing this technology to the forefront is the sufficient level of size reduction required. The way to overcome this barrier is by focusing on the development of compact components, enabling the production of atomic sensors which can be operated by a person in an outdoor environment and powered by a battery.

Most recently, a large effort has been made to encourage knowledge transfer between academia and industry and towards the transition of quantum technologies from the field of fundamental research to applications and commercialisation. For this objective, the *UK National Quantum Technology Hub in Sensors and Metrology* (QT Hub) was initiated in 2014, of which the University has the leading role. One of its main goals is to build the supply chain for component technologies and facilitate progress towards quantum sensor miniaturisation. Current work on component standardisation among QT Hub partners includes laser systems, vacuum systems and electronics, with the view of expanding this range further.

1.1 Motivation

Aim of this work is to apply the magnetic shielding technique on the mobile atomic sensor which is being developed by this team, in order to provide the appropriate protection from external magnetic fields and extend this research to next generation systems.

Certain applications require very low magnetic field environments and can be affected by the Earth's field or fields produced by other nearby sources. The Earth's magnetic field magnitude is approximately $\sim 50\,\mu\text{T}$, exhibiting perturbations by $\sim$10 nT over time and location. These perturbations are owed to various natural mechanisms in the crust, ionosphere and magnetosphere both in a daily and longer time-scale periods [25]. The magnetic field produced by various devises will add to this field, imposing challenges in the operation of a sensitive system like an atomic sensor. In particular, magnetic fields are known to cause Zeeman shifts on the internal energy levels of the atoms and magnetic forces that cause undesired accelerations. Therefore, the experimental region has to be magnetically shielded sufficiently in order to keep stray magnetic fields well controlled. Typically, this is achieved either passively, by the use of special enclosures or actively, by compensation coil systems that null the external fields in the region of interest. Depending on the nature of its source, a magnetic field can be either constant in time or time dependent. For example, a magnetic field emanating from a permanent magnet or generated by a coil that carries a direct current (DC), is commonly called *DC magnetic field* and is characterised by a constant magnitude and orientation. Similarly, a coil powered by an alternating current (AC) produces a magnetic field that oscillates with the same frequency which is called *AC magnetic field*. In many applications, slowly changing or quasi-static fields like the Earth's field are often treated as DC fields. Some typical figures of common magnetic field sources are given in tab. 1.1. However, the mechanisms involved when shielding against a DC magnetic field are different from those in the case of AC fields. For example, when an AC field interacts with a conductive material it can induce localized electric currents known as Eddy currents [55], whereas a DC field does not. Therefore, different

Source	Approximate distance [m]	Magnetic flux density [μT][1]
Geomagnetic field (DC)	Ambient	~ 50
Underground transmission line of 1 kA (DC)	1.4	<10
Escalator (DC)	1	48 - 68
Moving walkway (DC)	1	24 - 122
Fluorescent light (AC)	1	0.02 - 0.25
Computer conductive screens (AC)	0.3 - 0.5	≤ 0.7
Household appliances (AC)	1	0.05 - 0.3
Household switchboard (AC)	1 - 2	0.1
Distribution lines (AC)	15	<0.1 - 0.5
Large power lines (AC)	15	< 1 - 7
Local supply transformers - kiosk (AC)	2 - 3	0.1
Electric trains (AC)	Passengers' compartment	~ 10

Table 1.1: Common magnetic field sources with their typical magnitude levels (information sourced from [9, 48]).

shielding techniques are required for each case. Since the scope of this work is focused on passive shielding against DC magnetic fields, the techniques applied for AC fields are not examined here.

Field attenuation becomes a more challenging task in the case of portable atomic sensors which tend to exhibit complex geometries and have stringent requirements in weight and size. Shielding performance should be adequate so that the sensor can operate properly during deployment at different locations in the field, without the burden of field compensation systems. In addition, feedthroughs for tubing and wiring are commonly required, that compromise shielding effectiveness due to magnetic field leakage and fringing by the apertures.

Focus of this work is on the magnetic shielding aspects of compact atomic sensors, as part of the development of the GGtop atom interferometer, designed to be used for remote gravity sensing (see §1.3). In this perspective, a shielding design study was initially conducted to meet the GGtop system requirements. Then, the study is extended to alternative methods that could be applied to a broader range of next generation compact atomic sensors. In the first method highly permeable Metglas foil was used to build lightweight shielding housings, which has been demonstrated in literature previously but in different applications [75]. The second method demonstrates the first attempt of using additive manufacturing (AM) to 3D print compact shielding housings out of permalloy-80 [27, 83]. The latter case applies for sensors smaller than the GGtop and is mostly oriented towards the QT Hub objectives, as discussed above.

[1] 1 μT (micro-tesla) = 10 mG (milli-gauss).

1.2 Inertial Sensors

Each massive body generates a gravitational scalar potential described by

$$\Phi(\mathbf{r}) = G \int \frac{\rho(\mathbf{r}')}{|\mathbf{r}' - \mathbf{r}|} d^3\mathbf{r}' \tag{1.1}$$

where $\rho(\mathbf{r}')$ is the material density at position $(\mathbf{r}')$ and $G = 6.673 \times 10^{-11}$ $\mathrm{Nm^2kg^{-2}}$ is the *gravitational constant*. Gravity is given by

$$\boldsymbol{g}(\mathbf{r}) = \nabla\Phi(\mathbf{r}), \tag{1.2}$$

and is measured in $\mathrm{m/s^2}$ (SI) or Gal[1] (CGS). The variation of $\boldsymbol{g}(\mathbf{r})$ in space is described by the gravity gradient Γ, measured in units of Eötvös (E) which equals to 1 E $= 10^{-9}$ $\mathrm{sec^2}$ or 10^{-4} mGal/m.

Assuming a spherical body of mass $M(\mathbf{r})$ with its centre of mass fixed at $\mathbf{r}' = 0$, and whose density is a function of the radius $\mathbf{r}$ only,

$$\Phi(\mathrm{r}) = G\frac{M}{\mathrm{r}}, \quad g_\mathrm{r} = -G\frac{M}{\mathrm{r}^2} \quad \text{and} \quad \Gamma_{\mathrm{rr}} = G\frac{2M}{\mathrm{r}^3} \ . \tag{1.3}$$

Since gravity depends upon location, a reference value of $g_0 = 9.806\,65\,\mathrm{m/s^2}$ is commonly used in applications, often referred to as *"standard acceleration"*. This value is defined as the acceleration of an object due to gravity in a vacuum at mean sea level and a latitude of 45° [12].

Gravity sensors have been initially used in fundamental research to test the physical laws of gravity like the universal gravitational constant G [46, 99] and the equivalence principle [43, 104]. In addition, gravity sensing or gravimetry has proved to be a method that can provide useful information in many different fields of research which has triggered the development of transportable and portable inertial sensors, exploited in numerous applications. Many examples are found in the geophysical sector such as surveys on global climate systems and ice melting [21], geodesy [84, 100] and volcanology [22]. Furthermore, underground mapping applications in mining and resource exploration surveys [39] have found high commercial interest, as well as in civil engineering [81] for detecting underground voids and buried infrastructure lines. Finally, mobile inertial sensors can be used as integrated precise accelerometers [49] in inertial navigation systems, which have attracted the attention from the aerospace and defence industry.

Depending on the measurement method, gravity sensors can be classified in two types. *Absolute gravity sensors* perform a direct measurement of g by recording the motion of a free falling test mass, like in the

[1] 1 Gal $= 0.01\,\mathrm{m/s^2}$.

case of falling corner-mirror systems, or atomic gravimeters that use cold atoms as test masses. Their main disadvantage is the low repetition rate, however they have almost negligible experimental drifts and can be used for long term measurements. The second type is the *relative gravity sensors* which compare the gravitational force to a counterforce, like the spring force in a spring-mass system [4, 67]. These sensors exhibit high experimental drifts and need to be recalibrated in a regular basis, making them more suitable for short term measurements.

One of the first deployable gravitational devises was the torsion pendulum [42] invented by Loránd Eötvös in 1890. Today, the best accuracies achieved by large lab-based gravitational atomic sensors are of the order of $\sim 6.7 \times 10^{-6}$ mGal [115]. This value corresponds to signals produced by objects which are smaller than the human body. Typical magnitudes of environmental sources influencing a measurement of the local gravitational field are shown in tab. 1.2. Research carried out at different groups over the recent years has

Sources influencing local gravity	Order of magnitude ($\times g_0$)
Global (geoid, geographic latitude)	10^{-3}
Local (landscape, large buildings, etc.)	10^{-6}
Tidal effects (ocean loading, elastic response, etc.)	$10^{-7} - 10^{-8}$
Geophysical (tectonic movement, crustal rebound, etc.)	10^{-9}/year
Human size objects (vehicles, human body, etc.)	$10^{-8} - 10^{-9}$

Table 1.2: Examples of sources that influence measurements of local gravity with magnitudes relative to g_0 (approximate values sourced from [93]).

achieved a considerable advancement towards mobile atomic sensors, which have demonstrated comparable or better results from their classical competitors. Some examples of relevant mobile atom interferometers are the GAIN in Berlin [102], the experiment at ONERA [17] and CAG at LNE-SYRTE [78] in France, the work demonstrated at Stanford [127] and groups in China like in [126].

1.3 GGtop Consortium

The current experiment was initiated by the *Gravity Gradient Technologies and Opportunities Programme* (GGtop), which is a multidisciplinary consortium involving partners from Physics, Electrical, Mechanical and Civil Engineering as well as Archaeology. Aim of the programme is to develop a mobile gravity gradient sensor based on cold atoms to evaluate its potentials in the field of underground mapping surveys. The range of potential applications includes fundamental research, urban infrastructure, seabed inspection, mining, archaeological surveys, and others. The gravity signals that correspond to such applications are typically below the level of $10^{-7} g_0$ (see tab. 1.2). In particular, in the case of small targets such as buried pipes and

cables, the signals are lower than $10^{-9}g_0$. Therefore, the gradiometer developed should be sensitive at signals below 10 E[1], with the ambition of reaching a sensitivity level of $\sim 1\,\mathrm{mE}/\sqrt{\mathrm{Hz}}$.

A system like GGtop is expected to be sensitive to a number of different noise sources which can affect its operation. External magnetic fields are one of the factors of the highest impact, since they can interact with the atoms and therefore proper magnetic shielding becomes an important aspect of this experiment.

1.4 Thesis Organisation

The material of this thesis is organised as follows. Initially, a theoretical introduction to the fundamentals of the atomic sensor is given in Chapter 2, while Chapter 3 describes the initial GGtop apparatus, along with some representative results of its current status. Then, the next two chapters are dedicated to magnetic shielding, which is the main focus of this work. In particular, Chapter 4 presents a brief theoretical introduction in magnetic shielding and properties of ferromagnetic materials, accompanied with numerical simulations and results from the initial magnetic tests on the GGtop magnetic shield. The findings from a second level study are being discussed in Chapter 5, where Metglas and additive manufacturing are being investigated as alternative shielding methods. Finally, Chapter 6 provides an overall summary of the previous content, along with a discussion on future steps and prospects.

1.5 Contribution Statement

The numerical simulations and magnetic shielding experiments shown in Chapters 4 and 5 are the author's personal work. Research related to the 3D-printing was in collaboration with the Metallurgy & Materials department of the University. The author's contribution was the CAD design of the shield prototypes and magnetic shielding tests, as well as the majority of the magnetic characterisation of the small samples on VSM and analysis. The production, structural characterisation and HIP treatment were undertaken by the collaborating team, while the final sample heat treatment was offered by Magnetic Shields Ltd. (MSL) who joined the project during the final stage.

In parallel to the above work, some contribution to the cold atoms experiment was also made as part of the author's involvement to the GGtop project team. This was mainly focused on the physics package of the system and includes magnetic shielding, the design of new modular bases for the 2D-MOT telescopes and

[1] 1 E corresponds to a signal produced by a 10 cm diameter source of 1 kg at a depth of approximately 1 m.

3D-MOT compensation coils. Involvement in other aspects includes some parts of the code for the computer control interface and repairs on electronics and the laser distribution system.

CHAPTER 2

THEORY

2.1 Fundamentals of Laser Cooling

2.1.1 Atom Cooling

Laser cooling [47, 80] is a method of atom deceleration using near resonant light, based on a successive absorption and emission process, demonstrated for a first time by WD Phillips (Nobel Prize in 1997) [94].

Figure 2.1 shows a simplified model describing light scattering by an atom with two energy levels, travelling along a light field. Assuming that the light-field is close enough to the atomic resonance, the atom can go through successive cycles of excitation and de-excitation between these two levels. Starting from the ground level, as the atom absorbs a photon from the applied light field, it will be excited to the upper level while at the same time it receives a momentum kick along the direction of the incident light beam. It will then stay in this state until it de-excites spontaneously to the ground level, by emitting a photon in a random direction. As the atom travels against the light, it will go through multiple transitions by this process and receive a net deceleration along the axis of the incident light beam.

The above scattering mechanism is being used in a technique which is well established in cold atom experiments, known as the *optical molasses*. Aim of this technique is to create a region where the atoms get decelerated or "cooled" and takes its name due to its resemblance to a viscous medium that would damp the motion of a moving particle. In this process, the atom is placed between two counter-propagating laser beams of the same frequency, which is shifted to slightly below the atomic resonance. Due to its motion relative to the light field, the atom will "see" the frequency of the opposing beam Doppler shifted towards resonance. Similarly, the beam that the atom travels away from, will be shifted further away from resonance.

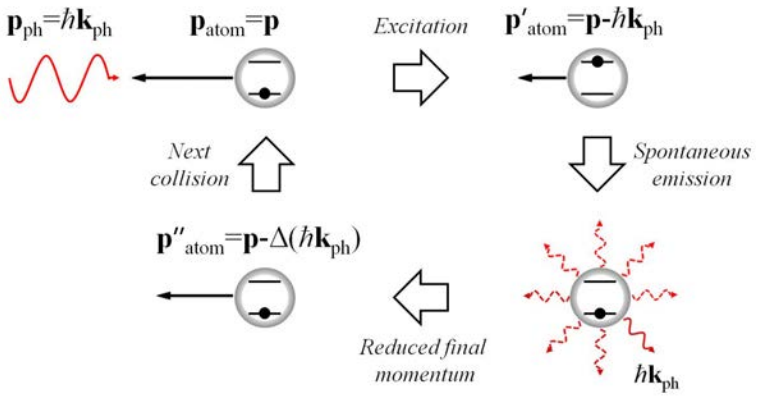

Figure 2.1: Schematic representation of the momentum exchange between an atom and the incident photons from a near resonant light field.

As a result, photons travelling against the atom will have a higher probability to be scattered compared to those travelling in the same direction. After multiple scattering events, this imbalance will create a net push against the atom's velocity and will eventually decelerate it. This mechanism constitutes a damping force (see fig. 2.2) exerted on an atom moving between the two counter-propagating beams, in the form [80]

$$F_{\text{molass.}} = -\alpha u, \tag{2.1}$$

where u is the atom velocity and α is the damping coefficient which relates to the scattering rate and momentum transfer. By using three orthogonal counter-propagating laser beams instead of one, the above

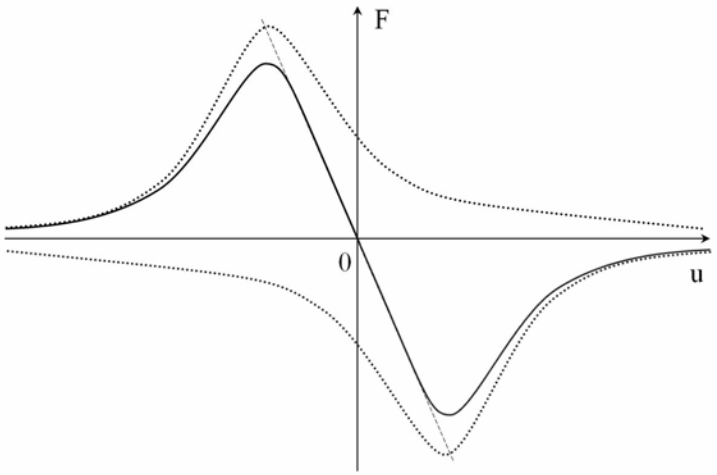

Figure 2.2: Velocity dependent force for one–dimensional optical molasses. The produced forces from the counter-propagating laser beams (doted curves) form a damping force (solid curve) over a certain velocity range.

scheme can be extended to three dimensions. In this case, atoms moving within the laser beam overlap region will experience a deceleration in all three directions.

However, cooling is not the only effect on the above mechanism. The average kinetic energy change over a photon absorption is equal to $E_{\mathrm{r}} = \hbar\omega_{\mathrm{r}}$, also known as the *recoil energy* [80]. The laser beams introduce a mechanism on the atoms which stems from the randomness in the atom recoil direction and is always in competition with the above damping effect. This sets a limit to the cooling mechanism, known as the *Doppler limit* [29, 80], which is typically of the order of $\sim 10^2$ μK and is given by

$$\mathrm{T_D} = \frac{\hbar\Gamma}{2k_{\mathrm{B}}}, \tag{2.2}$$

where k_{B} is the Boltzmann's constant and Γ is the linewidth or inverse lifetime of the atomic excited state.

2.1.2 Atom Trapping

According to the above technique, atoms interacting with an optical molasses will eventually lose a fraction of their initial momentum after multiple scattering events, however they will not be confined in space due to absence of a spatially dependent trapping force. In order to achieve this, a local magnetic field is being introduced to the above scheme, creating a configuration known as the Magneto-Optical Trap (MOT) [47].

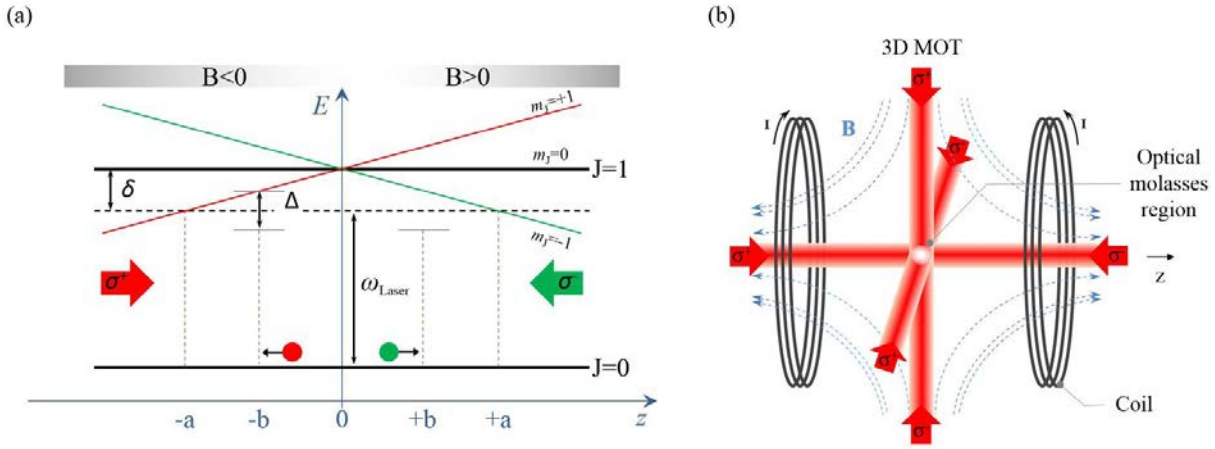

Figure 2.3: (a) Position dependent Zeeman effect caused by a linear magnetic field gradient **B** (z) to realize a magneto optical trap. The counter propagating laser beams are detuned by δ relative to an atom at rest. An atom moving against either of the two laser beams will see a Doppler shift of Δ, respectively (schematic not in scale). (b) Basic schematic of 3D–MOT scheme, consisting of three pairs of circularly polarised counter–propagating laser beams that create the optical molasses. A pair of anti–Helmholtz coils produces a quadrupole magnetic field with its minimum amplitude at the trap centre.

A schematic representation of the 1D-MOT scheme is presented in fig. 2.3 (a), where the atom is placed

between two counter-propagating beams of circularly polarised light. The beam with positive polarisation σ^+ drives the $\mathrm{m_J} = +1$ transition while the one with σ^- drives the $\mathrm{m_J} = -1$, respectively. A pair of anti-Helmholtz coils creates a magnetic field gradient $\mathrm{d}B/\mathrm{d}z$ in the molasses region, which is zero at the centre $z = 0$ and increases linearly in magnitude when moving away from it. Both laser beams are detuned below the atomic transition by δ so that an atom moving towards the right beam will have a higher probability in scattering photons coming from the right beam compared to the opposite, as before. However, the presence of the magnetic field gradient will cause an energy shift to its non-zero magnetic sub-levels due to the *Zeeman effect* [47] described by

$$\Delta E = g_{\mathrm{L}} \mu_{\mathrm{B}} \mathrm{m_J} \mathrm{B}, \tag{2.3}$$

where g_{L} and μ_{B} are the Landé factor and Bohr magnetron, respectively (see §2.5.2). Assuming an atom moving away from the trap centre along the $z > 0$ semi-axis, it will experience a position dependent Zeeman shift so that the $\Delta \mathrm{m_J} = -1$ transition will be shifted closer towards resonance, favouring the absorption of photons from the counter-propagating beam which has σ^- polarisation. This will result in a restoring force that pushes the atom back, towards the MOT centre which is given by [47]

$$F_{\mathrm{MOT}} = -2 \frac{\partial F_{\mathrm{scatt.}}}{\partial \omega} (\mathrm{k}u + \beta z) = -\alpha u - \frac{\alpha \beta}{\mathrm{k}} z, \tag{2.4}$$

where ω is the light field angular frequency, α is the radiative force damping coefficient and $\alpha\beta/\mathrm{k}$ the corresponding spring constant of the magnetic restoring force, with $\beta = \frac{g \mu_{\mathrm{B}}}{\hbar} \frac{\mathrm{d}\mathbf{B}}{\mathrm{d}z}$. The same mechanism will act on an atom moving in the opposite direction where photons coming from the beam with the σ^+ polarisation will be favoured, again pushing the atom towards $z = 0$. The above configuration can be expanded in three dimensions, as represented in the schematic in fig. 2.3 (b).

2.1.3 Sub–Doppler Cooling

One of the experimental techniques used to achieve temperatures bellow the Doppler limit is based on a light polarisation gradient configuration which perturbs the atomic energy sub–levels via the AC Stark effect [34, 47]. Heavy atoms have a complex energy structure with several Zeeman sub-levels (see §2.5.2). Alkali metals fall into this category and are widely used in cold atom experiments.

Initially, a standing wave is formed by two counter–propagating laser beams of orthogonal linear polarisations (lin.⊥lin.). The polarisation of the resulting light field will vary along its path, depending on the relative phase between the original beams. Assuming a starting point with linear polarisation, it changes to

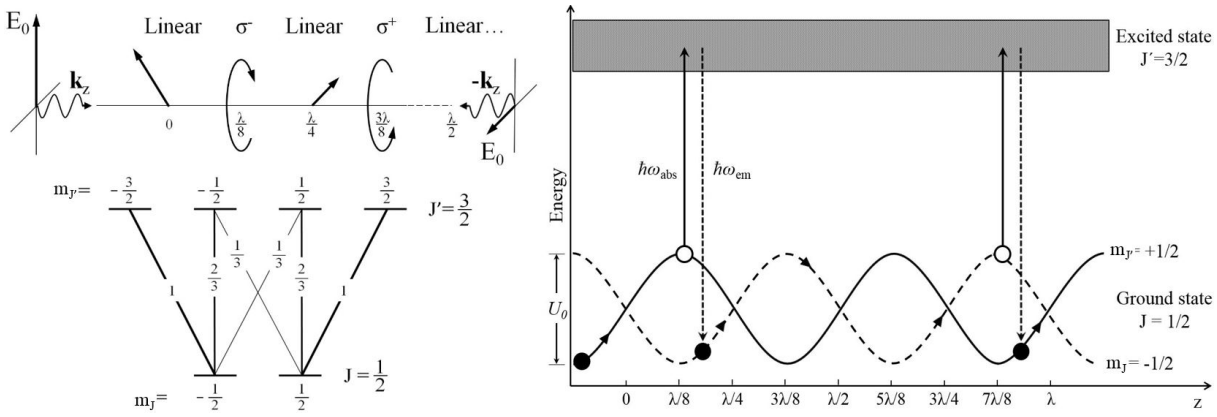

Figure 2.4: (Upper left) Polarization gradient within a standing wave formed by two counter–propagating laser beams of lin.⊥lin. polarisation. Depending on their relative phase difference, the local polarization interchanges between linear and circular within a distance of $z = \lambda/8$. (Lower left) Transition diagram between $J = 1/2$ and $J' = 3/2$ levels indicated by the corresponding coefficients. Light of σ^+ and σ^- polarisation excites transitions by $\Delta m_J = +1$ and $\Delta m_J = -1$, respectively. (Right) Representation of the Sisyphus cooling mechanism for an atom going through the light polarization gradient. The two ground states are perturbed by AC Stark shifts forming a periodic potential. The atom is pumped to J' level from the top of the potential hill and decays at the valley by spontaneous emission with a loss in kinetic energy of $\sim U_0$ (diagrams not in scale).

circular σ^-, then to linear again and finally becomes circular σ^+, in a periodic pattern (see fig. 2.4). If an atom goes through this standing wave, the electric field will cause Stark shifts on its energy sub-levels by $U(z)$, inducing a periodic modulation on its energy level states. As a result, the atom has to go through successive potential hills and valleys, interchanging its potential energy with kinetic energy.

Atomic states related to angular momentum are excited by circularly polarised light, with σ^+ and σ^- radiation exciting transitions by $\Delta m_J = \pm 1$, respectively. Figure 2.4 shows an example of a $J = 1/2$ to $J' = 3/2$ transition, where an atom with initial state $m_J = +1/2$ at $z = 0$ has to climb a potential hill while approaching point $z = \lambda/8$. The polarisation at this point becomes σ^- which can excite the atom in $m_{J'} = -1/2$. From this state, the atom can decay into either $m_J = +1/2$ or $m_J = -1/2$. In the first case, the atom will return to the same potential hill and the process restarts without any change in its total energy. However, if it de–excites into $m_J = -1/2$, then the emitted photon will translate to a higher energy than the absorption by roughly U_0, since this level corresponds to the potential valley. The same mechanism applies at a position of σ^+ polarisation where transitions follow the opposite direction. This dissipative process is known as *Sisyphus cooling*, where the atom ends up with a significantly lower kinetic energy after multiple transition cycles, until it cannot climb the potential hill any more. As a result, atoms in a standing wave are

characterized by a kinetic energy close to U_0. It is shown that this relates to temperature as [47]

$$k_{\mathrm{B}}\mathrm{T} \propto U_0 \frac{I}{|\delta|}, \tag{2.5}$$

where I is the radiation intensity. At some point, the above process is balanced by the recoil energy E_{r} due to spontaneous emission.

In the above mechanism, it is essential that the atom's quantization axis is well defined along the standing wave for the effect to work properly. Also, similar to electric fields, stray magnetic fields can also perturb the atomic states via the Zeeman effect. As a result, a Zeeman shift comparable to U_0 will affect the cooling process. For instance, a magnetic field of $\sim 10\,\mu\mathrm{T}$ can result to an energy shift that corresponds to a temperature of a few µK. Considering that the geomagnetic field is of the same order of magnitude, it indicates the importance of shielding such experiments from stray magnetic fields.

Experiments like the GGtop use circularly polarised light to create the MOT. This configuration introduces a different type of cooling mechanism which is known as σ^+-σ^- *polarisation gradient cooling* [34] and is briefly described in the following. The σ^+-σ^- light beam configuration forms a linearly polarised light field everywhere in the space between the counter-propagating light beams. The electric field vector has a constant amplitude and rotates around the light propagation axis by a 2π angle over a distance of one wave-length λ (see fig. 2.5). In contrary to the Sisyphus cooling mechanism, the Stark shift that is induced on the travelling atoms in this case is constant in space. In the steady state, atoms align their magnetic moment with the current polarisation orientation inside the light field, while the magnetic sub–levels of the ground state are populated in a symmetrical way, where the $\mathrm{m_f} = 0$ sub–level possesses the highest population, due to the selection rules (see §2.4). Therefore, an atom scatters photons from each beam with the same probability and no net force is produced. An example of the sub–levels of a $\mathrm{J} = 1$ and $\mathrm{J} = 2$ system is shown in fig. 2.5, where $|g_i\rangle$ and $|e_i\rangle$ denote the i-th ground and excited sub-levels, respectively. However, when moving inside the light field produced by the σ^+-σ^- polarisation configuration, the quantisation axis of the atoms is constantly rotating, forcing the population of the atomic states to redistribute according to the new "local" steady state distribution. This process creates a lagging of the population across the ground magnetic sub-levels, causing atoms travelling toward the σ^+ beam to have an increased probability to be transferred in the $\mathrm{m_F} = +1$ ground sub–level and equally, those moving toward the σ^- light to populate the $\mathrm{m_F} = -1$ state. This will result in an imbalance in the population distribution among the atomic sub-levels that constitutes a differential scattering force. This force is motion sensitive and cools the atoms to a temperature that is

given by [34]

$$k_{\mathrm{B}}\mathrm{T} = \frac{\hbar\Omega^2}{|\delta|}\left[\frac{29}{300} + \frac{254}{74}\frac{\Gamma^2/4}{\delta^2 + (\Gamma^2/4)}\right], \tag{2.6}$$

where Ω is the Rabi frequency which is discussed in the next section.

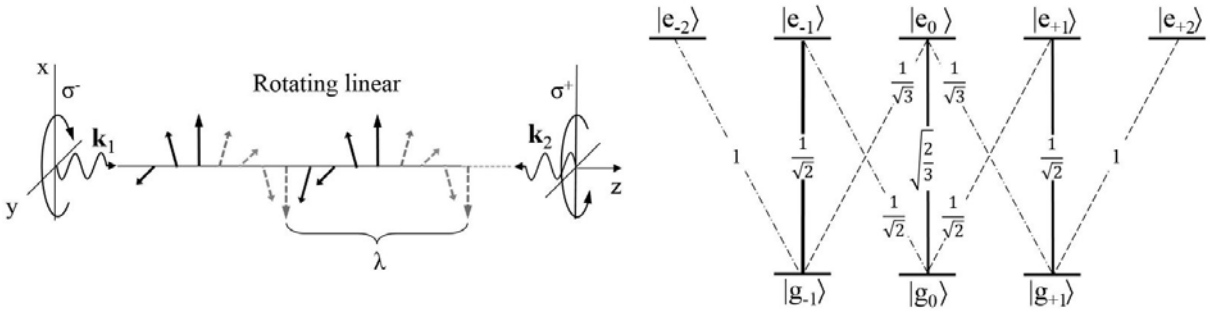

Figure 2.5: (Left) Polarization gradient within a standing wave formed by two orthogonal counter–propagating laser beams of σ^+-σ^- polarisation. The resulting light field is of linear polarisation everywhere in space, with a constant intensity but rotates around the propagation axis by a 2π angle over one wave-length. (Right) Example scheme of ground and excited state sub-levels, indicated by the corresponding transition coefficients.

2.2 Atom Interferometry

A very common method practised in metrology for precise measurements is *interferometry* [51]. It relies on the wave properties of light and in particular the interference phenomenon. Many different experimental interferometer configurations have been demonstrated throughout the years such as the Fabry-Perot [53] and Michelson [82]. Figure 2.6 shows a scheme known as the Mach–Zehnder interferometer [129], consisting of two pairs of a 50:50 beam-splitter and a mirror, along with two photo-detectors. The incident beam is initially split in two components of equal power, forming two branches. The two beams are guided with the aid of the mirrors and recombined at the second splitter. Finally, the two output beams are detected by the sensors at the output of the interferometer. In the ideal case where both paths are identical, the overlapped beams will be in phase with each other and interfere constructively. In other case however, any relative phase accumulation $\Delta\phi$ will produce interference fringes which are diagnostic of the relative difference. By measuring the phase difference in these fringes, it is possible to resolve the magnitude of the cause with a high sensitivity. Since a visible laser beam has a wavelength of the order of 10^2 nm, it is clear that this method constitutes an ideal tool for precision measurements. By using atoms in a similar mechanism where massive particles follow spatially separated paths, it is possible to realise an *atom interferometer* [58] for measuring gravity.

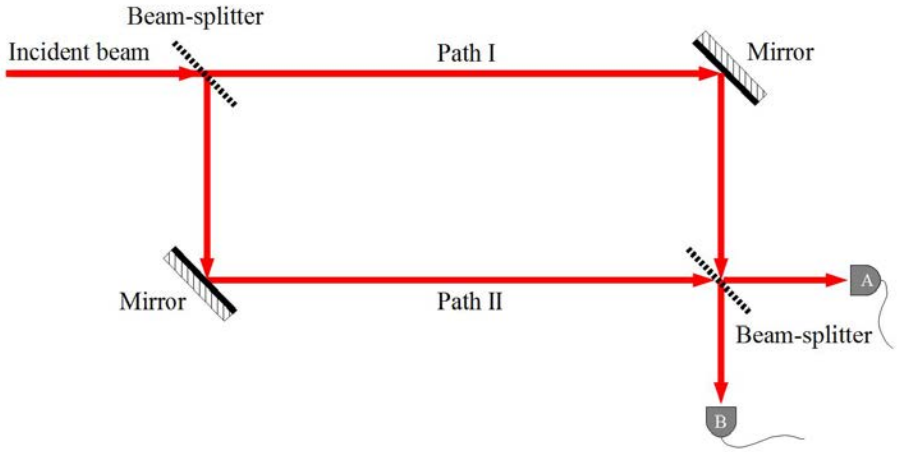

Figure 2.6: Mach–Zehnder interferometer scheme consisted of a combination of two beam splitters and mirrors. The incident light beam is equally split in two paths which are guided with the aid of the mirrors and finally recombine at the end. Any relative phase difference between the two paths will cause interference fringes at the output, which are used to deduce the magnitude of the cause.

Before moving further to the atom interferometry technique, it is constructive to make a brief introduction to the two-level atom model that considers interaction with a light field. The theoretical treatment in the next sections follows the work in [16, 47].

2.2.1 Two-Level Atom

The Hamiltonian describing an atom with a ground $|\mathrm{g}\rangle$ and excited state $|\mathrm{e}\rangle$ within a light field $\mathbf{E}_\mathrm{L}$ is

$$\mathcal{H} = \frac{\mathbf{p}^2}{2m} + \hbar\omega_\mathrm{g} |\mathrm{g}\rangle \langle\mathrm{g}| + \hbar\omega_\mathrm{e} |\mathrm{e}\rangle \langle\mathrm{e}| - \mathbf{d} \cdot \mathbf{E}_\mathrm{L}, \tag{2.7}$$

where m the atom mass, $\mathbf{p}$ its momentum and $\mathbf{d}$ the atomic dipole moment. $\mathbf{E}_\mathrm{L}$ is the external electric field given in the classical form as

$$\mathbf{E_L}(t) = \mathbf{E_0} \cos\left(\omega_\mathrm{L} t + \phi_\mathrm{L}\right), \tag{2.8}$$

where $\mathbf{E_0}$ is a constant amplitude and ω_L the light frequency with an arbitrary phase ϕ_L.

The wave function describing the atomic state at an arbitrary time t is

$$|\Psi(t)\rangle = a_\mathrm{e}(t) |\mathrm{e}\rangle + a_\mathrm{g}(t) |\mathrm{g}\rangle, \tag{2.9}$$

with $a_\mathrm{g}(t)$ and $a_\mathrm{e}(t)$ being the amplitude coefficients of the corresponding states at time t. Substitution of

(2.9) to the Schrödinger time dependent equation

$$i\hbar\frac{\mathrm{d}}{\mathrm{d}t}\left|\Psi(t)\right\rangle = \mathcal{H}\left|\Psi(t)\right\rangle, \tag{2.10}$$

yields

$$i\hbar\dot{a}_{\mathrm{e}}(t) = \hbar\omega_{\mathrm{e}}a_{\mathrm{e}}(t) + a_{\mathrm{g}}(t)\left\langle \mathrm{e}\right|\mathbf{d}\cdot\mathbf{E_L}\left|\mathrm{g}\right\rangle, \tag{2.11}$$

$$i\hbar\dot{a}_{\mathrm{g}}(t) = \hbar\omega_{\mathrm{g}}a_{\mathrm{g}}(t) - a_{\mathrm{e}}(t)\left\langle \mathrm{e}\right|\mathbf{d}\cdot\mathbf{E_L}\left|\mathrm{g}\right\rangle. \tag{2.12}$$

The transition coefficients from the ground to the excited state are given by

$$\left\langle \mathrm{e}\right|\mathbf{d}\cdot\mathbf{E_L}\left|\mathrm{g}\right\rangle = \hbar\Omega_{\mathrm{eg}}\left[\frac{e^{i(\omega_{\mathrm{L}}t+\phi_{\mathrm{L}})}+e^{-i(\omega_{\mathrm{L}}t+\phi_{\mathrm{L}})}}{2}\right], \tag{2.13}$$

where

$$\Omega_{\mathrm{eg}} = -\frac{\left\langle \mathrm{e}\right|\mathbf{d}\cdot\mathbf{E_0}\left|\mathrm{g}\right\rangle}{\hbar} \tag{2.14}$$

is the *Rabi frequency* on resonance. The above equations can be simplified by using the *rotating wave approximation* (RWA) [80] resulting to

$$i\dot{c}_{\mathrm{e}}(t) = \frac{\Omega_{\mathrm{eg}}}{2}e^{-i\delta t}e^{-i\phi_{\mathrm{L}}}c_{\mathrm{g}}(t) \tag{2.15}$$

$$i\dot{c}_{\mathrm{g}}(t) = \frac{\Omega^{*}_{\mathrm{eg}}}{2}e^{i\delta t}e^{i\phi_{\mathrm{L}}}c_{\mathrm{e}}(t), \tag{2.16}$$

where $\Omega_{\mathrm{eg}} \ll \omega_{\mathrm{e}}, \omega_{\mathrm{e}}$ was considered, so that the fast oscillating terms can be factored out from the slowly oscillating ones as

$$a_{\mathrm{g}}(t) = c_{\mathrm{g}}(t)\cdot e^{-i\omega_{\mathrm{g}}t} \tag{2.17}$$

$$a_{\mathrm{e}}(t) = c_{\mathrm{e}}(t)\cdot e^{-i\omega_{\mathrm{e}}t}. \tag{2.18}$$

Finally, assuming an exposure time τ the derived atomic state coefficients are

$$c_{\mathrm{g}}(t_0+\tau) = e^{i\delta\tau/2}\left\{c_{\mathrm{g}}(t_0)\left[\cos\left(\frac{\Omega\tau}{2}\right) - i\frac{\delta}{\Omega}\sin\left(\frac{\Omega\tau}{2}\right)\right] + c_{\mathrm{e}}(t_0)e^{i(\delta t_0+\phi_{\mathrm{L}})}\left[-i\frac{\Omega_{\mathrm{eg}}}{\Omega}\sin\left(\frac{\Omega\tau}{2}\right)\right]\right\} \tag{2.19}$$

$$c_{\mathrm{e}}(t_0+\tau) = e^{-i\delta\tau/2}\left\{c_{\mathrm{g}}(t_0)e^{-i(\delta t_0+\phi_{\mathrm{L}})}\left[-i\frac{\Omega_{\mathrm{eg}}}{\Omega}\sin\left(\frac{\Omega\tau}{2}\right)\right] + c_{\mathrm{e}}(t_0)\left[\cos\left(\frac{\Omega\tau}{2}\right) + i\frac{\delta}{\Omega}\sin\left(\frac{\Omega\tau}{2}\right)\right]\right\} \tag{2.20}$$

where Ω is the *generalised Rabi frequency*

$$\Omega = \sqrt{\delta^2 + \Omega_{\mathrm{eg}}^2}. \tag{2.21}$$

The atomic state probabilities are then given by

$$\mathcal{P}_{\mathrm{g}}(\tau) = \left(\frac{\Omega_{\mathrm{eg}}}{\Omega}\right)^2 \frac{[1 + \cos(\Omega\tau)]}{2} \tag{2.22}$$

$$\mathcal{P}_{\mathrm{e}}(\tau) = \left(\frac{\Omega_{\mathrm{eg}}}{\Omega}\right)^2 \frac{[1 - \cos(\Omega\tau)]}{2}, \tag{2.23}$$

demonstrating an oscillatory behaviour with frequency Ω. Assuming zero detuning $\delta = 0$, $\Omega = \Omega_{\mathrm{eg}}$ and equations (2.19), (2.20) are simplified to

$$c_{\mathrm{g}}(t_0 + \tau) = c_{\mathrm{g}}(t_0)\cos\left(\frac{\Omega_{\mathrm{eg}}\tau}{2}\right) - ic_{\mathrm{e}}(t_0)e^{i\phi_{\mathrm{L}}}\sin\left(\frac{\Omega_{\mathrm{eg}}\tau}{2}\right) \tag{2.24}$$

$$c_{\mathrm{e}}(t_0 + \tau) = -ic_{\mathrm{g}}(t_0)e^{-i\phi_{\mathrm{L}}}\sin\left(\frac{\Omega_{\mathrm{eg}}\tau}{2}\right) + c_{\mathrm{e}}(t_0)\cos\left(\frac{\Omega_{\mathrm{eg}}\tau}{2}\right). \tag{2.25}$$

The corresponding probabilities become

$$\mathcal{P}_{\mathrm{g}}(\tau) = \frac{1 + \cos(\Omega_{\mathrm{eg}}\tau)}{2} \tag{2.26}$$

$$\mathcal{P}_{\mathrm{e}}(\tau) = \frac{1 - \cos(\Omega_{\mathrm{eg}}\tau)}{2}. \tag{2.27}$$

Considering the above derivations, the wave-function describing an atom starting from the $|\mathrm{g}\rangle$ state with a light exposure time τ is given by

$$|\Psi(\tau)\rangle = \cos\left(\frac{\Omega_{\mathrm{eg}}\tau}{2}\right)|\mathrm{g}\rangle + e^{-i\pi/2}e^{i\phi_{\mathrm{L}}}\sin\left(\frac{\Omega_{\mathrm{eg}}\tau}{2}\right)|\mathrm{e}\rangle. \tag{2.28}$$

This oscillatory behaviour of the time dependent wave-function between the two states is known as *Rabi oscillations* and is shown in fig. 2.7. An exposure time of $\tau = \pi/\Omega_{\mathrm{eg}}$ is commonly referred to as a π-pulse and will transfer the atom to the $|\mathrm{e}\rangle$ state. Similarly, a pulse of $\tau = \pi/2\Omega_{\mathrm{eg}}$ is known as a $\pi/2$-pulse, setting the wave-function in a linear superposition of $|\mathrm{g}\rangle$ and $|\mathrm{e}\rangle$ with equal probability amplitudes. These pulses will play a fundamental role throughout the experimental process, as it will be shown later.

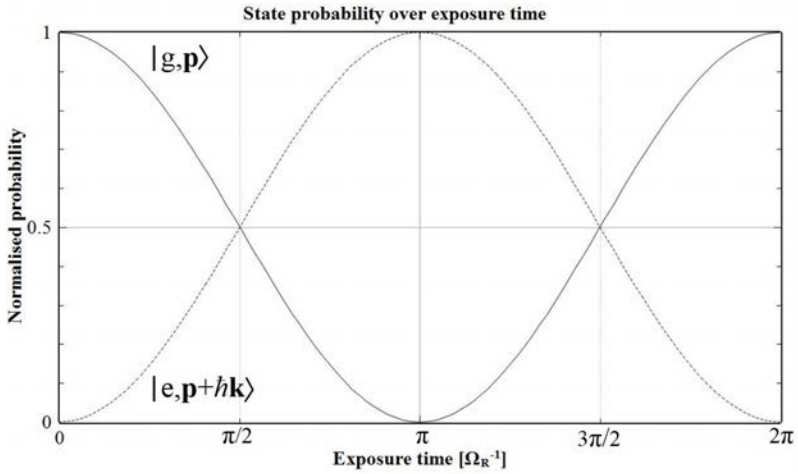

Figure 2.7: State probability graph versus exposure time, where zero detuning is considered. The exposure time which sets the wave function into a superposition of the two states is defined for the $\pi/2$-pulse, while the time for state inversion corresponds to the π-pulse.

2.2.2 Raman Transitions

This time, a three-level atom is considered with a virtual intermediate energy level as indicated in fig. 2.8 with the dashed lines. The light field now consists of two counter-propagating beams, equally detuned from

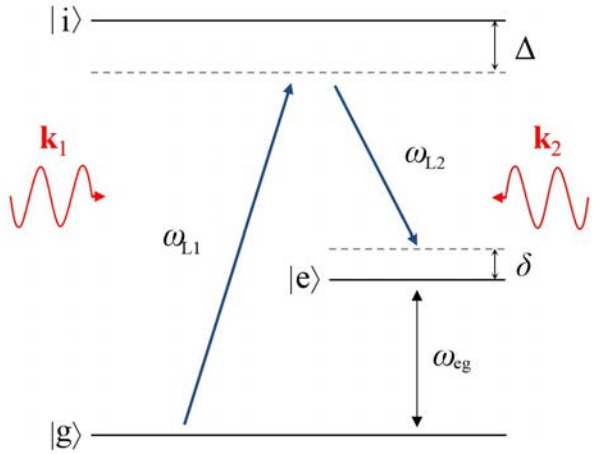

Figure 2.8: Basic Raman transitions scheme of a three-level atom model, consisting of a ground $|g\rangle$ and excited state $|e\rangle$, with an intermediate state $|i\rangle$ (diagram not in scale).

this level by Δ and is given by

$$\mathbf{E}_{\mathrm{L}} = \mathbf{E}_{\mathrm{L1}} \cos(\mathbf{k}_{\mathrm{L1}} \cdot \mathbf{r} - \omega_{\mathrm{L1}} t + \phi_{\mathrm{L1}}) + \mathbf{E}_{\mathrm{L2}} \cos(\mathbf{k}_{\mathrm{L2}} \cdot \mathbf{r} - \omega_{\mathrm{L2}} t + \phi_{\mathrm{L2}}). \tag{2.29}$$

From now on, it is convenient to apply the following definitions

$$\omega_{\text{eff}} = \omega_{\text{L1}} - \omega_{\text{L2}} \approx \omega_{\text{eg}} \tag{2.30}$$

$$\mathbf{k}_{\text{eff}} = \mathbf{k}_{\text{L1}} - \mathbf{k}_{\text{L2}} \approx 2\mathbf{k}_{\text{L1}}, \quad (\mathbf{k}_{\text{L1}} \approx -\mathbf{k}_{\text{L2}}) \tag{2.31}$$

$$\phi_{\text{eff}} = \phi_{\text{L1}} - \phi_{\text{L2}}. \tag{2.32}$$

As shown in fig. 2.8, if the detuning Δ is considerably bigger than both δ and the natural line-width of $|\text{i}\rangle$, the transition probability between either $|\text{g}\rangle$ or $|\text{e}\rangle$ to $|\text{i}\rangle$ becomes negligible. Considering this, spontaneous emission can be ignored from calculations, and the system can be approximated by a two–level system with resonance frequency $\omega_{\text{eg}} = \omega_{\text{eff}} - \delta$ and a momentum transfer $\hbar\mathbf{k}_{\text{eff}}$. This two–photon process involving an intermediate level where an atom is transferred between two energy levels via a virtual level, is known as *Raman transition* [47, 80].

The Hamiltonian describing the atomic state in this case can be written as

$$\mathcal{H} = \frac{\mathbf{p}^2}{2m} + \hbar\omega_{\text{g}} |\text{g}\rangle \langle\text{g}| + \hbar\omega_{\text{e}} |\text{e}\rangle \langle\text{e}| + \hbar\omega_{\text{i}} |\text{i}\rangle \langle\text{i}| - \mathbf{d} \cdot \mathbf{E}_{\text{L}}. \tag{2.33}$$

Similarly to the previous treatment, the time-evolution coefficients corresponding to the $|\text{g}, \mathbf{p}\rangle$ and $|\text{e}, \mathbf{p} + \hbar\mathbf{k}_{\text{eff}}\rangle$ states can be obtained by

$$\begin{aligned} c_{\text{g}}(t_0 + \tau) = e^{-i\left(\frac{\Omega_+^{\text{AC}} - \delta}{2}\right)\tau} \Bigg\{ & c_{\text{g}}(t_0) \left[\cos\left(\frac{\Omega_{\text{R}}\tau}{2}\right) - i\frac{\delta - \Omega_-^{\text{AC}}}{\Omega_{\text{R}}} \sin\left(\frac{\Omega_{\text{R}}\tau}{2}\right) \right] + \\ & c_{\text{e}}(t_0) e^{i(\delta t_0 + \phi_{\text{eff}})} \left[-i\frac{\Omega_{\text{eff}}}{\Omega_{\text{R}}} \sin\left(\frac{\Omega_{\text{R}}\tau}{2}\right) \right] \Bigg\} \end{aligned} \tag{2.34}$$

$$\begin{aligned} c_{\text{e}}(t_0 + \tau) = e^{-i\left(\frac{\Omega_+^{\text{AC}} + \delta}{2}\right)\tau} \Bigg\{ & c_{\text{g}}(t_0) e^{-i(\delta t_0 + \phi_{\text{eff}})} \left[-i\frac{\Omega_{\text{eff}}}{\Omega_{\text{R}}} \sin\left(\frac{\Omega_{\text{R}}\tau}{2}\right) \right] + \\ & c_{\text{e}}(t_0) \left[\cos\left(\frac{\Omega_{\text{R}}\tau}{2}\right) + i\frac{\delta - \Omega_-^{\text{AC}}}{\Omega_{\text{R}}} \sin\left(\frac{\Omega_{\text{R}}\tau}{2}\right) \right] \Bigg\} \end{aligned} \tag{2.35}$$

where $\Omega_+^{\text{AC}} = \Omega_{\text{e}}^{\text{AC}} + \Omega_{\text{g}}^{\text{AC}}$ and $\Omega_-^{\text{AC}} = \Omega_{\text{e}}^{\text{AC}} - \Omega_{\text{g}}^{\text{AC}}$, with the corresponding factors

$$\Omega_{\text{g}}^{\text{AC}} = \frac{|\Omega_{\text{g},1}|^2}{4\Delta} + \frac{|\Omega_{\text{g},2}|^2}{4(\Delta - \omega_{\text{eg}})} \quad \text{and} \quad \Omega_{\text{e}}^{\text{AC}} = \frac{|\Omega_{\text{e},1}|^2}{4(\Delta + \omega_{\text{eg}})} + \frac{|\Omega_{\text{e},2}|^2}{4\Delta}, \tag{2.36}$$

expressing the Stark light shifts. For this model, (2.14) is written as

$$\Omega_{\mathrm{g,n}} = -\frac{\langle \mathrm{i}|\, \mathbf{d}\cdot\mathbf{E}_{\mathrm{n}}\, |\mathrm{g}\rangle}{\hbar} \quad \text{and} \quad \Omega_{\mathrm{e,n}} = -\frac{\langle \mathrm{i}|\, \mathbf{d}\cdot\mathbf{E}_{\mathrm{n}}\, |\mathrm{e}\rangle}{\hbar}, \quad (\mathrm{n} = 1,\, 2) \tag{2.37}$$

while the one photon detuning and the effective Rabi frequency coupling states $|\mathrm{e}\rangle$ and $|\mathrm{g}\rangle$ are given by

$$\delta = (\omega_{\mathrm{L1}} - \omega_{\mathrm{L2}}) - \left(\omega_{\mathrm{eg}} + \frac{\mathbf{p}\cdot\mathbf{k}_{\mathrm{eff}}}{m} + \frac{\hbar\,|\mathbf{k}_{\mathrm{eff}}|^2}{2m}\right), \tag{2.38}$$

$$\Omega_{\mathrm{eff}} = \frac{\Omega_{\mathrm{e}}^{*}\Omega_{\mathrm{g}}}{2\Delta} e^{i(\phi_{\mathrm{L1}} - \phi_{\mathrm{L2}})}. \tag{2.39}$$

Lastly, Ω_{R} is the off-resonant Rabi frequency expressed as

$$\Omega_{\mathrm{R}} = \sqrt{\Omega_{\mathrm{eff}}^2 + (\delta_{12} - \Omega_{-}^{\mathrm{AC}})^2}. \tag{2.40}$$

A summary of the light parameters used in the two–level and multi–level atom models is given in tab. 2.1.

two-level atom, single-photon transition	ω_{L}	$\mathbf{k}_{\mathrm{L}}$	ϕ_{L}	Ω_{eg}	Ω
multi-level atom, Raman transition	ω_{eff}	$\mathbf{k}_{\mathrm{eff}}$	ϕ_{eff}	Ω_{eff}	Ω_{R}

Table 2.1: Light parameters used in the two–level and multi–level atom models.

Assuming $\delta,\ \Omega_{-}^{\mathrm{AC}} \ll \Omega_{\mathrm{eff}}$, equations (2.34) and (2.35) can be simplified as

$$c_{\mathrm{g}}(t_0+\tau) = e^{-i\left(\frac{\Omega_{+}^{\mathrm{AC}} - \delta}{2}\right)\tau}\left[c_{\mathrm{g}}(t_0)\cos\left(\frac{\Omega_{\mathrm{eff}}\tau}{2}\right) - ic_{\mathrm{e}}(t_0)e^{i(\delta t_0 + \phi_{\mathrm{eff}})}\sin\left(\frac{\Omega_{\mathrm{eff}}\tau}{2}\right)\right] \tag{2.41}$$

$$c_{\mathrm{e}}(t_0+\tau) = e^{-i\left(\frac{\Omega_{+}^{\mathrm{AC}} + \delta}{2}\right)\tau}\left[c_{\mathrm{e}}(t_0)\cos\left(\frac{\Omega_{\mathrm{eff}}\tau}{2}\right) - ic_{\mathrm{g}}(t_0)e^{-i(\delta t_0 + \phi_{\mathrm{eff}})}\sin\left(\frac{\Omega_{\mathrm{eff}}\tau}{2}\right)\right]. \tag{2.42}$$

2.2.3 Interferometric Sequence

An atom interferometer is realised by a succession of specially engineered Raman light pulses. It should be noted that the term "Raman light" here refers to the light stimulating Raman transitions on the atoms forming the cold atomic cloud and not to be confused with the Raman type laser light sources. When a Raman pulse is applied on an atomic ensemble, it affects both the internal energy and momentum states of the atoms. In the case of a $\pi/2$–pulse, the population is set in a superposition between the $|\mathrm{g}\rangle$ and $|\mathrm{e}\rangle$ states. At the same time, the atoms transferred in the $|\mathrm{e}\rangle$ state receive a momentum kick by stimulated photon emission. This results in a spatial separation between the two state populations, resembling to a

50:50 beam–splitter. In a similar manner, a π–pulse inverts the internal atomic states with two photon momenta exchange, acting as a state mirror.

The amount of the induced momentum transfer can vary depending on the choice of the relative orientation between the two Raman beam wave vectors, as shown in fig. 2.9. In the *co-propagating* configuration the momentum transfer is equal to $\hbar\,(\mathrm{k}_1 - \mathrm{k}_2)$, while the Doppler effect cancels out since both beams are equally shifted from the atom resonance. This way, all atoms can be addressed without the need for velocity matching. In the *counter-propagating* configuration the momentum transfer equals to $\hbar\,(\mathrm{k}_1 + \mathrm{k}_2)$, however the Doppler shift cancels out only within a narrow velocity region. Therefore, this configuration introduces a narrow velocity selection since atoms coming from a different velocity group will have a lower transition probability.

Over the course of this work, the co-propagating Raman light configuration was used to prove atom interference. This technique allows for a high signal intensity but yields a lower sensitivity [see (2.50)]. The counter-propagating configuration will be used to achieve a higher sensitivity at a later stage when the experiment will be optimised for gravity sensing.

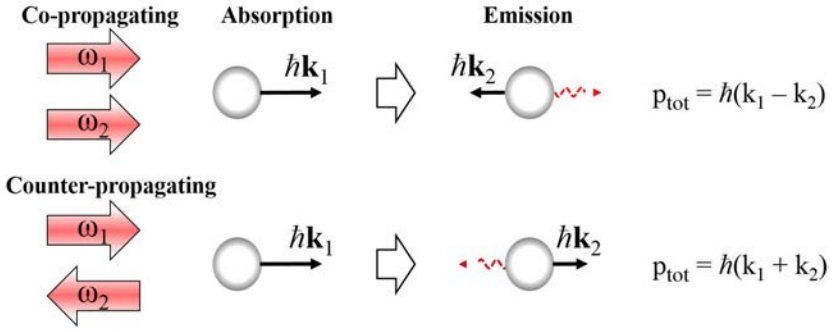

Figure 2.9: Two Raman beam configurations, resulting to a different momentum transfer. In the co-propagating case, the absorbed photon from the one beam is emitted in the same direction by stimulation from the second beam. In this case, the momentum transfer to the atom is $\hbar\,(\mathrm{k}_1 - \mathrm{k}_2)$. In the counter-propagating configuration the photon is emitted in the opposite direction, resulting in a two photon recoil kick equal to $\hbar\,(\mathrm{k}_1 + \mathrm{k}_2)$.

By using a $\pi/2 - \pi - \pi/2$ pulse sequence [58], it is possible to realise a Raman based Mach–Zehnder atom interferometer, as shown in fig. 2.10. The initial $\pi/2$–pulse will create the two interferometer arms where atoms at the $|\mathrm{g},\, \mathbf{p}\rangle$ state follow path I and those at the $|\mathrm{e},\, \mathbf{p} + \hbar\mathbf{k}_{\mathrm{eff}}\rangle$ state follow path II. After a time interval T, a π–pulse causes state inversion between the two wave–packets and finally, a symmetric $\pi/2$–pulse is applied at the overlap between the two ensembles, mixing the two states. Any local fields that interact with the atoms during this process, will imprint a relative phase difference on the individual wave–functions causing interference at the output (see fig. 2.10).

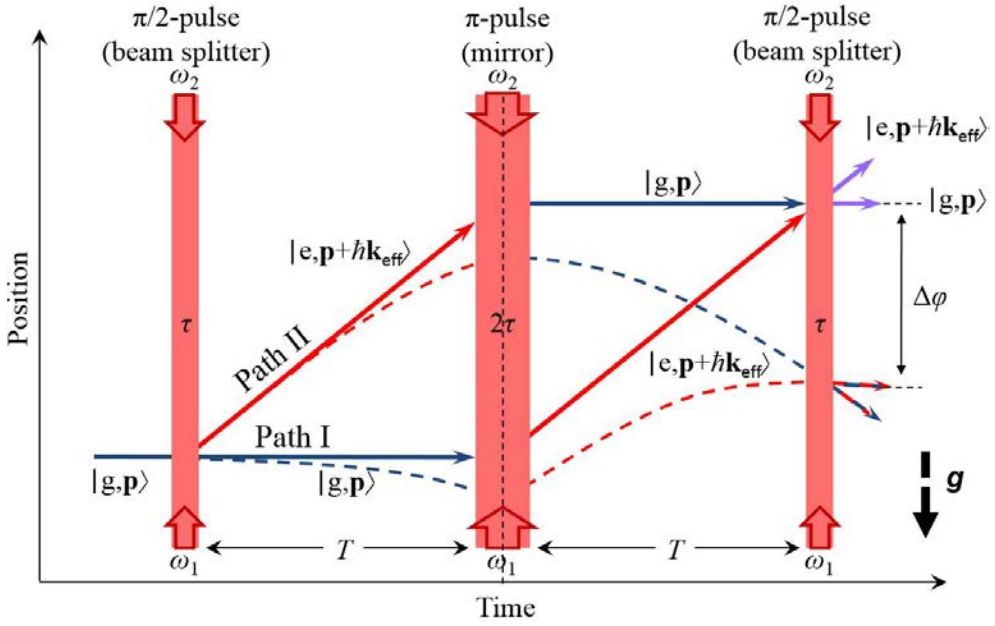

Figure 2.10: Mach–Zehnder scheme for an atom interferometer based on stimulated Raman transitions, comprising a $\pi/2 - \pi - \pi/2$ pulse sequence. The curved dashed lines take in to account the effect of the gravitational field, which points downwards.

The above $\pi/2 - \pi - \pi/2$ scheme proposed by Kasevich and Chu can be broken down to two successive sets of a $\pi/2 - \pi/2$ sequence, also known as *Ramsey sequence*. During this sequence, the atom receives an initial $\pi/2$-pulse of duration τ at time $t = 0$ and then a second $\pi/2$-pulse of the same duration after a time $t' = T$. Any interactions of the atom during the free evolution time T will introduce a phase factor, causing interference in the probability amplitude of detecting the atom at the excited state, given by [47]

$$\mathcal{P}_{\mathrm{e}}(\delta) = \left|\frac{\Omega_{\mathrm{eff}}\tau}{2}\right|^2 \left[\frac{\sin\left(\delta\tau/2\right)}{\delta\tau/2}\right]^2 \cos^2\left(\frac{\delta T}{2}\right). \tag{2.43}$$

By plotting this probability amplitude as a function of different detunings from the atomic resonance δ, one derives the characteristic interference pattern shown in fig. 2.11, which is known as *Ramsey fringes* [18, 19]. The envelope encapsulating the fringes is related to the pulse length τ, while the separation among them is related to the free evolution interval T.

2.3 Interferometer Phase Contributions

Similarly to a photon, a particle is considered to be in a superposition of both interferometer arms due to its wave nature. Therefore, all possible paths through the interferometer will contribute to the final phase. The

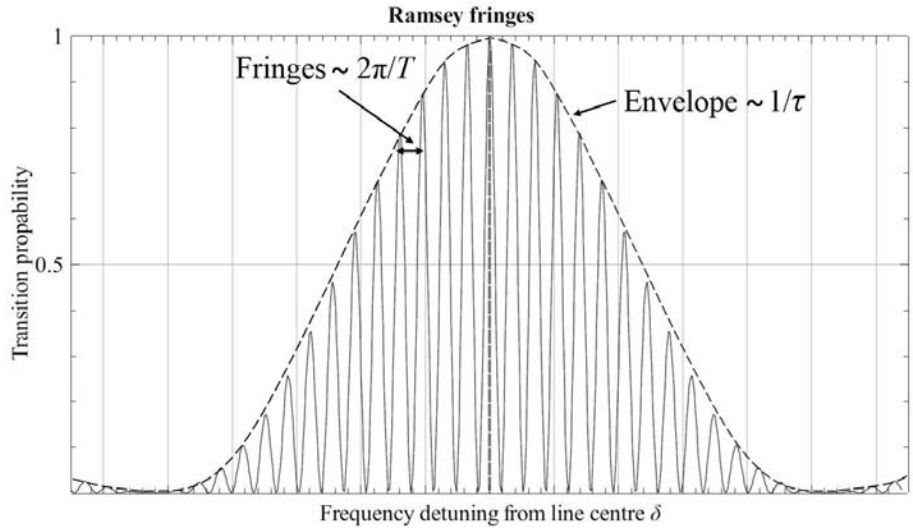

Figure 2.11: Theoretical example of Ramsey fringes produced by two successive $\pi/2$ pulses, separated by a free evolution time T.

tool used to derive the involved phase–shifts during this process is the *Feynman's path integral* concept [45] of a freely moving particle subject to a potential V. This formalism generalizes the action principle of classical mechanics where all possible trajectories from a point $r(t_1)$ to a point $r(t_2)$ are possible. However, they interfere with each other and the highest probability amplitude corresponds to the path approaching the classical trajectory. Considering a Lagrangian

$$\mathcal{L}[r(t), \dot{r}(t)] = \frac{1}{2} m \dot{r}^2 - V(r), \tag{2.44}$$

the related classical action between the two points is derived from

$$S = \int_{t_1}^{t_2} \mathcal{L}[r(t), \dot{r}(t)] dt. \tag{2.45}$$

Finally, the evolution phase–shift is given by

$$\Delta\phi_{\text{ev.}} = \frac{1}{\hbar}(S^{\text{II}} - S^{\text{I}}) = \frac{1}{\hbar} \oint_{\text{C}_0} \mathcal{L} dt, \tag{2.46}$$

where S^{I} and S^{II} are the actions corresponding to path I and II, while C_0 is the whole classical interferometer path. In practice, the total interferometer phase–shift can be decomposed into three main components as

$$\Delta\phi_{\text{tot}} = \Delta\phi_{\text{L}} + \Delta\phi_{\text{sep.}} + \Delta\phi_{\text{ev.}}, \tag{2.47}$$

which are described below.

Interaction with the light during each pulse at $t = 0, T$ and $2T$ leaves a phase imprint $\Delta\phi_{\rm L}$ on the atomic wave–function, approximated by

$$\Delta\phi_{\rm L} = \phi_{\rm L}^{\rm II} - \phi_{\rm L}^{\rm I} = \phi_{\rm eff}(0) - 2\phi_{\rm eff}(T) + \phi_{\rm eff}(2T),\ (T \gg \tau) \tag{2.48}$$

where $\phi_{\rm eff}$ is defined at the beginning of the pulse.

In addition, the presence of non–uniform fields will cause a non–perfect overlap between the two wave-packets during the last pulse. This physical separation Δz will raise a $\Delta\phi_{\rm sep.}$ phase–shift given by

$$\Delta\phi_{\rm sep.} = \frac{\mathrm{p}\Delta z}{2\hbar}. \tag{2.49}$$

Finally, $\Delta\phi_{\rm ev.}$ involves all atom interactions with the local forces during the wave–function free evolution, at the time interval T between the sequential Raman pulses. For a given potential V, this term can be derived by (2.46).

In a real experiment, a plethora of local sources contribute to the final interferometer phase which has been discussed thoroughly in the literature [37, 65, 66, 110]. Some of these sources can be either intrinsic such as mirror vibrations, sensor tilt, laser frequency and intensity noise, or related to external fields. Among them, the gravitational field has the highest impact and is the quantity of interest for a gravitational sensor, while stray magnetic fields can produce undesired signals of similar magnitude.

2.3.1 Gravitational Field

The local gravitational field cannot be shielded and will interact with any massive particle, causing inertial phase shift. Assuming the gravity acceleration g as constant and uniform in the measurement region, $\Delta\phi_{\rm sep.}$ and $\Delta\phi_{\rm ev.}$ will vanish. Considering $z = 0$ and $\dot{z}(0) = u_0$ to be the initial conditions and $V = -mgz$, the resulting phase-shift from (2.44) can be approximated by [93]

$$\Delta\phi_g = -\mathbf{k}_{\rm eff} g T^2, \tag{2.50}$$

As the velocity of a free falling particle changes by $\dot{z}(t) = u_0 - gt$, the Raman frequency needs to be ramped accordingly, in order to stay in resonance with the particle frame of reference. In practice, g is determined by applying the appropriate frequency ramp that compensates for the produced Doppler shift

by the free fall [59]. From (2.50) it is clear that sensitivity increases quadratically by time T or equivalently, by the available falling distance. For this reason, large scale experiments have been realised as described in [52, 115, 130]. Figure 2.12 shows an example of gravity signal caused by tidal effects, as measured form the group at the University of Stanford [92].

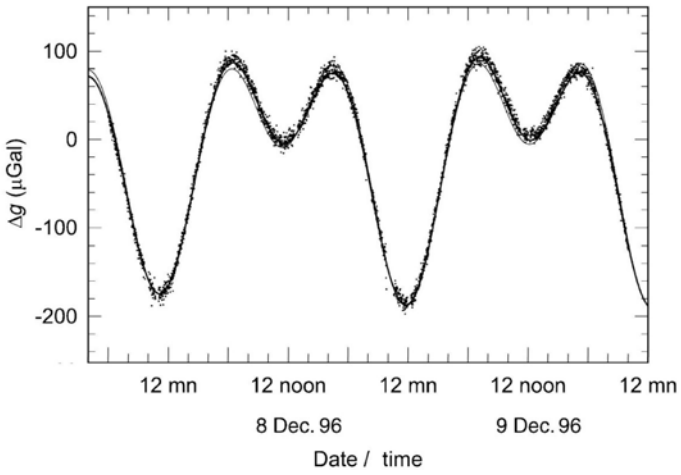

Figure 2.12: Gravity signal of the Earth's tides acquired after two days of gravity measurements at Stanford University (figure copied from [92]).

In the case of a gravimeter the measurement is performed on a single atom cloud. When realising a gravity gradiometer, two free falling atom clouds are used, physically separated from each other by Δh. Considering a reference level $z = 0$ with an acceleration value of $-g$ and a constant acceleration gradient γ, the equation of motion becomes $\ddot{z}(t) = -g + \gamma z(t) + z(0)$. The Raman pulses are performed on the two clouds simultaneously, so that the local g_1 and g_2 values are measured at points z_1 and z_2, respectively. This way any common frame accelerations or light fluctuations will cancel out, making this technique practically immune to relevant error sources. By adding a perturbation $\Delta\mathcal{L} = -\frac{1}{2}m\gamma z^2$ to (2.44), the gravity gradient shift is derived by [65, 73]

$$\Delta\phi_{\text{grad}} = \mathbf{k}_{\text{eff}}\gamma\Delta h T^2, \tag{2.51}$$

where $\gamma = g_2 - g_1$.

For this experiment, Δh and T are estimated to be approximately 10 cm and ∼100 ms, respectively, depending on the chosen scheme. Assuming $\gamma \approx 3 \times 10^{-6}$ s^{-2}, $\Delta\phi_{\text{grad}} \sim 10^{-7}g$. The above treatment can be generalised to any kind of frame accelerations so that the sensor can be used as a very sensitive accelerometer.

2.3.2 Magnetic Fields

External magnetic fields can affect the atoms in two ways. Either by distorting their trajectory through dipole moment interaction forces or by causing internal energy level shifts via the Zeeman effect, respectively. Since the Zeeman effect is discussed separately in §2.5.2, the relevant equations shown here will be considered as known. Assuming an atom with a magnetic dipole moment $\boldsymbol{\mu}$ subject to an external magnetic field $\mathbf{B}$, it will gain a potential energy equal to $-\boldsymbol{\mu}\cdot\mathbf{B}$. This induces a magnetic force acceleration on the atom given by [65]

$$\mathbf{a} = \frac{1}{m}\mathrm{m_F}\mu_\mathrm{B} g_\mathrm{F}\frac{\mathrm{dB}_z}{\mathrm{d}z}\frac{\boldsymbol{z}}{|\boldsymbol{z}|}. \tag{2.52}$$

This force depends on the atomic $\mathrm{m_F}$ quantum number and mass m, and vanishes under a uniform field. Preparing atoms in the $\mathrm{m_F}=0$ state and applying efficient magnetic shielding across the measurement region will suppress magnetically induced accelerations to the first order.

However, although atoms in the $\mathrm{m_F}=0$ are immune to the first order Zeeman–shift, they do interact with the field by the second order Zeeman effect, that causes a hyperfine splitting between the corresponding states in the $\mathrm{F}=1$ and $\mathrm{F}=2$ levels, given by $\Delta E_\mathrm{Z} = h\alpha_\mathrm{Z}^{(\mathrm{II})}\left|\mathbf{B}\right|^2/2$. This will produce an acceleration given by [65]

$$\mathbf{a} = \frac{h}{m}\alpha_\mathrm{Z}^{(\mathrm{II})}\mathrm{B}\frac{\mathrm{dB}_z}{\mathrm{d}z}\frac{\boldsymbol{z}}{|\boldsymbol{z}|}, \tag{2.53}$$

where $\alpha_\mathrm{Z}^{(\mathrm{II})}$ is the quadratic Zeeman coefficient. The related phase-shifts can be deduced similarly to the gravity and gravity gradient shifts (2.50) and (2.51), by substituting $\mathbf{a}$ to $\boldsymbol{g}$ and $\frac{\mathrm{dB}_z}{\mathrm{d}z}$ to γ.

As a comparison example, assuming $\mathrm{B}=50\,\mu\mathrm{T}$ and $\frac{\mathrm{dB}_z}{\mathrm{d}z}=5\cdot10^{-3}\ \mu\mathrm{T/mm}$, the induced acceleration on a ^{87}Rb atom in the $\mathrm{m_F}=1$ state will be $\mathrm{a}_{(\mathrm{m_F}=1)}\sim 3.3\cdot10^{-5}g$, according to (2.52). For the $\mathrm{m_F}=0$ case, (2.53) yields $\mathrm{a}_{(\mathrm{m_F}=0)}\sim 6.5\cdot10^{-9}g$, ($\alpha_\mathrm{Z}^{(\mathrm{II})}=575\cdot10^{-4}\ \mathrm{Hz}/\mu\mathrm{T}^2$). This example shows that even for atoms prepared in the $\mathrm{m_F}=0$ state, the above effect can induce accelerations comparable to the gravitational signal level of human size objects. Therefore, special care should be taken for reducing the local magnetic field magnitude and gradient within the experimental region. A case study on the impact of these magnetically induced accelerations on an atom interferometer is discussed in §2.5.3.

In the above discussion, the magnetic field was assumed to be constant over time. In the case of a time varying magnetic field $\mathbf{B}(t)$ the induced Zeeman shift will cause time dependent variations in the atomic resonance, given by (2.62). For simplicity, the magnetic field can be assumed to be uniform across the

experimental region, so no inertial forces will act on the atoms. The induced phase shift is now given by [65]

$$\Delta\phi_{\mathrm{Z,II}} = 2\pi \int_0^{2T} \alpha_{\mathrm{Z}}^{(\mathrm{II})} |\mathbf{B}(t)|^2 \mathrm{d}t, \tag{2.54}$$

where atoms in the $\mathrm{m_F} = 0$ state have been considered. Assuming a rectangular 1 ms pulse of a uniform magnetic field of 10 µT ($\sim \frac{1}{5}\mathrm{B_{Earth}}$) that occurs only during the second interferometer interval, it can produce a phase shift of $\Delta\phi = 361$ mrad.

2.4 Working With Rubidium–87 Species

Throughout this work, the energy level definition is given in the spectroscopic notation $\mathrm{n}^{(2\mathrm{S}+1)}\mathrm{L_J}$, where n is the principal quantum number, S the total electron spin angular momentum (in the case of alkalis, S = 1/2), L is the electron angular momentum (usually numbers 0, 1, 2, 3... are related to the letter code s, p, d, f..., respectively), and J = L + S the total electron angular momentum. Finally, F = J + I is the total angular momentum with I being the nuclear angular momentum. For ^{87}Rb, S = 1/2 corresponding to the the single outer 5s electron[1] (L = 0), with J = 1/2, while all inner atomic shells are completely filled. Also, I = 3/2 which depending on the relative orientation between vectors **I** and **J** gives F = 1 and 2, respectively.

Finally, it should be noted that only certain transitions between energy levels are allowed, which have to obey the following selection rules simultaneously [47, 80]

$$\Delta\mathrm{J} = 0, \pm 1, \tag{2.55}$$

$$\Delta\mathrm{L} = 0, \pm 1, \tag{2.56}$$

$$\Delta\mathrm{S} = 0. \tag{2.57}$$

These rules stem from energy and momentum conservation symmetries and can be summarized in

$$\Delta\mathrm{F} = 0, \pm 1 \ \ (\text{except for } \mathrm{F} = 0 \rightarrow \mathrm{F}' = 0). \tag{2.58}$$

One of the main requirements in choosing the atomic species for an atom interferometer is its resemblance to a two-level system, with both levels having natural decay times much longer than a single experimental cycle. In addition, first order magnetic field immunity is essential for atom manipulation

[1] By convention, the electron and atom angular momentum are indicated in lower and upper case characters, respectively.

and systematics suppression. The two hyperfine ground states of the alkali metal rubidium–87 species $|g\rangle = \left|5^2S_{1/2}, F = 1, m_F = 0\right\rangle$ and $|e\rangle = \left|5^2S_{1/2}, F = 2, m_F = 0\right\rangle$ fulfill the above requirements (see fig.2.13). Its relatively simple energy level structure with a cooling transition cycle $5^2S_{1/2}$ $F = 2$ to $5^2S_{3/2}$ $F' = 3$ corresponding to wave–lengths close to 780 nm, makes it practically easy to control with commercial diodes. The cooling transition has a relatively short lifetime, which can only decay at the $F = 2$ state, according to (2.58). However, as mentioned in the above discussion on Doppler cooling, this light needs to be red-detuned making it possible for some atoms to be excited to the $F' = 2$ state. This state decays at the $5^2S_{1/2}$ $F = 1$ level and the atom drops off the cooling cycle. For this reason a weaker repump laser is responsible for promoting these atoms back to the $F' = 2$. Atoms are detected by the same light source used for cooling but with no detuning, since high intensity fluorescence is required. The above experimental transitions for ^{87}Rb are indicated in fig. 2.13.

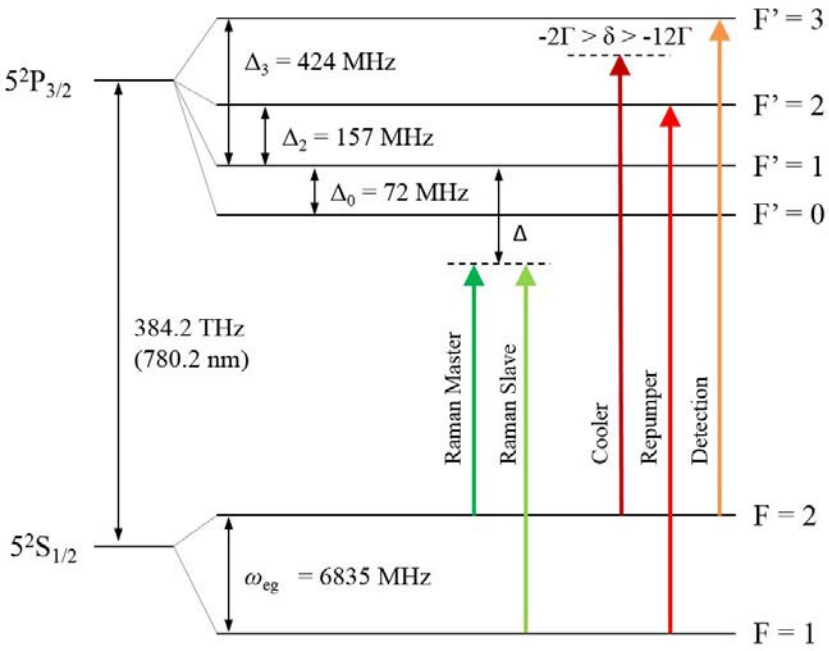

Figure 2.13: Energy level scheme for ^{87}Rb along with the experimental transitions. The cooling process is driven by the cooling laser, while the repumper laser brings atoms fallen in the $F = 1$ ground state back to the cooling cycle. The two Raman light frequencies drive the transition between the two ground states during the interferometric measurement. Finally, the detection light is used for population state readout (diagram not in scale).

2.5 Implications of a Portable Quantum Sensor

From the above discussion it is clear that an atom interferometer and quantum sensors in general, are

extremely sensitive devices susceptible to various sources of errors. Typical sources of noise that can affect gravity measurements like in fig. 2.12 can be classified into three main categories. The first category is the environmental noise which stems from phenomena such as celestial tides, ocean loading, atmospheric pressure and man-made noise. The second type of error sources depend on the measurement location, such as terrain effects, geographic latitude and elevation. Lastly, the third category is the instrumental noise which relates to effects like system tilt from the vertical, temperature on sensor, and others.

A great effort is put in order to control and compensate for these effects, if possible, and evaluate them for post processing. Although this is feasible for a lab based experiment where most conditions are well controlled, it becomes a great challenge to a portable quantum sensor which has to operate in a less controlled environment. Factors of the highest impact are temperature variations, external rotations, vibrations and stray magnetic fields.

2.5.1 Temperature and Mechanical Factors

A temperature variation of about 10 °C while operating in the field can affect optical components such as optical fibres and beam splitters, causing drifts by a few %. This will result in beam imbalances and noise that will affect the MOT and Raman sequence. In addition, the Coriolis effect is commonly compensated by an adjustable mirror through a piezo [116] at the end of the interferometry section §3.2. However, real time correction and absolute levelling when a sensor operates in the field is much more challenging. Consequently, missalignments among the atom quantisation axis, Raman beam wave vector and $\boldsymbol{g}$ will cause undesired phase-shifts. Other external sources of accelerations such as the wind and ambient vibrations also need to be compensated.

2.5.2 External Magnetic Fields

In the previous sections it was shown that the Zeeman effect is related to the interaction of the atoms with magnetic fields and is involved in various phenomena taking place in a cold atom experiment, with a considerable impact. In many cases it is exploited for engineering certain techniques such as the MOT realisation and Raman transitions, but at the same time it can become a significant error source if local magnetic fields are not well controlled. A brief overview of the Zeeman effect is given below which follows the discussion in [47, 80], while more information can be found in [69, 123].

The potential energy produced by the interaction between a magnetic dipole $\boldsymbol{\mu}$ and an external field $\mathbf{B}$ is generally given by $U = -\boldsymbol{\mu} \cdot \mathbf{B}$. In the case of an atom, a valence electron orbiting around the nucleus

is characterized by an orbital magnetic moment $\boldsymbol{\mu}_{\mathrm{L}} = -\mu_{\mathrm{B}}\mathbf{L}$, where μ_{B} is the Bohr magnetron and $\mathbf{L}$ the electron orbital momentum. In a similar manner, atom spin also produces a magnetic moment $\boldsymbol{\mu}_{\mathrm{S}} = -g_{\mathrm{S}}\mu_{\mathrm{B}}\mathbf{S}$, where g_{S} is the corresponding Lande g–factor and $\mathbf{S}$ the spin vector. Therefore,

$$\boldsymbol{\mu}_{\mathrm{e}} = -\mu_{\mathrm{B}}\mathbf{L} - g_{\mathrm{S}}\mu_{\mathrm{B}}\mathbf{S} = -g_{\mathrm{J}}\mu_{\mathrm{B}}\mathbf{J}, \quad (\mathbf{J} = \mathbf{L} + \mathbf{S}) \tag{2.59}$$

with $\mathbf{J}$ being the total electronic angular momentum. Normally, $\mathbf{L}$ and $\mathbf{S}$ are coupled and constitute the *fine structure*. The atomic nucleus also has a spin $\mathbf{I}$, producing its own magnetic moment given by

$$\boldsymbol{\mu}_{\mathrm{I}} = g_{\mathrm{I}}\mu_{\mathrm{N}}\mathbf{I}, \tag{2.60}$$

where μ_{N} is the nuclear magnetron. Combination of the above gives the total atomic magnetic moment

$$\boldsymbol{\mu}_{\mathrm{atom}} = -g_{\mathrm{J}}\mu_{\mathrm{B}}\mathbf{J} + g_{\mathrm{I}}\mu_{\mathrm{N}}\mathbf{I} \tag{2.61}$$

and similarly to the previous, the IJ–coupling is called the *hyperfine structure*. However, since $\mu_{\mathrm{N}} \ll \mu_{\mathrm{B}}$, the nuclear term is often neglected at first approximation.

When an external magnetic field interacts with an atom, it causes energy level shifts, lifting sub–level degeneracies. This phenomenon is called the Zeeman effect and is accompanied by the characteristic splitting of the atomic spectral lines, that depends on the field intensity. This interaction is expressed as a perturbation term into the atomic Hamiltonian. If $\mathbf{B}$ is weak enough so that the hyperfine interaction dominates, then $\mathbf{L}$ and $\mathbf{S}$ are coupled with $\mathbf{J}$, precessing around the external field $\mathbf{B}$ (see fig. 2.14). If the $\mathbf{I}$ contribution is considered, then the total angular momentum is given by $\mathbf{F} = \mathbf{J} + \mathbf{I}$, with a similar behavior. The Zeeman energy for this case is given by

$$E_{\mathrm{Z}} = g_{\mathrm{F}}\mu_{\mathrm{B}}\mathrm{m_F B} + h\alpha_{\mathrm{Z}}^{(\mathrm{II})}\mathrm{B}^2, \tag{2.62}$$

where the first term corresponds to the *first order* or *linear Zeeman effect* and the quadratic term to the *second order Zeeman effect*, where $h\alpha_{\mathrm{Z}}^{(\mathrm{II})} = \frac{g_{\mathrm{F}}^{(\mathrm{II})}}{m_e c^2}\mu_{\mathrm{B}}^2$. From the above expression it is clear that the $\mathrm{F} = 0$, $\mathrm{m_F} = 0$ state has no first order Zeeman shift, but is still susceptible to the second order effect.

2.5.3 Impact of Magnetic Field Gradient Forces on the Interferometer

For experiments operating inside the lab, the magnetic field produced by the Earth and nearby known operating electronic devices can be determined and compensated by active coil systems. A portable sensor

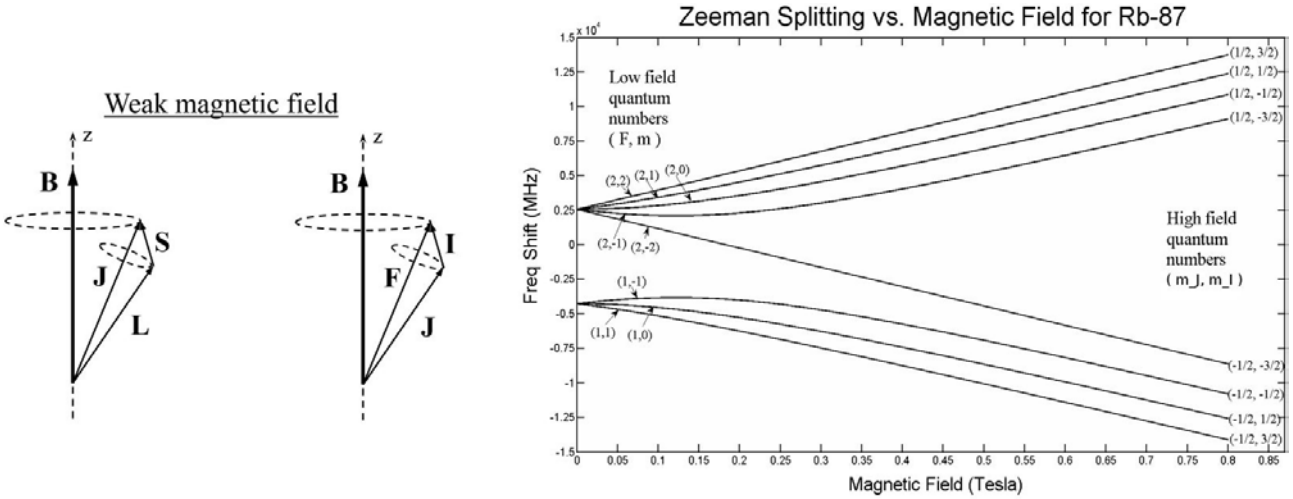

Figure 2.14: Representation of the corresponding atomic angular momentum vectors for week magnetic fields. The energy level diagram of the 5S line Zeeman splittings for ^{87}Rb is shown on the left (diagram copied from [112]).

on the other hand has to operate without the aid of such systems which would increase size and weight, making its use impractical. During field surveys the sensor will be transferred to sites of different background field conditions, while its location with respect to these fields will also vary. The presence of additional not well known sources can change the anticipated conditions even further. For instance, in civil engineering applications nearby buried cable lines or passing–by vehicles can introduce considerable magnetic noise, while underground rock formations with magnetic properties can potentially be an obscured magnetic field source when operating in open field.

As discussed previously, in order to perform the interferometric measurement, the quantization axis needs to be well defined for the atoms. For this reason, a uniform magnetic field is being applied along the z-axis of the interferometry tube by a solenoid, covering its length. Typically, values of the order of $\sim 10\,\mu$T are being used, which are of the same order of magnitude as the Earth's field $\sim 50\,\mu$T. However, the background field is neither uniform in space or constant in time and includes a horizontal component as well. For instance, typical values of the background field components from measurements taken in the lab at Birmingham are $B_{ver.} \approx 47\,\mu$T and $B_{hor.} \approx 17\,\mu$T, respectively. In addition, other sources like in the previous examples will also affect the local field, compromising the measurement even further.

By introducing a magnetic shield at the experimental region, the external fields will be attenuated. This will minimise the negative effects from the environment and will enable the creation of the desired field conditions for the atoms. A shield providing a field attenuation by a factor of $\sim 10^3$ will allow residual fields of the order of $\sim 10^{-2}\mu$T. This way, an applied quantisation field of $\sim 30\,\mu$T by the solenoid can be

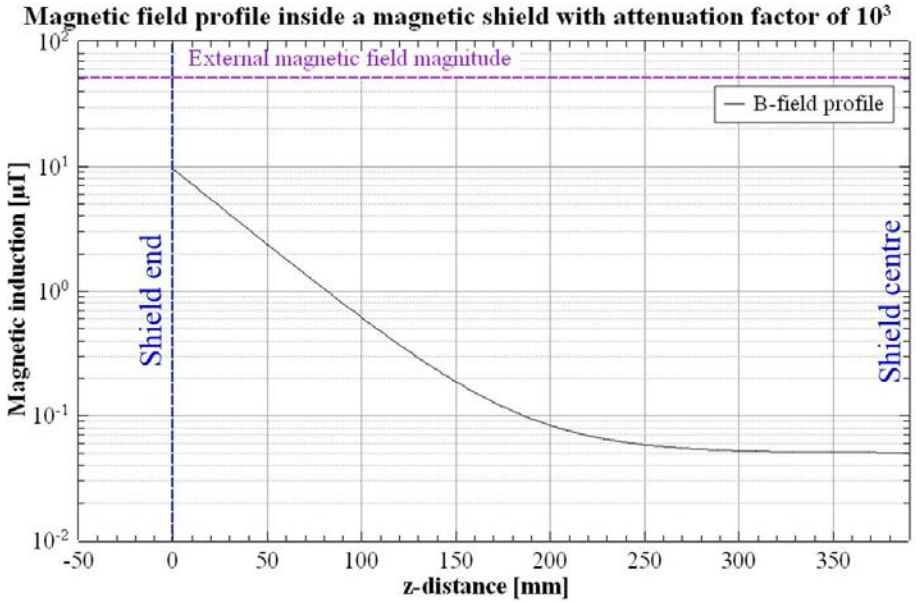

(a) Magnetic induction magnitude profile along the shield's longitudinal semi-axis.

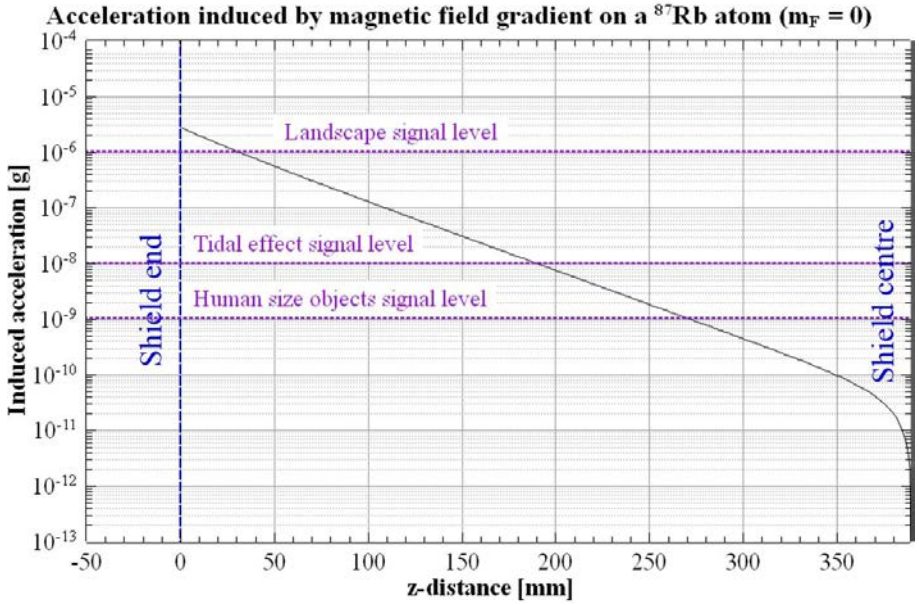

(b) Induced acceleration due to magnetic field gradient along the shield's longitudinal semi-axis.

Figure 2.15: (a) Magnetic induction magnitude profile along the longitudinal semi-axis of a magnetic shield providing a field attenuation by a factor of 10^3. An axial external magnetic field of 50 μT is considered, while field fringing at the shield's end is ignored. In this example, a triple-layered shield of 1 mm gauge mu-metal is considered with ID = 170 mm, IL = 800 mm and an air-gap of 10 mm between the layers. (b) Induced acceleration on a ^{87}Rb atom prepared in the $m_F = 0$ state due to magnetic field gradient, while moving along the shield's semi-axis. In this case, an applied quantisation field of 30 μT is considerer along the shield's axis, while the expected gravity signal levels of different sources are indicated by the horizontal dashed lines for comparison.

considered as constant within the experimental region. However, the magnetic field profile inside a shield is not constant but it drops exponentially from its ends towards the centre. Sub-figure 2.15a shows the magnetic induction magnitude profile along the longitudinal semi-axis of a hypothetical cylindrical magnetic shield. These values were derived from the expressions (4.13) and (4.17) which are discussed in §4, ignoring any field fringing effects at the shield's ends. In this example, a shield with dimensions comparable to the GGtop system is considered, consisting of three nested cylindrical shells with a thickness of $t = 1$ mm, separated by a 10 mm air-gap. The inner layer has an inner diameter of $ID = 170\,\text{mm}$ and inner length $IL = 800\,\text{mm}$, while a typical relative permeability value for mu-metal was used of $\mu_\text{r} = 20000$. The data point at z = 0 in the diagram corresponds to the shield's end, while an external field of 50 µT parallel to its axis is considered. The field decay at the shield's ends introduces a gradient which can induce a magnetic force on the atoms prepared in the $\text{m}_\text{F} = 0$ state due to the second order Zeeman effect, given by (2.53). Differentiation of the above field profile along the z-axis gives the field gradient that an atom experiences at each point, while moving along the shield's axis. By making use of these values and assuming an applied quantisation field of 30 µT, one can derive a plot of the induced acceleration along this axis, as shown in fig. 2.15b.

In the case of GGtop, the aim is to measure gravity signals of human size targets, typically of the order of $\sim 10^{-9} g_0$ (see tab. 1.2). Comparison of this value with the above example indicates that the measurement has to take place close to the central region of the shield, where the field gradient takes lower values. However, in the case of a small size atom interferometer like the GGtop, this can set limitations to the sensitivity of the gravitational measurement, which scales quadratically by the free evolution time T between the interferometric pulses.

The above figures provide an order of magnitude approximation of the potential impact of the local magnetic fields on the atomic inertia during a gravitational measurement. Considering these implications, it is indicative that these fields must be well controlled in order to be kept uniform and at a minimal magnitude within the experimental region. Chapters 4 and 5 are dedicated to the magnetic shielding aspects of such experiments, which is the focus of this work. Before that, a brief description of the GGtop interferometer apparatus will be presented in the following chapter.

CHAPTER 3

EXPERIMENTAL SETUP

Lab based atom interferometers have been demonstrated successfully over the past years, which are confined in a well controlled laboratory environment, while their dimensions can be as large as a couple of building floors to allow for high sensitivity [115].

The aim of the GGtop project is to build a mobile prototype version of these systems as a proof of principle of a versatile deployable sensor which could be used in the field to detect buried structures such as infrastructure pipelines, cables and archaeological artefacts. This application imposes numerous restrictions on the sensor design in terms of dimensions, weight and power consumption. In addition, stability issues during measurements in an environment outside the lab will create additional challenges. Vibrations, temperature fluctuations and external magnetic fields are some of the highest impact error sources.

This chapter provides a brief description of the GGtop experimental setup and its current status along with some key results.

3.1 Physics Package

Aim for the whole experimental apparatus architecture was to be transportable for field measurements. In this perspective, the system components were organised in two modules that can be carried outside the lab. The first module is the physics package which is shown in fig. 3.1, while the second module is the electronics package which is shown later.

A frame composed of aluminium profiles supports the vacuum chamber system including the three main lasers and the laser amplifier. The same structure hosts the laser distribution system box which carries the optic fibre network, the laser locking electronics box and the spectroscopy box. The total dimensions of the frame structure are $1628 \times 955 \times 500$ mm^3, while aluminium was chosen in the effort to reduce the overall

weight and avoid magnetic materials. Finally, the ensemble includes other smaller mechanical components like various mounts, the majority of which are 3D-printed out of plastic. The total weight of the system including the electronics is $\sim 200\,\mathrm{kg}$, with an energy consumption of $\sim 1\,\mathrm{kW}$. However, it should be noted that the primary objective of the experiment at this early stage was to achieve gravitational measurements. Therefore, system optimisation in terms of compactness and energy consumption would be the focus of the next stage. An initial work towards this goal is presented in [54], which relates to the development of a single-laser system. A similar portable system that is used as a test platform for novel components is the iSense experiment [74]. The future plan is to place the sensor system on a vibration isolating platform to reduce vibrational noise and tilts during measurements.

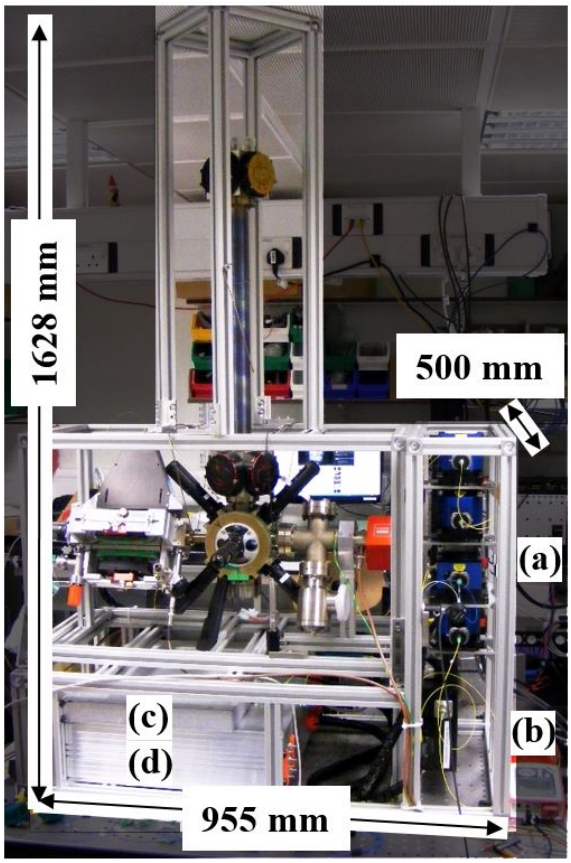

Figure 3.1: The whole physics package is supported by an aluminium frame structure which apart from the main ultra high vacuum system hosts (a) the master, cooling and repumper lasers, along with the amplifier (TA), (b) the spectroscopy box, (c) the beat locking electronics box and (d) the laser distribution system, based on a fibre optics network. The total weight of the system including the electronics is $\sim 200\,\mathrm{kg}$, with an energy consumption of $\sim 1\,\mathrm{kW}$.

3.2 Vacuum Chamber System

The main body of the device is the ultra-high vacuum chamber system (see fig. 3.2). In order to achieve a high number of atoms in a limited loading time, while maintaining ultra-high vacuum in the interrogation region, a system combining a 2D- and 3D-MOT was used. The chamber system can be divided into three sections. The 2D-MOT chamber where the atoms are captured and pre-cooled, the 3D-MOT chamber where further cooling and launching takes place, and finally the interferometry tube where the gravitational measurement is being performed. Apart from the requirement of a lightweight structure, its materials should primarily be non-magnetic, since any stray fields will affect the atoms considerably and therefore the output signal of the interferometer. For this reason, titanium was chosen for the vacuum chamber system which in addition to its robust structure, it demonstrates a high resistivity that provides fast dissipation to induced Eddy currents that can also affect the experiment. Furthermore, the incorporation of a differential pumping stage assures that the appropriate vacuum conditions in the MOT sections are being maintained.

2D-MOT Chamber

In the case of a deployable sensor like the GGtop, it is important to be able to achieve a high measurement repetition rate, in order to reach the desired accuracy within the limited time scales of a survey. In order to realise the gradiometer, one needs to launch two successive clouds vertically and measure gravity on both of them during flight, simultaneously. The time between two cloud launches is limited to $\lesssim 500\,\text{ms}$ by the system's height. This led to the implementation of a 2D-MOT to the system, which serves as a "bright" source of pre-cooled atoms. The chamber is of rectangular shape with dimensions of $250 \times 54 \times 54$ mm^3, incorporating four 30×120 mm^2 rectangular windows which allow optical access to the cooling light, while a circular window of 30 mm diameter situated at the one end allows access for a pushing beam (see fig. 3.3). All windows are 6 mm thick BK7 glass indium sealed by compression flanges. A 16 mm diameter tube inlet close to the pushing beam window allows access to the ^{87}Rb source dispenser which is regulated by a vacuum valve. Connection between the 2D-MOT and 3D-MOT sections is achieved by a 13 mm diameter tube placed at the centre of the opposite end-face of the chamber, incorporating carbon inlets that collimate the atom flux.

When a current is applied to the ^{87}Rb source dispenser, atoms are being released in the form of atomic vapour inside the 2D-MOT chamber and can be captured along its central region. The cooling light is being transferred via an optic fibre network to each of the two telescopes and is directed through the centre of the chamber in the form of an elliptical laser beam. This practice provides a larger volume coverage by the cooling

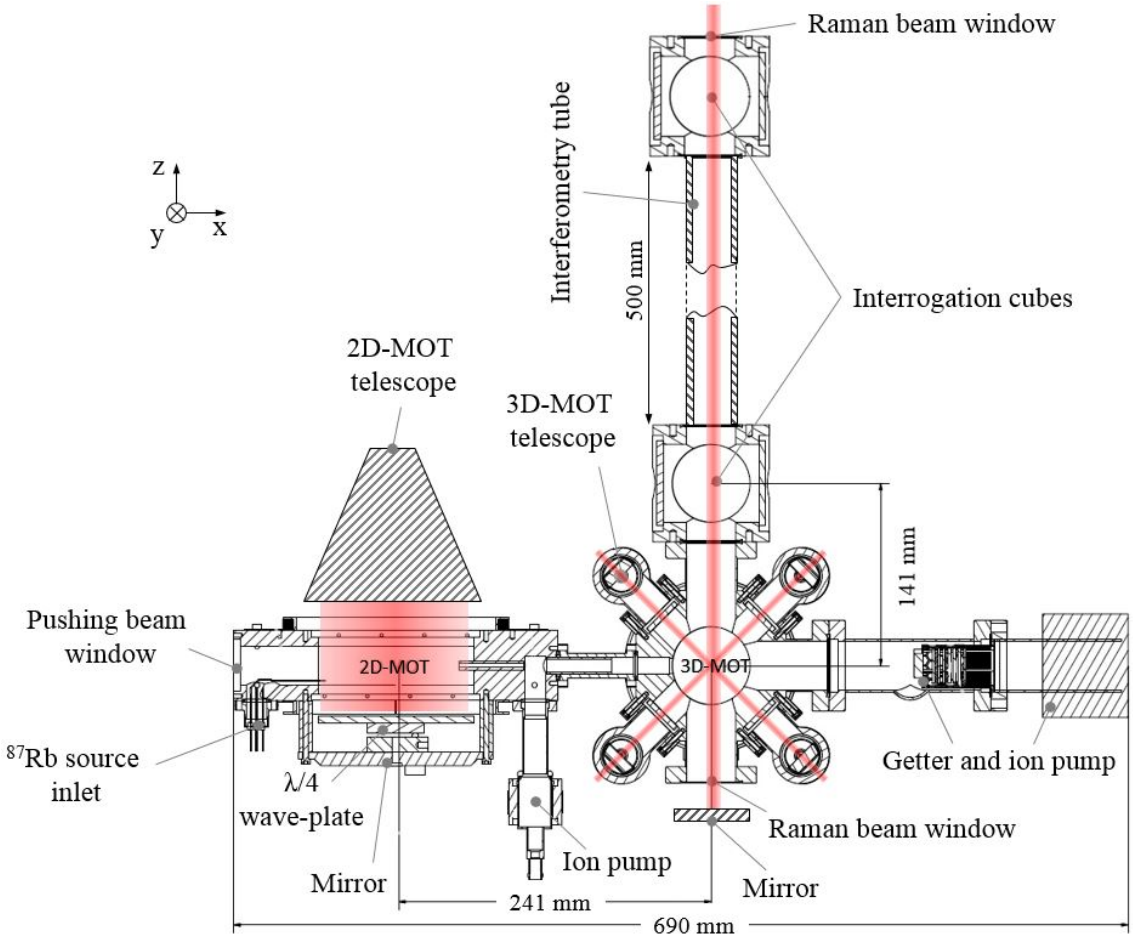

Figure 3.2: Schematic of the ultra-high vacuum chamber system. It consists of the 2D-MOT chamber, the 3D-MOT chamber and the interferometry section. A differential pumping stage enables the formation of a lower pressure in the 3D-MOT section compared to the 2D-MOT section.

light, resulting in an increased cooling area. Each beam is retro-reflected by an external mirror at the opposite window so that two perpendicular retro-reflected beams are being formed, coinciding along the chamber's axis. The use of a retro-reflected beam instead of two separate light beams provides higher stability against common frame vibrations and reduced number of optical components. In order to generate the appropriate magnetic field gradient for the MOT, four rectangular coils are placed around the four chamber windows in Ioffe configuration (see fig. 3.3). Each coil has dimensions of $\sim 17 \times 2.5$ cm^2 and a square cross-section, formed by 8×8 copper wires of 1 mm in diameter.

Atoms which are captured and cooled along the 2D-MOT axis region are confined with respect to the radial dimension of the chamber but can move along its longitudinal axis, in the form of a slow beam of cold atoms. This way, the atoms can be transferred to the 3D-MOT section. A common way to achieve this is by

the use of a pushing beaming which exerts light pressure on the trapped atoms along the longitudinal axis. Another way is to use a more complicated configuration consisting of smaller traps in series [97]. However, this requires a larger number of optical elements and will increase atom loses, affecting sensor performance. A smart and compact configuration arrangement was demonstrated in [63], where a small tilt of the 2D-MOT telescopes with respect to the chamber's longitudinal axis can produce a net force, or imbalance on the trapped atoms, causing the same effect as with a pushing beam. The latter option was chosen for this experiment, since this requires less space and fewer optical components. However, the option of incorporating a pushing beam as an alternative was also anticipated during the design.

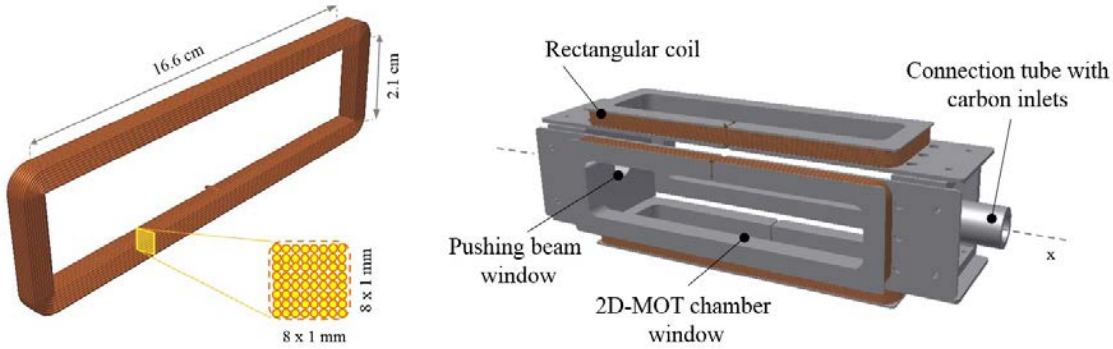

Figure 3.3: CAD render of the 2D-MOT chamber with the rectangular coils.

3D-MOT Chamber

Once the atoms have been pre-cooled in the 2D-MOT section are transferred to the 3D-MOT chamber. At this stage further cooling and state preparation will follow before launching the atomic cloud to the interferometry chamber. Considering this, the background pressure needs to be very low in order to reduce atom collisions. The required pressure values for this section are typically of the order of 10^{-9} mbar or lower. The geometry of this section is of circular shape, 60 mm in diameter and 38 mm in width, incorporating three inlets (see fig. 3.4a). One for the installation of the getter-pump (NEXTORR D100-5), one to allow connection to the 2D-MOT chamber and a third inlet that connects to the interferometry tube. The laser light can access the centre of the chamber through four circular windows of 30 mm in diameter at the sides of the circumference of the structure and two wider windows of 72 mm diameter on the circular faces. This configuration enables access to three counter-propagating pairs of light beams that intersect at the chamber's centre at right angles, forming an optical molasses. The chamber also incorporates a 37 mm diameter circular window at the bottom, which allows for the retro-reflection of the Raman beam coming from the top of the

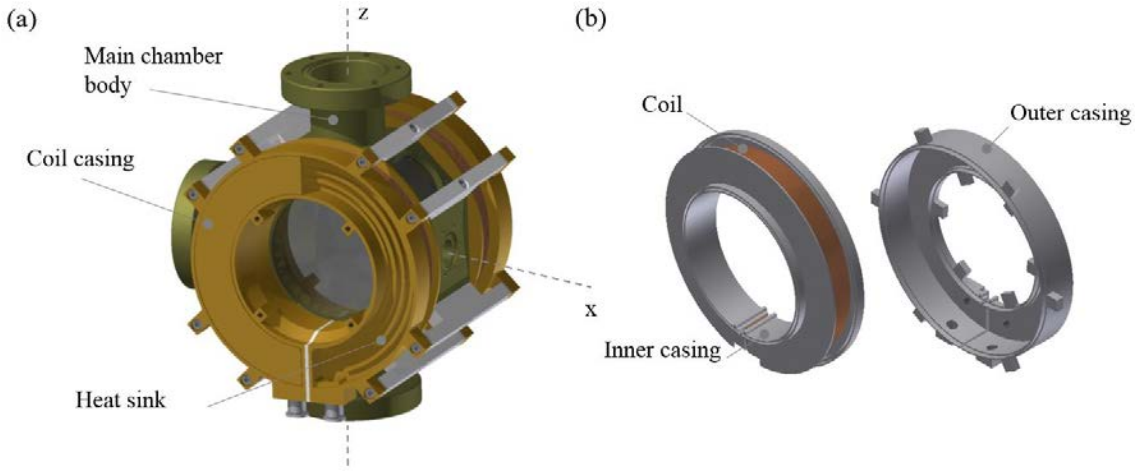

Figure 3.4: (a) Render of the 3D-MOT chamber assembly. (b) Circular anti-Helmholtz coil casing.

interferometry tube, as explained in the next subsection. The trapping magnetic field is produced by a pair of two circular anti-Helmholtz coils, mounted around the main chamber windows, creating a central field gradient of $\sim 1.3\,\mathrm{mT/cm}$ for a current of 1 A. Each of the coils has an inner diameter of 90 mm and consists of 352 turns of 1 mm copper wire with a total cross-section of $22 \times 37\ \mathrm{mm}^2$ (see fig. 3.4). In addition to the MOT coils, a system of three pairs of rectangular coils is mounted on the support frame of the device surrounding the 3D-MOT section in order to compensate for the external magnetic fields in three axes.

Atoms trapped within a MOT can reach temperatures close to the Doppler limit ($\approx$145 µK for rubidium). The cloud temperature at this stage is not sufficient for realising the experiment, since this will cause rapid cloud expansion once the atoms are released from the trap and will be lost before the measurement takes place. In order to reach lower temperatures, the sub-Doppler cooling technique [56] is used. During this process, the MOT coils are switched off leaving the atoms to interact only with the optical molasses. Then, a negative ramp in the laser light intensity with a simultaneous increase in frequency detuning, causes adiabatic cooling to the atoms within the molasses region. A schematic representation of this sequence is shown in fig. 3.5. A gradiometer is realised by launching two successive atom clouds fast enough (juggling), that will enable an interferometric measurement on both, simultaneously. In the case of GGtop, this translates to a molasses stage of a total time-length of approximately 10 ms [54]. However, the system is currently at an early stage and further optimisation is required to reach this performance.

The results from the above technique were evaluated by *time-of-flight* (TOF) [35] measurements which are shown in fig. 3.6. In this method, the MOT is switched off allowing the atom cloud to expand ballistically, in the presence of gravity. The expansion rate is related to the cloud temperature, which can be determined by

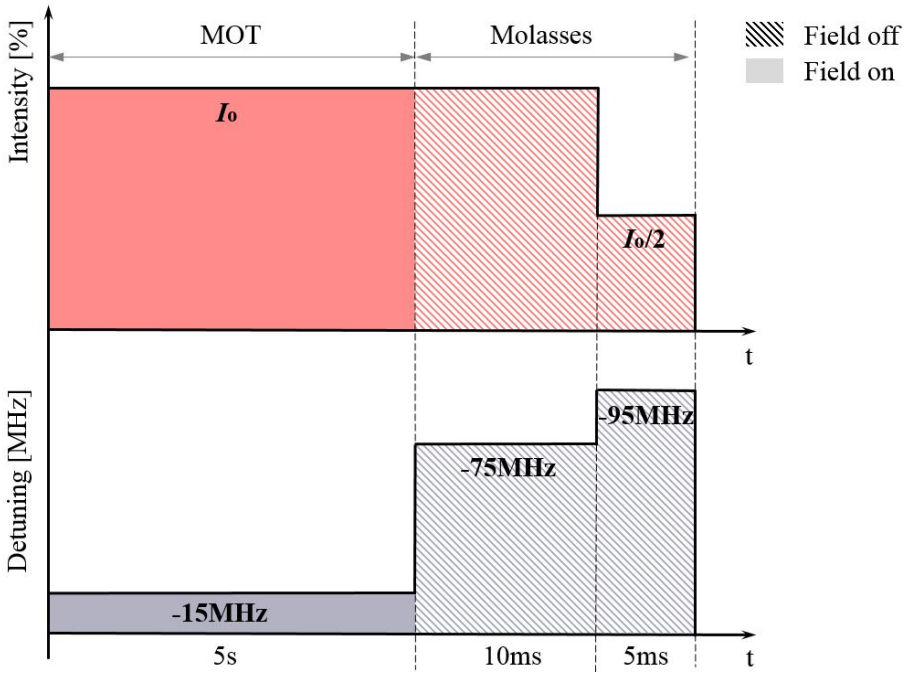

Figure 3.5: Schematic representation of the experimental molasses phase time sequence. The MOT coils are switched off and a stepped frequency detuning is introduced, along with a decrease in light intensity, causing adiabatic cooling (time axis not in scale).

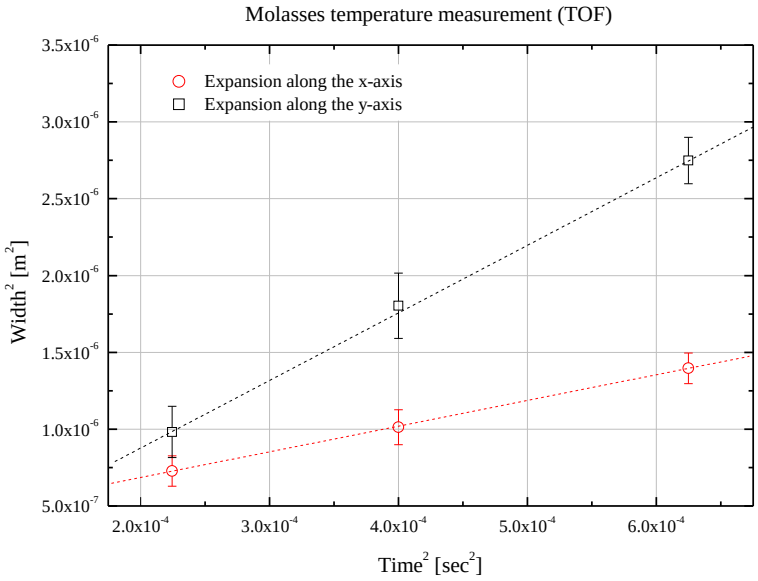

Figure 3.6: Time-of-flight measurements evaluating the sub-Doppler cooling efficiency [54, 86]. Each data point is extracted from 20 images of the expanding cloud, captured at the same time lapse.

measuring the cloud width over time. The two plot lines represent the measurements taken along the x and y axes, which demonstrate a deviation by a factor of ~ 2. This was mainly caused by intensity instabilities and stray magnetic fields in the MOT. Such effects can affect the uniformity and position of the cloud, and are discussed in §3.6. The extracted temperature value in this case was determined to be $\sim 45\,\mu K$. This value is lower than the Doppler limit by an order of magnitude; however, a cloud temperature of the order of a few μK is required for the experiment. The results are expected to improve by introducing a smoother intensity ramping during the sub-Doppler cooling phase, which could potentially reduce the light imbalance effects.

At the current stage, preliminary cloud launching trials have been initiated, aiming to realise an atomic fountain for gravity measurements. The mechanism to achieve this is known as the *moving molasses technique* [47]. An initial momentum is given to the cold atomic cloud upwards, by detuning the upper and lower MOT laser beams relative to each other. This mechanism produces a moving molasses, where the further detuned cooling beams behave as ordinary cooling beams in the atomic reference frame. By switching the magnetic field off and simultaneously ramping both cooling beam frequency and intensity, the atoms are given an initial vertical velocity and perform a parabolic flight under the local gravitational field. However, once the MOT is switched off, the atom cloud will start expanding due to its temperature. For this reason, its initial temperature needs to be sufficiently low, otherwise a large percentage of the atomic population will hit the chamber walls and will be lost, well before the interferometric sequence has been applied. Results for different relative beam detunings are shown in fig. 3.7, where the speed of the cloud's centre of mass (CM) is derived by a linear fit on the values extracted from fluorescence images, captured by a single camera [86]. It was observed that the atomic cloud takes an elongated shape before it vanishes (see fig. 3.8), indicating that a considerable number of atoms were accelerated towards this direction.

It should be noted that the above results correspond to the vertical velocity component as measured by a single camera. Horizontal cloud movement seemed insignificant and had not been measured up to this point. However, the addition of a second camera at a different aspect could reveal lateral accelerations, concealed in the first place. MOT stability and good control of the local magnetic fields play a crucial role on this sequence. In addition, launch control is also affected by local magnetic fields, which exert undesired accelerations onto the atoms. For this reason, a 3-axis compensation coil system was implemented at this region.

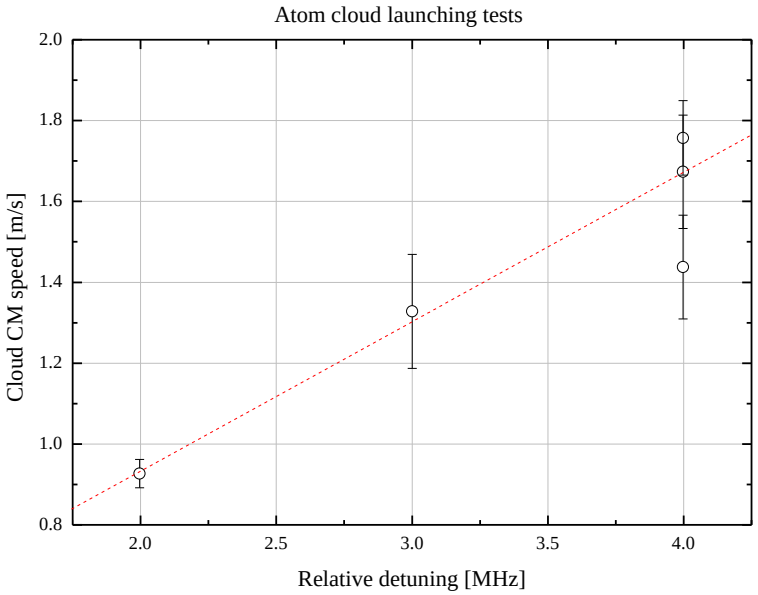

Figure 3.7: Measured speeds of the atom cloud CM, launched by applying different relative detuning $\delta_{\text{rel.}}$ between the upper and lower MOT laser beams, respectively [86].

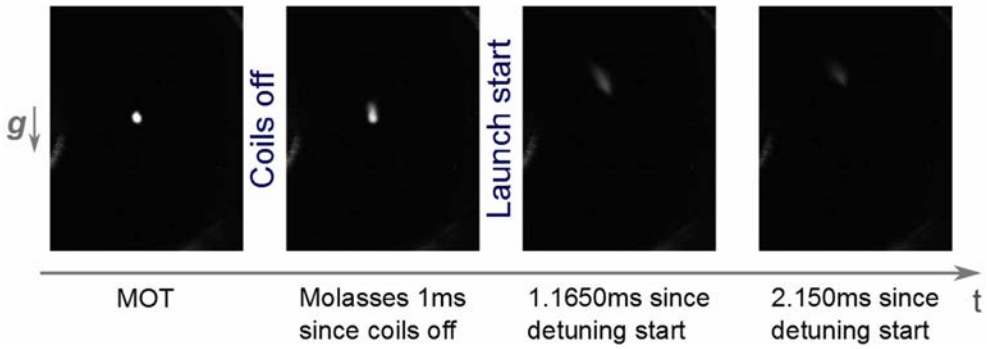

Figure 3.8: Time frame capture from preliminary atom cloud launching tests. The trap coils are switched off and the atoms are given a vertical momentum by applying a relative detuning among the top and bottom 3D MOT cooling beams. Tuneable launch velocities of $\sim$ 1 - 4 m/s were achieved.

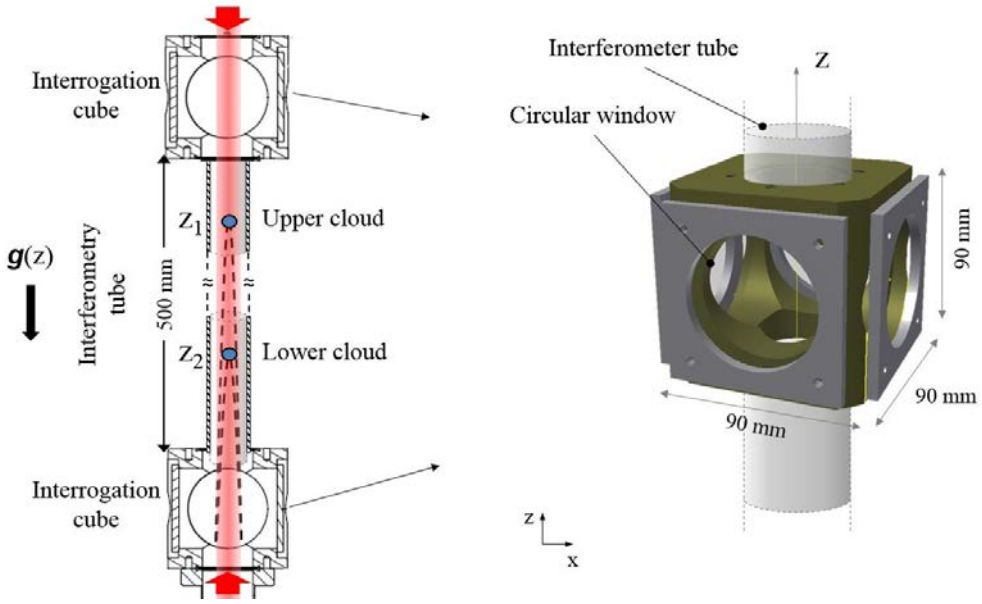

Figure 3.9: Schematic of the interferometry tube, along with a CAD render of one of the interrogation cubes.

Interferometry Section

The interferometric measurement will take place inside a vertical titanium tube of approximately 50 cm length with an inner diameter of 37 mm and 6 mm wall thickness (see fig. 3.9). Two titanium cubes of 90 mm edge are connected at both ends of this tube providing optical access to the detection light through a circular window of 72 mm diameter on each face. After state preparation the cooled atomic ensemble will be launched upwards inside the tube by detuning the upper 3D-MOT cooling laser beams with respect to the lower ones, creating a moving optical molasses. The Raman light beam comes downwards from a telescope mounted on the top window of the tube and retro-reflects on a mirror placed externally at the bottom window of the 3D-MOT chamber. As the light beam travels through the two chamber windows, even small bending on these due to vacuum under-pressure can cause significant wave-front aberrations affecting the interferometric measurement. For this reason a thickness of 20 mm was chosen for the two AR-coated Raman windows which are slightly tilted to prevent the formation of undesired standing waves.

In order for the system to operate as a gradiometer, a differential measurement needs to be performed by launching two sequential cooled atomic clouds at different heights. The interferometric measurement is then performed on both clouds, simultaneously. The separation of the two atomic ensembles for this experiment is considered to be approximately 10-30 cm, depending on the experimental parameters.

A bias field along the interferometric tube is needed to suppress undesired Raman transitions. For this

reason a solenoid was built and placed around the interferometry section. External magnetic fields can impose accelerations onto the atoms as well as energy shifts on their hyperfine levels, affecting the efficiency of the Raman transitions during the interferometric measurement. In order to keep the external fields at a minimum level and uniform within this region, a cylindrical three-layer magnetic shield made of 1 mm thick mu-metal sheet was used. The length and inner diameter values of the successive nested shells are $l_1 = 660.0$ mm, $ID_1 = 150.0$ mm for the inner layer, $l_2 = 670.0$ mm, $ID_2 = 168.95$ mm for the intermediate shell and $l_3 = 680.0$ mm, $ID_3 = 188.97$ mm for the external housing. As this work is focused on the magnetic shielding aspect of the experiment, a more detailed discussion on the shield design and performance will follow in the next chapter.

3.2.1 Telescopes

The optical molasses is realized by cooling laser light coming through the corresponding windows into the vacuum chamber. Light distribution to these points is achieved by a fibre optic network guiding the light to the 2D-MOT and 3D-MOT telescopes.

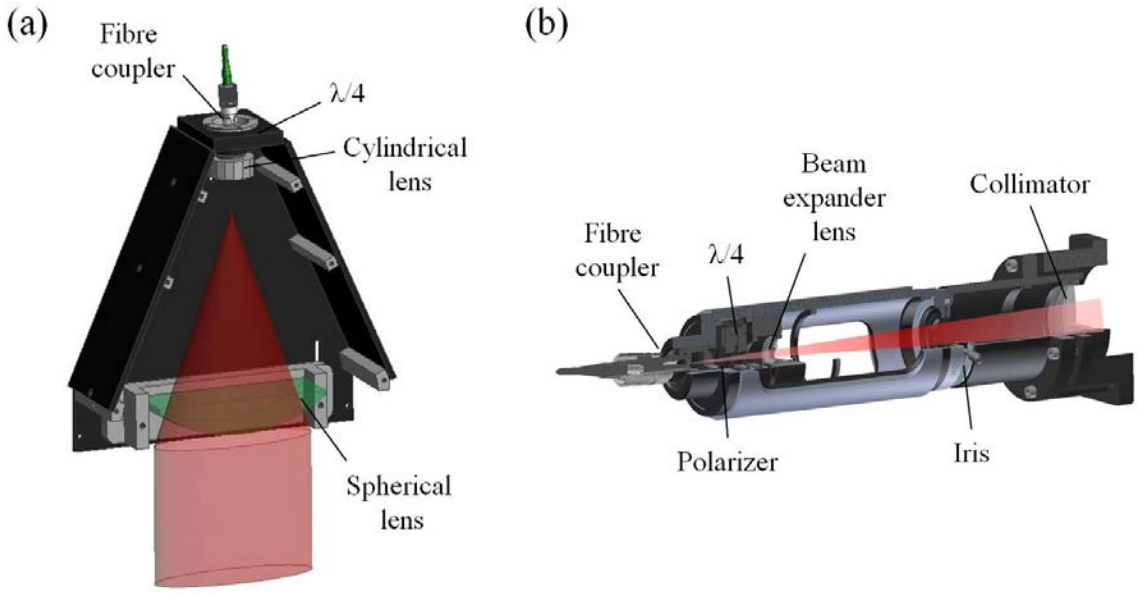

Figure 3.10: CAD renders of the (a) 2D-MOT and (b) 3D-MOT telescopes.

A CAD schematic of the 2D-MOT telescopes is shown in fig. 3.10a. In order to achieve the largest cooling region possible, a wide beam is necessary. The tip of an optical fibre is attached at the top of the structure. The output beam passes through a quarter waveplate and is expanded in one direction via a low focus cylindrical lens. Then, a spherical lens cut in rectangular shape collimates the light in both directions,

forming an elliptical beam which goes through the chamber and retro-reflects on an external mirror at the opposite window. As mentioned previously, a tilted telescope configuration was originally used instead of a pushing beam for transferring the pre-cooled atomic vapour to the 3D-MOT chamber. For this reason, a compact base structure was designed that allows tilt-angles in two axes, providing the appropriate stability at the same time (see fig. 3.11). The telescope's tilt angle with respect to the chamber's longitudinal axis θ is achieved via a hinge installed at its rear end, connecting it to the base frame. An adjustment control of at least $\sim 0.1°$ angle is required, which is reached by extending a micrometer screw mounted on the front end of the telescope. The setting achieving optimal atom transfer to the 3D-MOT chamber was found to be at $\theta = 2.3°$. The base structure also includes two parallel support plates at the two telescope sides for extra stability, as well as several locking screws. In addition, tilt angle control around the chamber's longitudinal axis φ is provided for minor adjustments by two Thorlabs goniometers with locking screws, mounted on each end of the chamber. In order to allow for the option of a pushing beam, if required, a mounting base was designed which extends past the rear window of the chamber and incorporates an Owis 2-axis linear stage with angle adjustment for the corresponding optic fibre collimator.

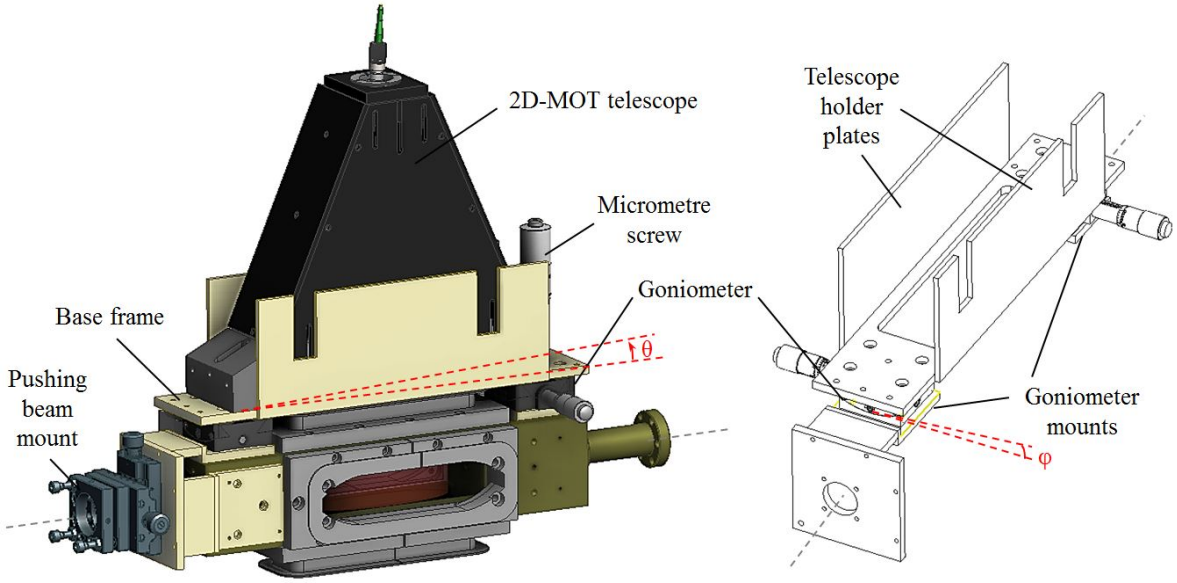

Figure 3.11: CAD render of the 2D-MOT telescope base mechanism which allows for 2-axis tilt. The corresponding tilt angles are adjusted via a micrometer screw at the telescope's front end and the goniometers supporting the two base-frame ends. The telescopes were operated at an optimal tilt angle of $\theta = 2.3°$.

The design of the 3D-MOT telescopes is shown in fig. 3.10b. The optical fibre tip is connected to a fibre coupler at the top and the laser light is directed through a polariser and a quarter waveplate. Then, an

f = −6 mm lens expands the beam which is finally collimated by a 100 mm lens at the end of the telescope.

Lastly, the Raman light telescope is mounted at the top of the interferometry tube. It consists of a polariser at the front of the fibre coupler, and an f = 200 mm collimating lens at its end, forming a beam of 40 mm waist diameter. The beam passes through the bottom window of the 3D-MOT chamber and retro-reflects on an external mirror, situated behind a $\lambda/4$ waveplate.

In addition to cooling, it is important to establish the appropriate imaging methods for detecting and monitoring an atomic cloud. The two main techniques used throughout this experiment are the *fluorescence imaging* and *absorption imaging* which are briefly described below. A more elaborate discussion can be found in [54].

In the first case, the atoms are being illuminated by near resonant light from the MOT beams. Then, the near-infrared radiation from the scattered photons is being detected by a reverse-biased photodiode. By measuring the voltage signal produced by the emitted photon energy within a given solid angle, it is possible to extract information about the atom number. However, the detected signal is weak since the scattered light is distributed in space isotropically. In addition, fluorescence imaging is a destructive method due to the high momentum transfer to the atoms, making it unsuitable for certain measurements.

The absorption imaging technique relies on the opposite principle. The atom cloud is illuminated by a short pulse of cooling light and the target's shadow is captured against the bright background. The attenuation of the light intensity during its propagation through the atomic vapour is correlated to the cloud density and this way, the atom number and temperature can be determined. The short pulse length, typically of the order of 5 µs, makes this method less destructive providing enough signal to noise ratio, but requires a considerable optical access.

The initial detection configuration was realised at the 3D-MOT chamber [86] (see fig. 3.12), while the final detection system was undergoing various iterations until its integration in the interrogation cube at a future step. More details on the latter system can be found in [54]. The detection light is tuned to the atomic resonance and is guided to the 3D-MOT chamber via a polarisation maintaining fibre, forming a collimated beam of 10 mm waist. The detection light illuminates the atoms causing fluorescent radiation, which is then focused onto a photodiode (Thorlabs DET36A) mounted on the chamber's window. Additionally, a charge-coupled device (CCD) camera (Imaging Source DMK42BUC03) was mounted on the opposite chamber window to image the atomic cloud by absorption, with the aid of an adjustable lens.

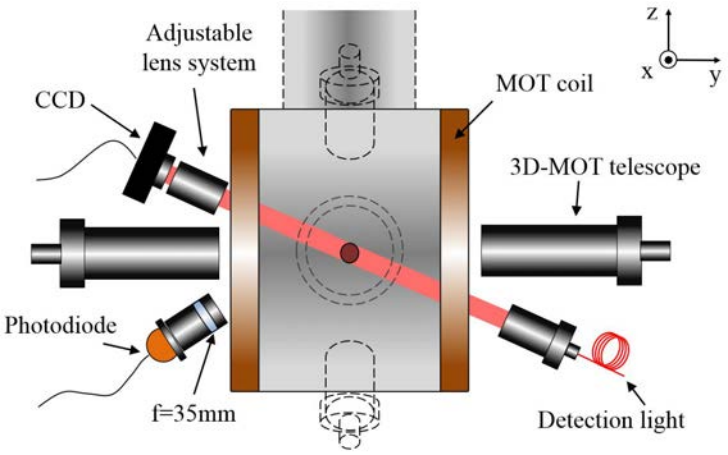

Figure 3.12: Schematic representation of the initial detection system, mounted around the 3D-MOT chamber. A 10 mm diameter beam of detection light illuminates the atomic cloud which is then captured by absorption onto a CCD camera. The atomic fluorescence radiation is detected by a photodiode.

3.3 Laser System

The main requirements for the laser system are stability, compactness and low power consumption. For this reason, a fibre optics network was chosen over an open-space optics system, consisting of optical components such as fibre switches, fibre splitters and acousto-optical modulators (AOM). In order to reduce the power losses and energy consumption the number of lasers and the involved optical components had to be kept at a minimum.

The initial layout of the GGtop laser distribution system is illustrated in fig. 3.13. Although the current setup consists of one set of 2D-MOT and 3D-MOT systems, the experimental scheme can be expanded to support up to three such sets for realising a full gravity tensor sensor in the future. The laser setup incorporates three Newport TLB-6913 Vortex II tunable extended cavity diode lasers (ECDL) with their corresponding servo controllers (Newport LB1005). Each laser can produce an output power of 25 mW light at a central wavelength of 780.24 nm. One of these diode lasers is used as a master laser which serves as a frequency reference and is locked to a rubidium cell spectroscopy reference. The other two diodes are detuned from the master laser and used as a cooling and repumping laser, respectively. Purpose of the cooling laser is to drive the closed cooling rubidium transition from the $5^2P_{3/2}$, F = 3 to $5^2S_{1/2}$, F = 2 state. However, after a large number of cooling cycles the atoms can fall to the $5^2S_{1/2}$, F = 1 state instead, which is out of the cooling cycle. Since this would degrade the cooling efficiency, a repumping laser is used in order to transfer these atoms back into the cooling cycle. 5% of the initial cooling and repumping light output is guided to the beat detection section, to be used for the offset lock. The rest of the cooling laser light is amplified by a

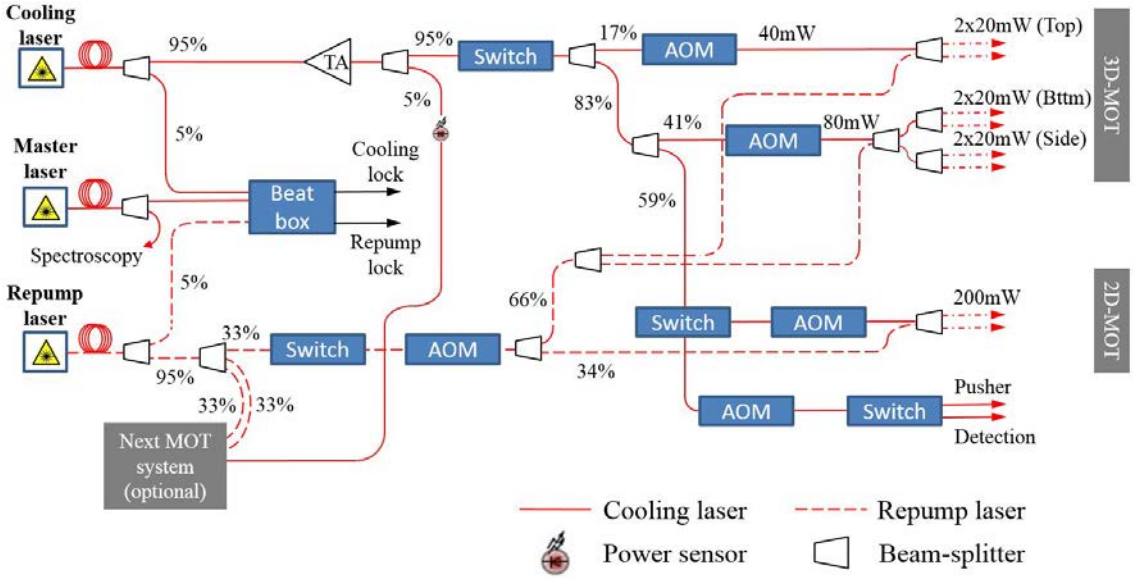

Figure 3.13: Laser distribution system based on a fibre optic network. Fibre splitters, fibre switches, AOMs and other optical components are used for light manipulation and distribution to the corresponding telescope ports.

New Focus TA-7600 tapered amplifier (TA) and is split in two beams of 200 mW and six beams of 20 mW, for the 2D-MOT and 3D-MOT telescopes, respectively. It was found that further light power was required for the 2D-MOT in order to cool a higher density of atoms, which was amended later by the implementation of a second TA. The rest of the components included in the above scheme are polarization maintaining fibre splitters from Evanescent Optics, AOMs from Gooch & Housegoo (Fibre-Q), and mechanical fibre switches from LEONI.

In order to be able to interact with the atoms it is important for the laser frequency to be stable enough and well controlled. For this reason the master laser is used as a frequency reference to the other lasers, tuned to the $F = 2 \rightarrow F' = 3$ transition of the rubidium-87 D_2 line. The technique used to stabilize its wavelength is *modulation transfer spectroscopy* [105]. Advantages of this technique are the sub-Doppler resolution and a zero background signal with zero crossings centred at the atomic transitions, indicating large peak-peak amplitude at the closed transitions. In addition, the lineshape baseline is independent of changes in absorption, temperature and light intensity. A schematic of the used spectroscopy system is shown in fig. 3.14. A high intensity light source is required for producing the Raman light in order to drive the desired Raman transitions onto the atoms. For this reason, an NP Photonics Rock Fibre Laser was used as a source for the Raman light, which provides a very narrow linewidth at 1560 nm with a maximum output power of 30 mW. The schematic of this setup is shown in fig. 3.15. The seeding light is guided through an EOM

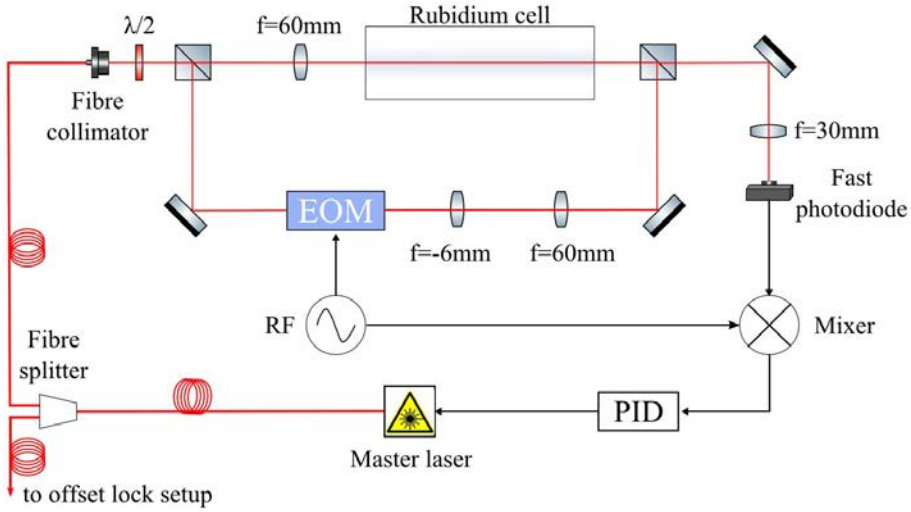

Figure 3.14: Spectroscopy scheme based on rubidium cell as an absolute frequency reference.

which adds sidebands to the signal by frequency modulation. The separation from the central frequency corresponds to the ^{87}Rb F = 2 - F = 1 ground state difference of 6.835 GHz. A schematic of the microwave source used for this modulation is shown in fig. 3.16. The light is then amplified by a table-top high power optical amplifier from BKtel photonics (THPOA-SFP427-FCAPC-C50) with a maximum output power of 13 W. Then, by using a frequency doubling crystal the desired wave of 780 nm is produced, including the transition side-bands. The output light is then coupled into an optic fibre and is guided to the Raman telescope, while an AOM is used as a fast switch before the fibre. Considering that a typical experimental time-length for a $\pi/2$-pulse is of the order of $\sim 10\,\mu s$, it can be deduced that a switching speed of $< 1\,\mu s$ is required.

A sensitive parameter for the laser distribution system is the polarization stability. Polarization variations can affect the MOT efficiency considerably, causing asymmetries on the optical molasses or even complete loss of cooled atoms. For this reason the light is distributed via polarisation-maintaining (PANDA) optical fibres, while a polariser is included in each of the 3D-MOT telescopes.

Light intensity stability is also another essential parameter in order to create a well formed optical molasses. Intensity imbalances among the MOT beams can result in optical net forces pushing the cooled atoms away from the trap centre. For this reason, careful light splitting through the fibre beam splitters is required in order to achieve the right power ratio among the different ports.

Finally, as the optical properties of an optical fibre are temperature dependent, the implementation of a reliable temperature control system is essential in order to provide temperature stability. For this reason peltier elements are used for monitoring temperature variations at different sections within the system.

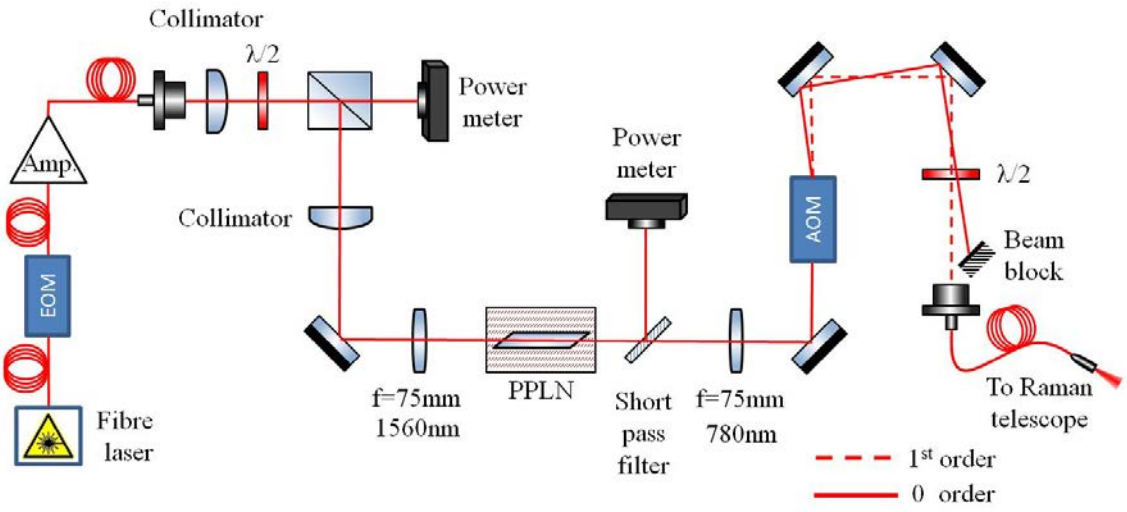

Figure 3.15: Schematic of the experimental setup used for the production of the Raman light. A beam of 1560 nm laser light is initially frequency modulated by an EOM to create sidebands corresponding to the ^{87}Rb F = 2 - F = 1 ground state difference of 6.835 GHz. The modulated light is then amplified and guided through a frequency doubling crystal, converting it to 780 nm light. Finally, the output beam is coupled into an optical fibre and guided to the Raman telescope. An AOM placed before the fibre serves as a fast switch.

3.4 Electronics Package

An efficient computer control system is needed in order to control the experimental process which involves various electronic and electro-optical components that need to be controlled and synchronised with accuracy. Considering that the time-length of a typical interferometric pulse is of the order of $\sim 10\,\mu$s, a resolution of well below $1\,\mu$s is required. The computer-apparatus communication is achieved by a serial communication interface via a field-programmable gate array (FPGA) (NI sbRIO-6932) with a maximum resolution of 5 ns, while the experimental sequences were programmed in LabVIEW code. The architecture of the computer control system is based on a main interface which is in bidirectional communication with the sub-programs that control the individual devices. The main interface provides monitoring of the important experimental parameters, such as the signal frequencies and amplitudes on the DDSs, as well as brief diagnostic messages. The control of these parameters is performed centrally, without the need of calling the individual sub-programs manually. In addition, the user environment provides a flexible way for composing the desired experimental sequence to be sent to the involved devices. All the experimental parameters can then be saved in table form as a "recipe", that can be called back again later.

Most of the electronics devices are hosted in a rack next to the sensor (see fig. 3.17a). It mainly caries two Novatech 409B direct digital synthesizers (DDS), which can create arbitrary waveforms from an

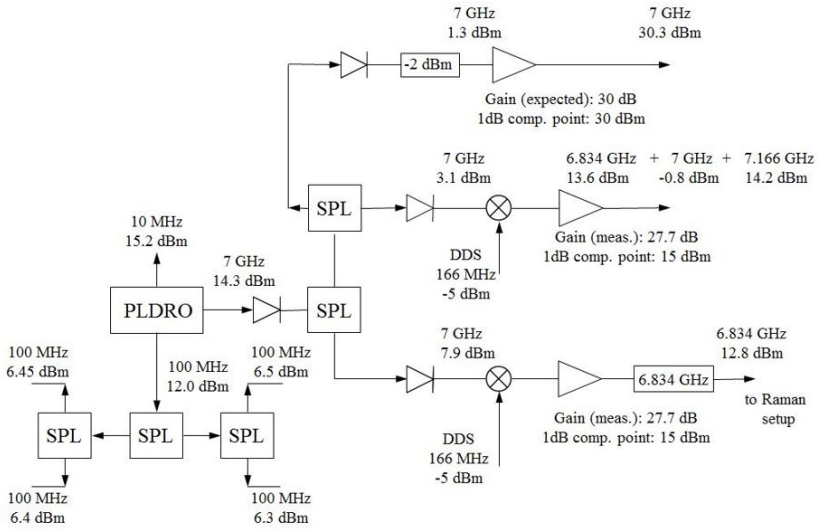

Figure 3.16: Diagram of the microwave chain providing 6.834 GHz to the Raman setup.

internal frequency reference clock, an oscillator-mixer circuit, three Newport LB1005 Servo Controllers for the master, cooling and repumping lasers, with the corresponding laser controllers (New Focus Vortex 6000). A four channel Rohde & Schwarz digital power supply is used to control the compensation coils surrounding the 3D-MOT chamber, while four Delta Electronika ES 030-10 power supplies drive the trap coils on the 2D-MOT and 3D-MOT chamber, respectively. During certain experimental steps (like atom launching), residual magnetic fields could affect the atomic trajectory and cause unwanted Zeeman-shifts. For this reason, IGBT fast switches have been implemented to the setup for rapid power extinction. A Yokogawa DL7440 oscilloscope is also included to monitor waveforms of interest such as the spectroscopy and photodiode signals. A liquid crystal display (LCD) is mounted on the rack frame and is connected with two CCD (DMK 31BU03) cameras to provide real time monitoring of the atomic clouds inside the 2D-MOT and 3D-MOT chambers. Finally, two uninterruptible power supplies (UPS) from Power Solve provide the appropriate protection to the above devices.

A tree diagram of the communication with the main hardware components is presented in fig. 3.17b. Some of the first level operations that the main interface provides is the control of the signal frequency, amplitude and phase of the DDSs, which are sent to the AOMs that control the lasers for the cooling light, Raman light and RF signal. It also sends signals to the fibre switches for laser light extinguishing, the IGBTs connected to the MOT coils for rapid field switch-off, and camera control. More details on the electronics package can be found in [86].

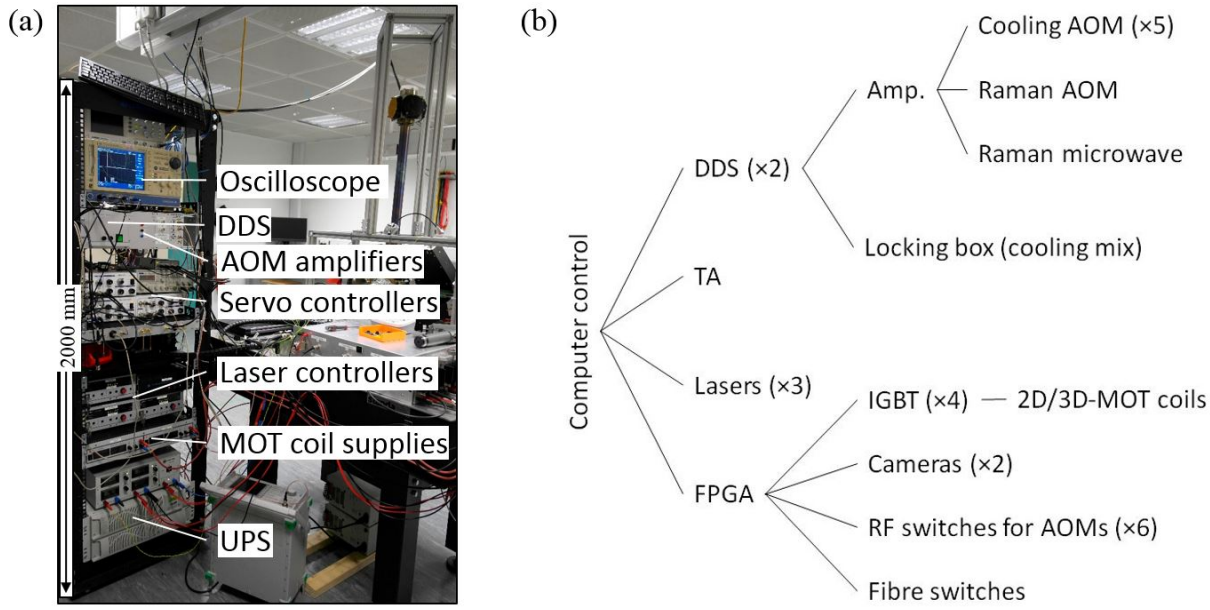

Figure 3.17: (a) Picture of the rack carrying the majority of the electronic systems and (b) tree diagram of the electronics control by the main interface program [86].

3.5 Interferometic Sequencies

Once achieving the appropriate MOT and molasses phase conditions, the most fundamental step required on realising an atom interferometer is to establish control on the atomic state transfer.

At the first stage, the atom cloud was illuminated with Raman light of different pulse lengths τ and the resulting number of atoms for each state was derived by fluorescence detection. Figure 3.18 shows an example of experimental data where the detected population ratio is plotted over the exposure time, demonstrating an oscillatory behaviour known as Rabi oscillations. The fast decaying trend of the experimental oscillation is mainly owed to two reasons. The first reason is related to the level of the vacuum inside the chamber, which was barely reaching 10^{-9} mbar during the period of these measurements. This could increase the collisions with the atoms of the background gasses and compromise the cloud coherence. The second cause is the population loses over time due to inefficient state transitions. The results could be improved by spotting and healing any potential leakages across the vacuum system, in order to establish a pressures of $< 10^{-9}$ mbar. In addition, good magnetic field management would enhance the atomic transitions' efficiency. A uniform and stable magnetic field bias is required to create a well defined quantization axis for the atoms. At the same time, potential interactions of the atoms with stray magnetic fields can be minimised by sufficient magnetic shielding. The exposure time that corresponds to equal state population ratio defines the duration

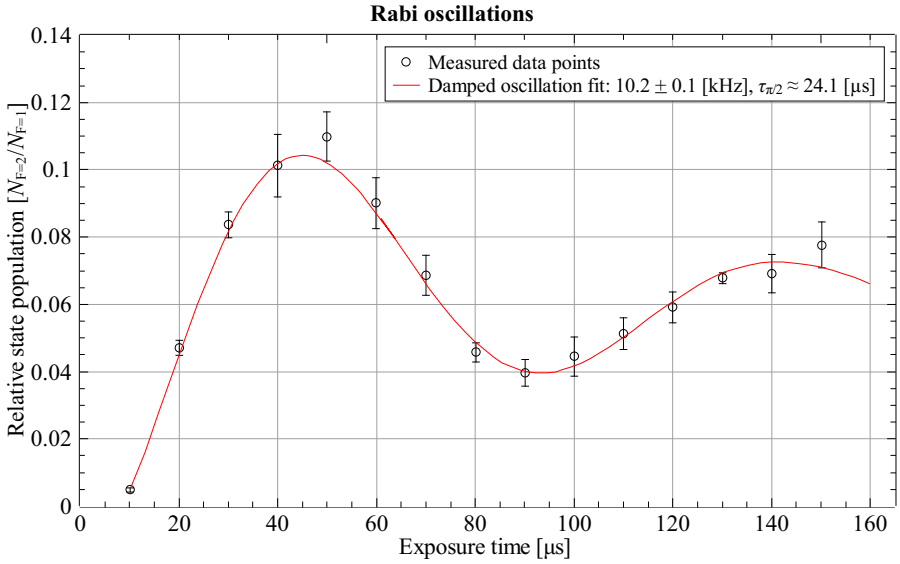

Figure 3.18: Detection of Rabi oscillations as measured on GGtop [54]. Each data point indicates the relative atom population transferred from the $|F = 1\rangle$ state to $|F = 2\rangle$, as function of exposure light. For this experiment, an intensity of 98 mW/cm^2 was used for the Raman light with 1.3 GHz detuning. The plotted data points are normalised to the MOT fluorescence signal.

for a $\pi/2$-pulse. Once $\tau_{\pi/2}$ is determined a full interferometer can be realised based on that. The pulse length for this case was determined to $\tau_{\pi/2} \approx 24\,\mu s$ [54]. The experimental sequence used during the above process is summarised in the schematic representation in fig. 3.19.

In the next stage, interferometric measurements were realised by using a similar sequence with the previous one, this time by introducing two successive $\pi/2$ Raman pulses, separated by a free evolution time $T = 100$ ms. If no phase shift has been accumulated on the atomic wave-packet during this time, then the two successive $\pi/2$-pulses together will act as a π-pulse causing all the atomic population to be transferred at the same state. However, if the two wave-packets end up with a relative phase difference, it will cause interference. Figure 3.20 shows experimental interference fringes from recent measurements on GGtop, by plotting the detected population state ratio while scanning the frequency detuning relative to the central line $\delta = \omega - \omega_0$.

3.6 Summary

The purpose of this chapter was to provide an overview on the GGtop experimental apparatus, along with some of the current results. Since the system is meant to operate as a transportable sensor, certain design choices were made in order to minimise complexity, size and weight. The experimental apparatus is

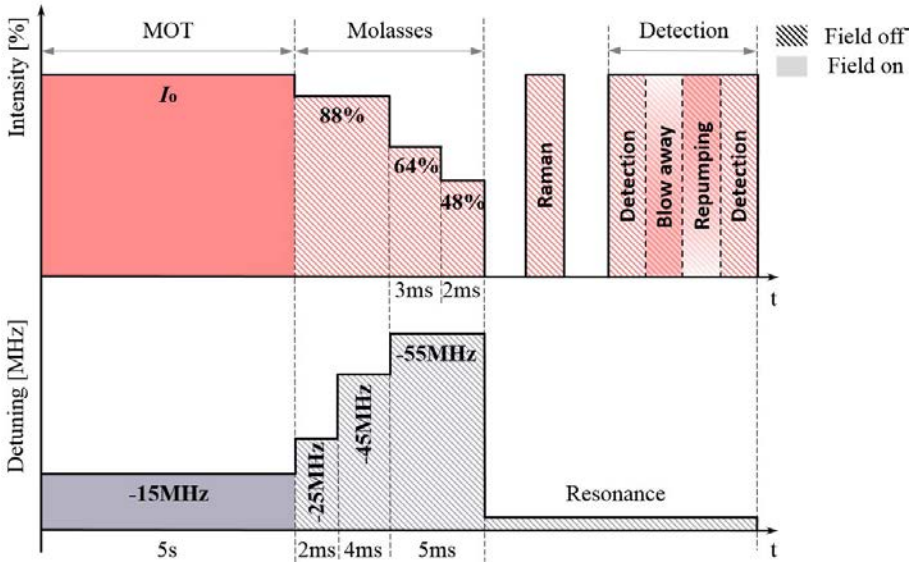

Figure 3.19: Experimental time sequence used to detect Rabi oscillations. The trap magnetic field is switched off and a molasses phase is introduced for sub-Doppler cooling and state preparation to the F=2 ground state. Raman pulses of varying lengths are applied, followed by population state detection. The pulse length resulting to an equal population state ratio defines $\tau_{\pi/2}$.

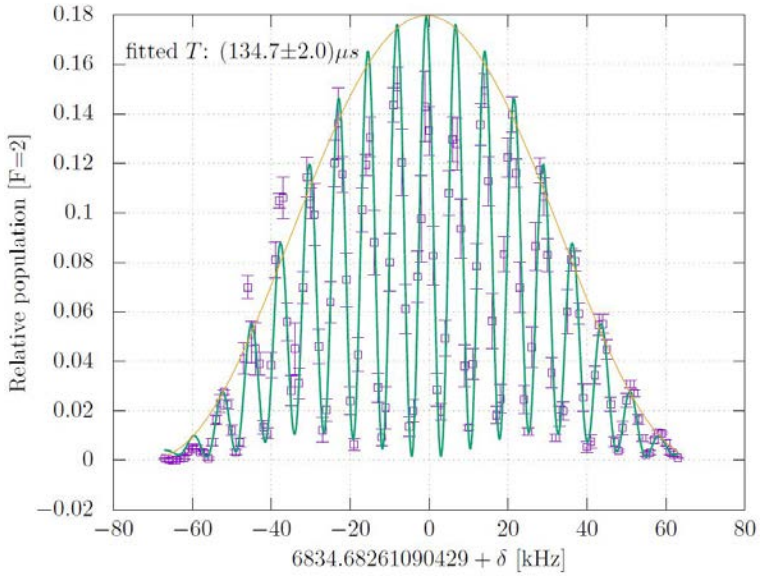

Figure 3.20: Experimental data from Ramsey fringes detection showing the relative atom population in the $|\mathrm{F} = 2\rangle$ state as a function of light detuning δ. The detected population signal is normalised to the MOT fluorescence prior to molasses cooling. A detuning step of 1 kHz was used for Raman pulses with a length of $\tau_{\pi/2} = 13.9\,\mu\mathrm{s}$, separated by $134.7\,\mu\mathrm{s}$ (picture copied from [54]).

organised in two main modules. The first module is the physics package which includes the vacuum chamber system with the magnetic shield and the laser system with its peripheral sub-modules. The second module

is the electronics package which is carried on the electronics' rack and contains the appropriate devises for the RF signal generation, switching and timing during the experimental sequence. The GGtop apparatus incorporates a relatively uncommon scheme for its laser light distribution system, which was originally based on fibre optics. The primary reasons for preferring an all in fibre scheme over a commonly used free space optics system were its enhanced compactness and robustness. In contrast, a free space system is expected to be larger, heavier and more susceptible to drifts.

A 3D-MOT with a number of atoms of the order of $\sim 10^8$ and a cloud temperature of $\sim 4\,\mathrm{mK}$ was initially realized on GGtop. Then, by using the polarisation gradient cooling technique, this temperature was reduced considerably, reaching typical values of $\sim 50\,\mu\mathrm{K}$. Although this sequence was not optimised yet, it allowed for atom cloud launching and preliminary interferometry tests. The moving molasses technique was used for launching the atoms in the vertical direction, by applying a relative detuning among the upper and lower MOT telescopes. During these trials, tunable initial cloud velocities of the order of $\sim$ 1 - 4 m/s were achieved, which are typical for an atomic fountain of this size [65, 101]. The last step that was achieved by the end of this work was the realization of a basic interferometric sequence. Initially, Rabi oscillations were observed by illuminating the atoms with Raman light to induce stimulated transitions between the two ground states. This way, the exposure time required for realising a splitting $\pi/2$-pulse was determined to $\tau_{\pi/2} \approx 24\,\mu\mathrm{s}$. At this stage, preliminary interferometric measurements were conducted by applying a sequence of two $\pi/2$-pulses onto the atoms, separated by a free evolution time of $T \approx 130\,\mu\mathrm{s}$. Despite the fair contrast, the observed Ramsey interference fringes proved that the current experimental setup is capable of realising interferometric measurements.

However during the course of the above work, the system encountered stability issues that limited the control and reproducibility of the experimental process. These instabilities are depicted on the atom number, shape and position of the cold atomic cloud. In addition, the minimum achieved temperature was limited to $\sim 20\,\mu\mathrm{K}$, which is an order of magnitude higher than the experimental requirements for gravity sensing [60, 65, 101]. A relatively high cloud temperature, will cause a wide spread in the velocity distribution of the atoms, resulting in a rapid expansion of the cloud after launching. This will have a negative impact on the interferometric measurements, since many atoms will escape from the Raman beam and will be lost on the chamber's walls. Therefore, a lower number of atoms will contribute to the interferometric signal, resulting in a reduced fringe contrast. The main factors that are related to these issues are discussed below.

Starting from the MOT, the major causes of the observed instabilities are related to light polarisation fluctuations and environmental temperature variations. A thorough investigation was undertaken to identify

the causes of the light instabilities within the laser delivery system, which is presented in more detail in previous work [54,86]. These are mainly attributed to variations in the refractive index across the polarisation maintaining optical fibres (PANDA type), which are caused by temperature fluctuations and mechanical stresses.

Temperature variations can affect the light polarisation within an optical fibre, since the refractive index of its material is temperature dependent. These changes are either local, depending on the particular section of the setup, or environmental and they vary in hourly and daily basis. In addition, the splitting ratio of the fibre splitters that are responsible for the light distribution among the MOT telescopes is also affected by temperature. According to the manufacturer, this ratio can vary by $\sim 0.186\%$ per $^{\circ}$C. Previous experimental observations on the 3D-MOT over the course of a day, indicated typical light power fluctuations of the order of $\sim 15\%$, which were caused by temperature variations in the lab environment [86].

Another source of the observed instabilities is affiliated with the mechanical stresses that can be induced in the optical fibres. Any applied external stresses due to bending, twisting, or temperature variations will cause birefringence in the fibre material and affect the supported mode of the propagating linearly polarised light. This can result in light leakage and generation of parasitic modes which will interfere with the supported mode. Furthermore, the laser light has to travel through a considerable length of optic fibre which has to be connected to multiple components such as fibre splitters and fibre switches via splices (see fig. 3.13). Any coupling imperfections at the splicing points or on the fibre collimators will add up to the above errors. Once the light exits the tip of the fibre, it goes through a waveplate that allows only light components of the same polarisation to pass through. As a result, any relative phase offsets of the light will be converted to intensity variations across the MOT light beams. These fluctuations can explain the observed shifts of the centre of the trap [86] as well as the formation of varying trapping patterns [111].

Measurements that were conducted on the 3D-MOT fibres during previous work [54], indicated light intensity variations of $\sim 2.7\%$, on average. This results in a residual force that is imposed on the atoms at the centre of the MOT, affecting the cooling efficiency. In the same work, the estimated horizontal acceleration that is imposed on the atoms by this force could reach values of the order of $\sim 500\,\mathrm{m/s^2}$ (worst case). This acceleration is enough to force the atoms to collide with the chamber's walls after launching, making an interferometric measurement impossible.

Finally, insufficient magnetic field compensation can also affect the shape of the atom cloud, its position and temperature. As shown previously, the sub-Doppler cooling stage is realised before launching the atoms by ramping the frequency and intensity of the MOT beams, while the trapping magnetic field is extinguished.

Any stray magnetic fields will interact with the atom cloud and affect the experiment in various ways. Firstly, the magnetic force will accelerate the atoms causing a fraction of the population to escape from the cooling region, while the remaining atoms will not reach the desired temperature due to the increased spread in the velocity distribution. In addition, the residual magnetic fields can affect the launching control, since the magnetically induced forces can impose horizontal accelerations on the atoms that will affect their trajectory. Lastly, the bias field that determines the atom quantization axis was poorly controlled at this stage, degrading the efficiency of atom interactions with the Raman light during the interferometry stage.

In addition to the above, the experimental progress was hindered by failures that occurred several times on the mechanical fibre switches that are incorporated in the laser distribution system. These switches are used for complete extinction of the laser light and are located before the fibre splitters that are responsible for the light distribution among the MOT telescopes (see fig. 3.13). Replacing these components is a tedious and time consuming work which requires integration in the fibre network via splicing.

The above discussion dictates that the system needs to undergo further optimisation in order to progress towards gravity sensing. One of the tasks for future work is to build a temperature stabilisation system that will mitigate temperature drifts and ensure a better light beam balance. In addition, the ability for fine tuning of the temperature conditions across the laser light system will allow for further optimisation on the light splitting ratio among the MOT telescopes. Another area for future work is related to the laser distribution system. The laser light has to travel through a lengthy optical fibre network with multiple components and splices, causing any occurring errors to accumulate and compromise the MOT efficiency. Therefore, the current system needs to be changed by a new setup with reduced complexity and number of components. Also, further investigation needs to be undertaken in order to find more reliable replacements for the mechanical fibre switches. Additional room for improvements can be found on the experimental sequence controlled by the LabView script. For instance, the polarisation gradient cooling stage could be improved by optimising the timings and increasing the number of steps in the light intensity and frequency sequence, to produce a smoother ramping. This could potentially improve the cooling efficiency and reproducibility. Regarding the drifts and fluctuations owed to mechanical vibrations, these can be suppressed by the installation of a stabilisation platform with vibration isolation capability. Lastly, sufficient magnetic shielding is required in order to minimise undesired Zeeman shifts and accelerations on the atoms during the experimental sequence. Although the interferometry section is currently shielded by a three-layer magnetic shield, further optimisation can be achieved by degaussing, which is briefly discussed in §4.1.2. The impact of the external magnetic fields on the 3D-MOT section is suppressed by a compensation coil system which is operated manually. This can

be upgraded to an active compensation system by implementing the appropriate feedback control electronics. Alternatively, the installation of an additional passive shield of mu-metal in this section could provide the appropriate field attenuation, without the need for specialised electronics.

In conclusion, the capability of realising interferometric measurements on the GGtop system has been demonstrated. However, unexpected issues have been encountered in the effort of gravity signal acquisition. It turned out that although the approach of using a fibre optics laser distribution system drastically enhanced system portability, it led to polarisation fluctuations which in return create long-term limitations in stability. In addition, multiple failures on the mechanical fibre switches delayed the overall experimental progress. The GGtop system is currently using a free-space system for laser cooling and is optimised for launches, while tests for gravity measurements are being undertaken.

CHAPTER 4

MAGNETIC SHIELDING

Stray magnetic fields are known to cause undesired effects in many applications like auto-transformers, magnetic memory storage, magnetic imaging, and others. For this reason, certain techniques need to be applied in order to keep external magnetic fields away from a particular region, known as magnetic shielding. As discussed in §2.5.3 atoms are sensitive to stray magnetic fields, making magnetic shielding a crucial aspect on the design of an atom interferometer. This stems from the fact that the atoms are susceptible to magnetically induced accelerations due to the second order Zeeman effect. Such effects may have a considerable impact on the interferometric measurement and need to be suppressed. A magnetic shield providing a shielding factor of $\sim 10^3$ will enable measurements of human size targets, that correspond to signals of the order of $10^{-9}g_0$ (see fig. 2.15).

Magnetic shielding techniques are divided in two main categories, passive and active magnetic shielding. Passive magnetic shielding relies on materials demonstrating special magnetic properties like ferromagnets and superconductors. Ferromagnets possess very high relative magnetic permeability values (μ_r), typically of the order of 10^3 to 10^6. Due to its high permeability, a ferromagnetic material provides an easier path to the magnetic flux, diverting it away from the area to be shielded. A superconductor on the other hand behaves in the exact opposite way in the sense of perfect diamagnetism, the ability to expel any magnetic fields completely from its body, also known as the *Meissner effect*. However, this requires cryogenic conditions which pose practical difficulties such as the need of special equipment that increases the total weight, dimensions and running-cost.

Active magnetic shielding [61,118] is achieved by a system consisting of compensation coils and a magnetic sensor connected to a feedback loop circuit. The sensor monitors the external magnetic field in real time

and drives the feedback system which controls the current sent to the coils to produce the appropriate compensating field.

A brief theoretical overview on the fundamentals of magnetic shielding is presented at the beginning of this chapter, followed by a numerical approach. Finally, a discussion on the magnetic shielding approach for the GGtop sensor will be given along with the magnetic test results.

4.1 Magnetic Shielding Fundamentals

4.1.1 Analytical Treatment - Shielding Factors

The study of a magnetic shielding problem starts from the simplified case of a homogeneous ferromagnetic body placed within a uniform magnetic field. The theoretical approach in the following formulation was adopted from [108]. In this discussion, an infinite cylindrical shell of relative permeability μ_r will be considered, as shown in fig. 4.1, however the same treatment can be generalized for an arbitrary geometry. The magnetic field induction in empty space is given by $\mathbf{B}_0 = \mu_0 \mathbf{H}_0$, where μ_0 is the magnetic constant and $\mathbf{H}$ the magnetic field (or magnetizing force). The presence of the highly permeable ferromagnetic material

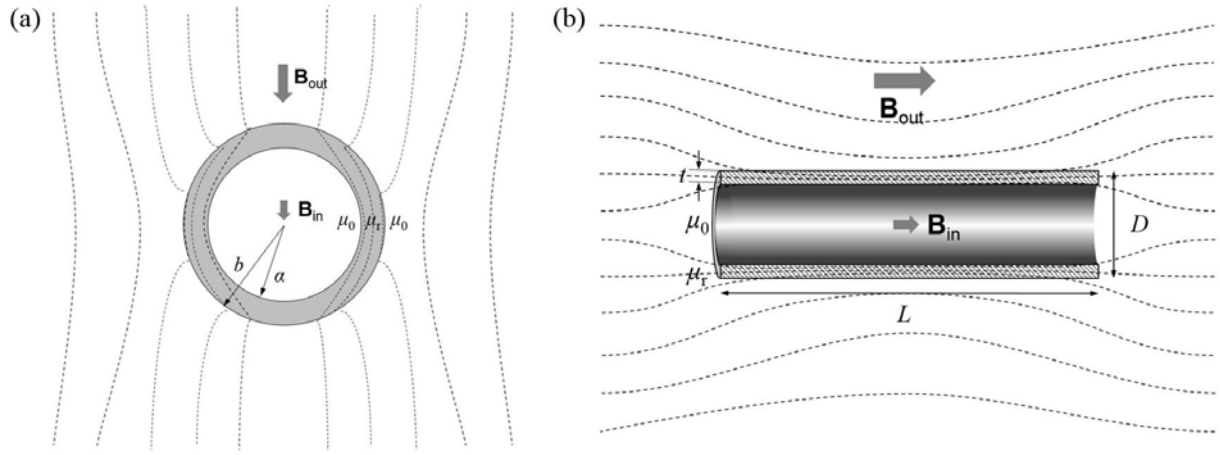

Figure 4.1: Representation of the cross-section of a cylindrical ferromagnetic shell within a (a) transverse and (b) axial magnetic field, respectively. The incident magnetic flux preferably follows the path through the highly permeable material, keeping away from the shielded area.

will affect the magnetic flux Φ, which will tend to flow through the "easiest" path that the material provides. The field vectors $\mathbf{B}$ and $\mathbf{H}$ can be derived by solving the boundary–value problem for the magnetic scalar potential V_m in each region, where $\mathbf{H} = -\nabla V_m$ [55]. Since $\mathbf{B} = \mu\mathbf{H} = \mu_0(1-\chi)\mathbf{H}$ with χ being the material's magnetic susceptibility, the divergence Maxwell equation becomes $\nabla \cdot \mathbf{H} = 0$ in all regions. Therefore, V_m

satisfies the Laplace equation for all points in space. The scalar potential for each region is then given in polar coordinates by

$$\begin{aligned} V_1 &= -\mathrm{H}_0 r\cos\theta + \tfrac{1}{r}\mathrm{B}_1\cos\theta, && r \geq b \\ V_2 &= \mathrm{A}_2 r\cos\theta + \tfrac{1}{r}\mathrm{B}_2\cos\theta, && a \leq r < b \\ V_3 &= \mathrm{A}_3 r\cos\theta, && 0 \leq r < a, \end{aligned} \tag{4.1}$$

where $\mathbf{A}$ is the vector potential, r the distance from the centre and θ the angle with respect to the external field orientation. The subscripts $i = 1, 2$, and 3 correspond to the region outside the housing, inside the ferromagnetic body and inside the housing, respectively. The boundary conditions dictate that the normal component of $\mathbf{B}$ and the tangential component of $\mathbf{H}$ should be continuous

$$\mathbf{H}_{i'} \cdot \mathbf{n} = \frac{\mu_i}{\mu_{i'}}\mathbf{H}_i \cdot \mathbf{n}, \qquad \mathbf{H}_{i'} \times \mathbf{n} = \mathbf{H}_i \times \mathbf{n}. \tag{4.2}$$

$$\mathbf{B}_{i'} \cdot \mathbf{n} = \mathbf{B}_i \cdot \mathbf{n}, \qquad \mathbf{B}_{i'} \times \mathbf{n} = \frac{\mu_{i'}}{\mu_i}\mathbf{B}_i \times \mathbf{n}. \tag{4.3}$$

Differentiation of V_m gives the solutions of $\mathbf{H}$:

$$\begin{aligned} \mathrm{H}_1 &= \mathrm{H}_0\hat{i} + \tfrac{1}{r^2}\mathrm{B}_1(\cos 2\theta\hat{i} + \sin 2\theta\hat{j}), && r \geq b \\ \mathrm{H}_2 &= -\mathrm{A}_2\hat{i} + \tfrac{1}{r^2}\mathrm{B}_2(\cos 2\theta\hat{i} + \sin 2\theta\hat{j}), && a \leq r < b \\ \mathrm{H}_3 &= -\mathrm{A}_3\hat{i}, && 0 \leq r < a. \end{aligned} \tag{4.4}$$

Characteristic measure of magnetic shielding performance is the amplitude ratio of the magnetic field without the presence of the shield, over the residual field measured at the same point after the shield installation. This ratio is known as the *shielding factor*

$$\mathrm{S} = \frac{\mathrm{B}_{\mathrm{out}}}{\mathrm{B}_{\mathrm{in}}}. \tag{4.5}$$

The shielding factor is a function of the material's magnetic properties and the housing's geometry. Analytical approximations for basic geometries are available in literature as follows.

Spherical housings provide the most optimum shielding factor given by [72]

$$\mathrm{S} = \frac{4}{3}\mu_{\mathrm{r}}\frac{t}{D} + 1, \quad (t \ll D) \tag{4.6}$$

where D is the outer diameter, t the wall thickness, and $\mu_{\mathrm{r}} = \mu/\mu_{\mathrm{o}}$ the *relative magnetic permeability.*

However, they are rarely being used in practice since they consume a lot of space and in most applications, openings are required to allow access inside the enclosure.

A more practical solution is the cylindrical shell, which is the most commonly used geometry. In the case of a very long cylinder under a transverse magnetic field (see fig. 4.1a), the shielding factor is approximated by [72]

$$\mathrm{S_t} = \mu_\mathrm{r}\frac{t}{D} + 1, \quad (t \ll D). \tag{4.7}$$

For a finite cylinder inside an axial (longitudinal) external field (see fig. 4.1b), the shielding factor expression takes the form [72]

$$\mathrm{S_a} = 4N\mathrm{S_t} + 1, \ \text{(open ends)} \tag{4.8}$$

$$\mathrm{S_a} = \frac{4N\mathrm{S_t} + 1}{1 + \frac{D}{2L}}, \ \text{(closed ends)} \tag{4.9}$$

where L is the cylinder's length and N the *demagnetization factor* [30, 64, 71], which is related to certain geometrical characteristics. For a cylinder with closed ends

$$N \approx 0.38\left(\frac{L}{D}\right)^{-1.3}, \quad \text{for} \ \ 1 \leq L/D \leq 10. \tag{4.10}$$

In the above formulae, end effects that would rise close to the cylinder's ends are neglected. Also, equations (4.8) and (4.9) indicate that the axial shielding factor is lower than the transverse factor (4.7). For this reason, it is a common practice to use end-caps in order to achieve a better field attenuation. In this case, conical shaped end-caps [76] can provide a better improvement over the flat caps. A bit more complicated expressions for the above shielding factors can be found in the literature, which consider various corrections and certain geometrical variations, like in [23, 40, 72, 90, 117].

Finally, cubic geometries come third in place in terms of shielding efficiency. This is mainly owed to the higher residual field density close to the edges, and especially the corners. An average shielding factor for a cubic enclosure with an edge–length a can be estimated by [62]

$$\mathrm{S} = \frac{4}{5}\mu_\mathrm{r}\frac{t}{a} + 1. \tag{4.11}$$

In some applications where a high shielding efficiency is required, it is a common practice to use multiple nested shielding shells to increase the field attenuation. An elegant approach for calculating the shielding factor of multi-layered housings is given in [128], where the shielding structure is represented as a magnetic

circuit [32]. The shielding factor can then be derived by defining the magnetic flux for the equivalent magnetic circuit problem.

In the case of a dual-layered cylindrical shield, (4.7) takes the form [117]

$$\mathrm{S} \approx 1 + \mathrm{S}_1\mathrm{S}_2 + \frac{\mathrm{S}_1\mathrm{S}_2}{2}, \quad (D_2 = 1.5D_1,\ t/D_2 \ll D_1/D_2) \tag{4.12}$$

where S_1 and S_2 correspond to the outer and inner shell efficiencies, respectively. The above expression shows that two nested shells act multiplicatively instead of additively. This means that for a given amount of material, the shielding factor can be increased significantly by introducing an air-gap in the form of a dual-layer separation. The optimum air-gap value which maximizes the shielding factor for this case is investigated numerically in [88] and approximated by $\Delta_o \approx 0.73D_2$. Furthermore, it is shown that for an infinitely long dual-layered cylindrical shield, a structure comprising of shells of equal-mass provides a better performance per unit mass compared to a combination of two shells of equal-thickness, which is commonly used in practice [88]. A generalised form for the transverse and axial shielding factors of i nested cylindrical shells is given by [38]

$$\mathrm{S}_{\mathrm{t,tot}} \approx \mathrm{S}_{\mathrm{t},n} \prod_{i=1}^{n-1} \mathrm{S}_{\mathrm{t},i} \left[1 - \left(\frac{D_{i+1}}{D_i}\right)^2\right], \quad (D_i > D_{i+1}) \tag{4.13}$$

$$\mathrm{S}_{\mathrm{a,tot}} \approx \mathrm{S}_{\mathrm{t},n} \prod_{i=1}^{n-1} \mathrm{S}_{\mathrm{t},i} \left[1 - \left(\frac{L_{i+1}}{L_i}\right)\right], \quad (L_i > L_{i+1}) \tag{4.14}$$

Other theoretical approaches for multi-layered shields can be found in [87, 117]. As discussed previously in §2.5.3, a shielding factor of at least 10^3 is required for the experimental region of the GGtop interferometer. In addition, the magnetic field gradient caused by the shield's ends is also important, because it gives rise to the second order Zeeman effect. This translates to magnetically induced accelerations onto the atoms, which affect the measured gravitational signal. As indicated in fig. 2.15, in order to measure a signal of $\sim 10^{-9} g_0$ that corresponds to a human size object, a field gradient of $\lesssim 10^{-3}\mu\mathrm{T/mm}$ is required. An analytical approximation of the magnetic field profile close to the shield's open ends can be derived from (4.5) and (4.17).

The above discussion refers to DC or extremely low frequency ($\leq 10 - 50$ Hz) magnetic fields. In the case of AC fields [28, 72], the shielding effectiveness improves with increasing frequencies by the induced Eddy currents within the material. These currents are forced to the surface and produce a magnetic counter–field to the external cause. As a result the current density inside the material will drop. This effect is known as

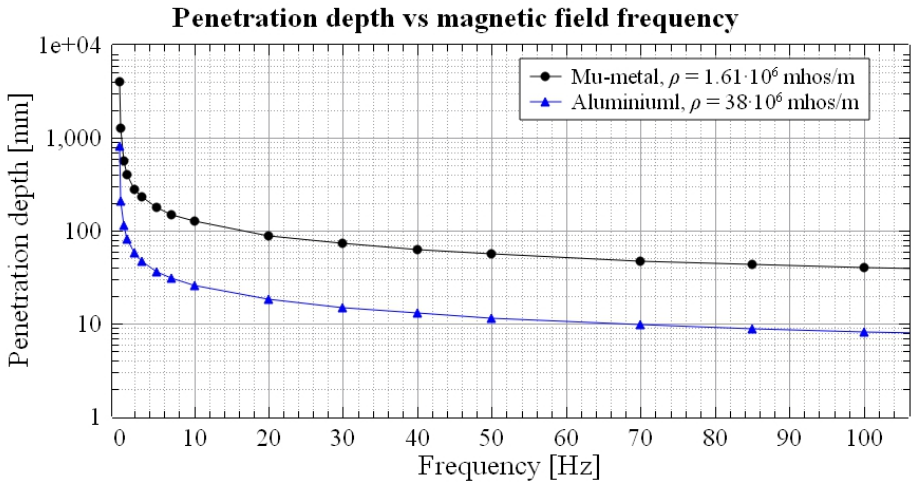

Figure 4.2: Comparison diagram of the penetration depth over the field frequency, for mu-metal and aluminium. At the low frequency regime, the required thickness of the shielding material increases rapidly, making its use impractical.

the *skin effect* and is related to the *penetration depth*, which is the depth where the current density falls off to e^{-1} of its value at the surface, given by

$$\lambda = \sqrt{\frac{\rho}{\mu\mu_0\pi f}} \,, \tag{4.15}$$

where ρ is the specific electrical resistance and f the field frequency. The effect becomes apparent for penetration depths equal to or smaller than half the wall thickness.

A common challenge in applications requiring magnetic shielding against a wide range of field frequencies [10, 20], are the very low frequency components of the order of a few Hz and especially for $< 1\,\text{Hz}$. This is because the effective penetration depth at these frequencies becomes much larger than the typical thickness of the shielding material. Therefore, the mechanism of the Eddy currents has practically no effect. Figure 4.2 shows a comparison of the variation of λ with respect to the field frequency for mu-metal and aluminium. Mu-metal has a lower electrical conductivity than aluminium, which translates to a thicker sheet of metal required for shielding against a field of the same frequency. For this reason, materials of a high electrical conductivity are preferred in AC shielding applications [20, 44, 50]. The above diagram shows that even in the case of aluminium, the skin-depth becomes larger than 400 mm over frequencies of $\leq 1\,\text{Hz}$. At the same time, the magnetic permeability of mu-metal drops rapidly as a function of the field frequency. This creates a "gray" zone at the very low frequency region, where both the AC and DC or ELF shielding mechanisms cannot provide optimal field attenuation.

4.1.2 Practical Challenges

Impact of Openings

In practice, there are many occasions where access is required inside the shield for laser light, wires, tubing etc. However, these openings will inevitably allow some of the magnetic flux to leak inside the housing and degrade the shielding efficiency [28, 98]. In the case of a finite cylinder with open ends the external magnetic field drops exponentially from the opening towards the centre as [128]

$$\mathrm{B_{in}} \approx \mathrm{B_0} e^{-\beta z / D_{\mathrm{op}}} \ , \tag{4.16}$$

where D_{op} is the diameter of the aperture, z is the distance and β a factor equal to 7.0 for a transverse and 4.5 for an axial external field. From (4.16) it can be shown that at a distance equal to one diameter ($z = D_{\mathrm{op}}$) the original field is decreased by a factor of 10^3 for a transverse and 10^2 for an axial field, respectively.

A formula that is used in this work (see fig. 2.15a, 4.6 and 4.8) and considers the contribution of the openings to the shielding factor of a cylindrical shell is [23]

$$\mathrm{S}_{j,\mathrm{eff}}(z) = \left(\frac{1}{3} e^{-k_j (z/(D/2))} + \frac{1}{3} e^{-k_j ((L-z)/(D/2))} + \frac{1}{\mathrm{S}_j} \right)^{-1}, \quad (j = \mathrm{t},\, \mathrm{a}) \tag{4.17}$$

where z is a point along the shield's longitudinal axis with its origin at the one end and k_j is the Bessel factor [72]. For a transverse external field $k_{\mathrm{t}} = 3.832$, while in the case of an axial field $k_{\mathrm{a}} = 2.405$. When apertures are necessary, a method used to suppress the field leakage effect is by incorporating a collar of the same material over the opening in the shielding shell. In practice, a collar of a length l and diameter d with an aspect ratio $l/d \approx 2 - 3$ is considered to make the above effect almost negligible. In addition, widening the air-gap between shells of a multi-layered shield is also recommended in these cases. The effect caused by much smaller openings such as holes and slits, can be treated theoretically by removing a magnetic dipole. In this case the field drop can be approximated as x^{-3}.

Joining Techniques

Another challenge which should be considered in applications is the technique used for mounting the shield onto the experimental setup or when assembling it in sections. Four different methods have been examined by S. Dickerson from M. A. Kasevich' s group at Stanford University [36] which include the use of fasteners, thermal interference fit, internal wrapping with highly permeable Metglas foil and welding followed

by annealing. The application of mechanical stresses, significant temperature variations and small holes or slits will degrade shielding performance. Consequently, torque application on fasteners or pressure on bracings can affect the shielding efficiency, even by a factor of 4. In the case of the thermal interference fit, two segments can slide together via a push fit joint under high temperature, producing a very tight fit after cool-down. This method performed about two times better compared to the previous practice, however both techniques create stresses in the shielding material. Application of Metglas windings (see §5.1) around the inner shielding shell outperformed the fasteners but increased the radial field inhomogeneity by a factor of 10 due to induced field gradients. Finally, the welding technique combined with a standard annealing process demonstrated the best results. Although initially the results were very close to the thermal interference fit, when followed by degaussing (see §4.1.3) the field inhomogeneity at the welded regions was minimised to almost negligible levels.

4.1.3 Magnetic Permeability and Optimization

The magnetic permeability of the shielding material plays a central role in shielding effectiveness. In contrast to paramagnetic and diamagnetic materials where the magnetic permeability is a linear function of the magnetising field, in ferromagnets it is characterized by a non-linear function [32]. A simplified model describing the ferromagnetic properties is illustrated in fig. 4.3a.

Examination of a ferromagnetic microstructure shows that the atoms, represented as magnetic dipoles, are organized in regions where the majority of the dipole moments has the same orientation, demonstrating what is referred to as *short-range order*. These regions are called *magnetic domains* and are characterized by a high internal magnetization. However, in the absence of external magnetic fields, the magnetization among these domains is completely random and cancels out, so that the material macroscopically behaves as if it has zero magnetization. Once an external field **H** is applied however, most of the magnetic dipoles will tend to align with the external cause. As a result, the domains with favoured orientations will grow in the expense of those domains with the less favoured orientations. If the field magnitude is high enough, the material will remain magnetized even if the magnetizing field vanishes (non-reversible region). Further increase in field amplitude will cause more dipoles to align with it, until the *saturation point*. At this point, the majority of the magnetic domains has the same orientation with the external field, and the material's magnetisation reaches a plateau. By decreasing the external field and then following the same process in the opposite orientation, one can derive the magnetization curve or *hysteresis loop* as shown in fig. 4.3b. The points where the curve intersects with the horizontal axis show the magnetising force required to magnetise the

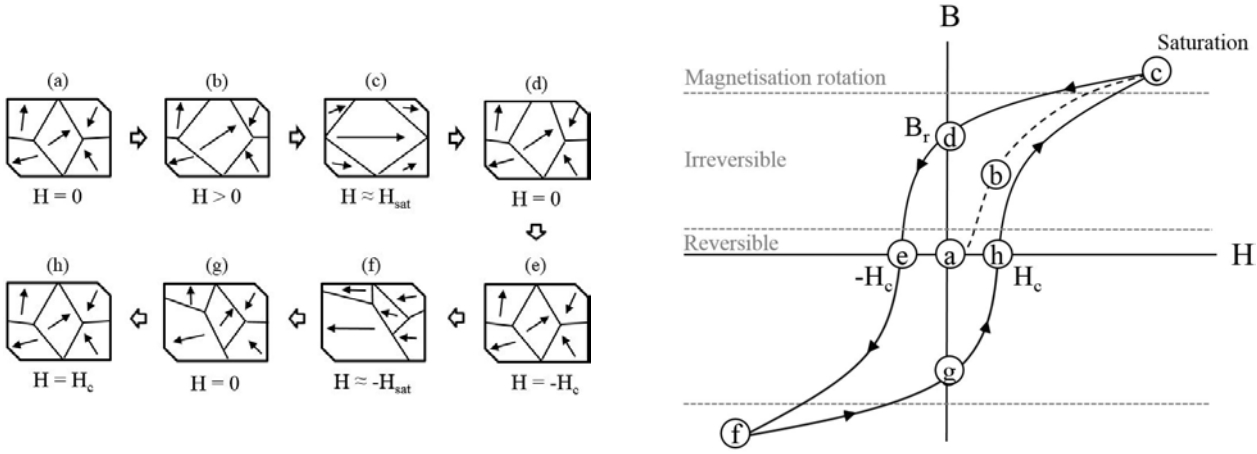

(a) Magnetic domains.

(b) Hysteresis curve.

Figure 4.3: (a) Representation of the magnetic domains in a ferromagnetic material under different magnetisation conditions. Favoured domains will expand under the presence of a magnetising field and will start rotating to almost perfect alignment at saturation. Once the magnetising field is vanished, a part of this magnetisation is stored in the material as remanence. (b) Example drawing of a hysteresis loop divided into three different regimes referring to magnetic domains' boundary motion (reversible, irreversible and magnetization rotation). Each labelled point on the hysteresis loop relates to the corresponding conditions in picture (a). The dashed curve represents the initial magnetisation curve (axes not in actual scale).

material, known as the *magnetic coercivity* H_c. Materials with a high H_c are called *hard magnetic materials* and are ideal for permanent magnets, whereas those with a low H_c are referred to as *soft magnetic materials* and are preferable for applications such as communication engineering, magnetic memory storage technology, and magnetic shielding. The points where the hysteresis curve intersects with the y-axis, corresponding to a zero external field, are called *remanent magnetization* M_r and indicate the permanent magnetization left to the material when the external cause has vanished. The magnetic permeability μ of the material is given by the slope along the hysteresis curve and is a function of the magnetising field $\mathbf{H}$. Starting from a certain minimum value, it increases until it reaches its maximum value close to saturation, and then drops rapidly. This is the reason why the magnetic flux can penetrate a magnetic shield easily when its material is saturated, degrading the shielding efficiency significantly. Also, a common characteristic to be taken into account for shielding applications is that materials demonstrating very high μ values tend to saturate relatively easily. For instance, annealed mu-metal can reach saturation at to the region of ~ 0.7 T [5].

Annealing

From the above discussion it is clear that the ease of motion of the magnetic domain boundaries plays a key role in the magnetic behaviour of the material. A change in magnetisation is restrained by internal

strains, as well as the presence of impurities within the crystal lattice. For this reason, a common treatment used in magnetic alloy engineering is *hydrogen annealing* [109]. The high heat releases internal stresses within the material's lattice and helps to remove impurities by breaking the interstitial bonds that they form with the lattice atoms. In addition, under these conditions and in the absence of external magnetic fields, the magnetic domains can randomise their orientations again to reduce the material's internal energy, and hence its net magnetization vanishes. However, in a real material remanence can be minimised but cannot become zero.

Degaussing

Although annealing is the most effective treatment, it is a high cost process and impractical to perform regularly. Another technique that is commonly used for shield optimisation is known as *degaussing* or *magnetic shaking* [11, 119, 122]. A slowly decaying external sinusoidal magnetic field produces internal magnetic torque on the material's atomic dipole moments, randomising their orientations. As a result, any residual magnetisation due to applied fields or stresses is reduced, while the effective permeability increases. In some cases, degaussing is used after annealing for further optimisation.

Typically, a special coil is wound around the shield housing and an AC current of approximately 50 - 60 Hz is applied. The initial amplitude of the produced magnetic field should be high enough to bring the material to complete saturation (five times the H_c is recommended). Then, by smoothly decreasing the demagnetising current to zero, the material goes through multiple cycles of the hysteresis loop with a gradually decreasing amplitude, until its remanent magnetization practically vanishes. Any ambient DC magnetic fields will have their impact to this process and will be stored in the material's memory. Hence, in real life applications it is more accurate to say that the practical result of degaussing is to bring the shielding enclosure to a magnetic equilibrium with its environment [11].

Since the shield performance is affected by its handling or storage history, degaussing is normally used after installation or certain periods of operation.

Mechanical Shaking

Similarly to degaussing, it is observed that introducing mechanical vibrations can also result in partial demagnetisation of a shielding shell. Since internal stresses or impurities might prevent domain wall motion, mechanical shaking can promote the randomisation of the domain orientations, decreasing the remanent magnetisation. Gentle tapping during degaussing is also said to improve results significantly [41]. Neverthe-

less, application of excessive stresses should be avoided as they can cause a magnetisation effect, commonly referred as *inverse magnetostriction* [68].

4.2 Numerical Treatment

Although there are many different definitions in the literature regarding the shielding efficiency, these are based on various approximations and apply only for basic geometries. Consequently, no accurate formula exists especially for more complex structures. A common tool used for studying and optimisation for this type of problems is numerical simulations based on the *finite element method* (FEM) [33, 57]. This method calculates approximate solutions to boundary value problems for partial differential equations on a certain geometry. The problem geometry is discretised by a mesh of small sub-domains, referred to as *finite elements*. Solving simple equations on these elements and then assembling the local solutions into a more complex equation system, allows to approximate a solution for the entire geometry.

Numerical simulations of this work were performed on COMSOL Multiphysics package [2], which shares many similarities with other familiar commercial software like ANSYS, Autodesk Simulation, DIANA etc. The procedure followed to build the models presented in this work is briefly described in the following subsection and could be useful to those interested in setting up similar simulations.

4.2.1 Model Definition

A single-shell cylindrical shield was modelled first to test the agreement between the simulation results and the analytical calculations. In most cases, a 2D model is sufficient for solving a simple magnetic shielding problem. However, in order to draw a better picture of the the magnetic field distribution around complex geometries like in these problems involving multiple apertures, asymmetries, additional magnetic field sources etc., then a 3D model is more suitable. The discussion that follows below goes through the steps for setting up a base model in 3D that covers most of the relevant problems; however, the same principles apply for the 2D case. In this example, the model geometry consists of a cylindrical shell encapsulated in a 3D box, representing the magnetic shield surrounded by a volume of air.

Since discretization is important for the convergence of any arithmetical method, the mesh quality of the CAD geometry ensures a more accurate result in FEM. This means that meshing needs to be optimised for each problem, by refining the element size and distribution within the geometry. Narrow regions or areas where rapid variations of the solved physical quantities occur, will require a finer mesh in order to be resolved.

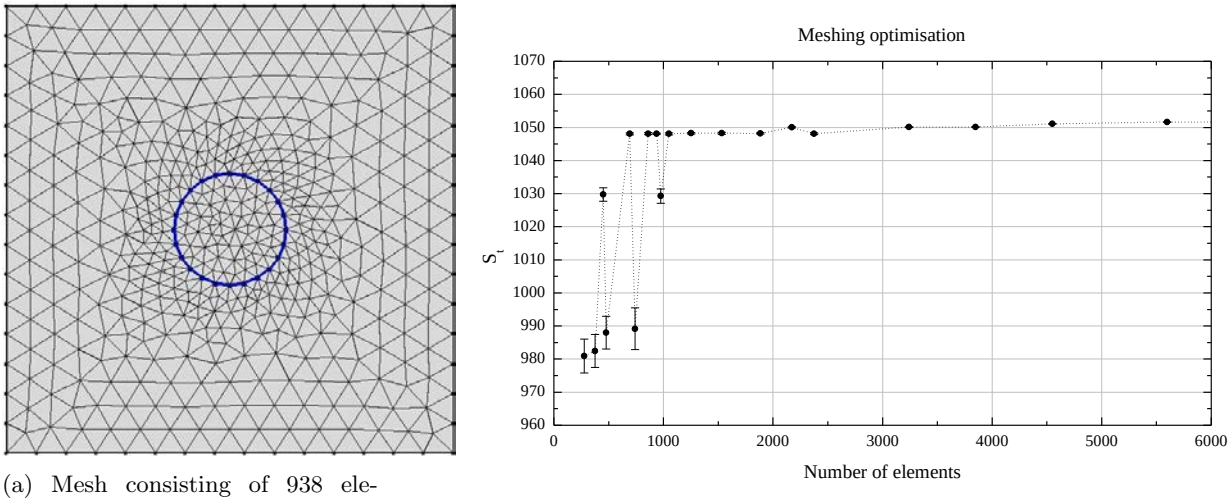

(a) Mesh consisting of 938 elements.

(b) Convergence plot.

Figure 4.4: Example of mesh optimisation process on a 2D model, where the shielding factor is derived by the average of the calculated values along a distance of 1/3 radius from the housing centre, in the magnetic field direction. (a) Mesh of a 2D model built during preliminary tests. The circle in the centre represents the shield cross-section. (b) Convergence plot of the simulated results as a function of the number of elements.

A common practice is to perform successive test simulations while refining the mesh, until results become independent of the element size. Figure 4.4 demonstrates this process by comparing the simulated results, while increasing the number of elements $\mathcal{N}$. Each data point represents the average S_t of about 10 values along 1/3 radius distance from the shield's centre. When the number of elements is still low (below 1000), the results indicate a relatively high deviation where the derived value is varying considerably. Beyond a certain number of elements however, the results become practically constant demonstrating a standard deviation of less than 1%. When the relative error drops below an acceptable value, it is up to the user's judgment on how much further optimization is satisfactory, considering that any increase in the number of elements has a cost in the memory requirements and solving time.

One of the challenges when simulating high aspect ratio geometries, like a long cylinder with very small wall thickness, is that a very fine mesh is required in order to resolve the narrow regions, resulting in a large number of elements. As a consequence, the memory requirements increase considerably and the solving time grows exponentially. In order to overcome this limitation, especially for more demanding cases such as multi-layered shields, the geometry symmetries were taken into advantage. Instead of solving for the whole structure, it is convenient to divide the geometry into symmetric sections by using planes of symmetry, as illustrated in fig. 4.5.

The physics equations for this model are defined by the *"Magnetic Fields, No Currents (mfnc)"* sub-

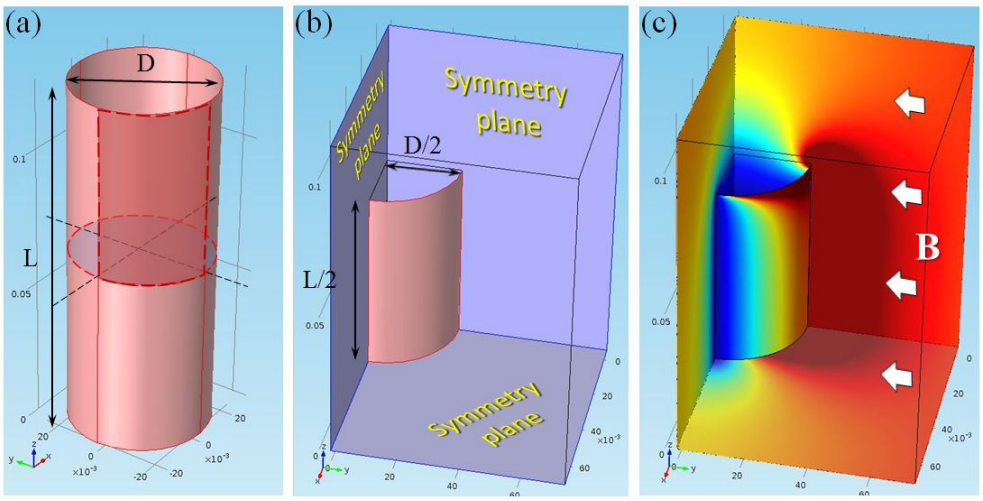

Figure 4.5: Simulated 3D geometry, sectioned into quarters by using planes of symmetry. This technique reduces the number of elements considerably and therefore minimizes the required computational resources and solving time.

module under the AC/DC module. No material magnetization $\mathbf{M}$ is considered in this analysis, so the model is only solving for the magnetic scalar potential V_{m}, corresponding to the perturbation field caused by the magnetic shield. This formulation is defined as *"Reduced Field"* and has the form

$$-\nabla \cdot (\mu_0 \nabla V_{\mathrm{m}} + \mathbf{B}_{\mathrm{ext}}) = 0, \tag{4.18}$$

where $\mathbf{B}_{\mathrm{ext}}$ is a uniform background field, representing the geomagnetic field. In the following simulations $\mathbf{B}_{\mathrm{ext}}$ is defined by a typical value of 50 µT.

One of the special features of the chosen sub-module is the *"Magnetic Shielding"* boundary condition which can be used to model the thin shielding sheet of metal in the form of a cylindrical 2D surface embedded in a 3D geometry. The purpose of this is to use a 2D mesh for the shielding structure instead of a 3D mesh. This way, the number of elements can be reduced considerably, since a thin cylindrical 3D wall would require a 3D mesh consisting of a larger number of elements. A 2D tangential projection of the 3D field equation is then solved on the shield's surface, where the permeability and thickness of the material are set as parameters in the settings.

The background magnetic field is applied via the *"External Magnetic Flux Density"* condition. In the case of a full geometry, this condition is assigned to all of the faces of the box that encloses the cylinder. However, when making use of the symmetry planes, certain boundary conditions need to be applied in order to meet the appropriate physical requirements. Symmetry planes tangential to $\mathbf{B}_{\mathrm{ext}}$ are assigned with the *"Magnetic*

Insulation" condition ($\mathbf{n}\cdot\mathbf{B}=0$), since the solution is exactly mirrored on them. The plane normal to $\mathbf{B}_{\text{ext}}$ is assigned with the *"Zero Magnetic Scalar Potential"* condition ($V_{\text{m}}=0$) to represent continuity of the solved field on the other side.

To verify the equivalence between a model (A) that simulates the full geometry with model (B) simulating a half-quarter section of the original geometry, two corresponding 3D models with identical parameters were built and compared. Figure 4.6 shows the comparison between the results of case (A) in black and case (B) in red colour, respectively. Each curve represents the shielding efficiency along the shield's longitudinal semi-axis, with the centre being at the origin. The derived results are very close with each other and seem to completely overlap at this plot scale. Therefore, the symmetry plane technique produces equivalent results with the full model and can be used for demanding simulations. In addition, the analytical prediction from (4.17) is plotted in the same graph, represented by the dashed curve. Comparison of the analytical shielding factor with the computed numerical values at the shield's centre showed a relative error of $\sim 8\%$. A potential reason for this difference could be that the analytical approximation does not consider any fringing effects at the shield's ends. However, these effects are expected to affect the distribution of the magnetic field at these regions, causing the values of the residual field to increase. As a result, the shielding factor values derived by the simulation will be lower.

A final trial was performed to test the accuracy of a model exploiting the *"Magnetic Shielding"* boundary condition that was described above. For this reason, a third 3D model (C) was built where the shield has exactly the same dimensions with the shield in model (A), with the only difference that the shielding wall is now represented by a 2D surface (shell) and the thickness is set as a parameter in the boundary condition settings. The computed results are plotted in the same graph with the previous iterations in fig. 4.6, represented by the turquoise curve. Again, the corresponding values are very similar with model (A), with a relative difference of less than 2% at the centre of the cylinder.

In conclusion, the investigated simulation techniques can be used for solving problems that involve more complex geometries, requiring a high number of elements. The number of elements used in the models of the above examples was $\mathcal{N}^{(\text{A})}\approx 1699802$, $\mathcal{N}^{(\text{B})}\approx 1470000$ and $\mathcal{N}^{(\text{C})}\approx 1730000$, respectively.

4.3 Results

As discussed in the previous chapters the GGtop sensor needs to be shielded at the interferometry section. For this reason, the traditional practice of introducing a commercial three-layered mu-metal shield was used. Before purchasing the shield, a series of simulations were performed by considering the geometrical

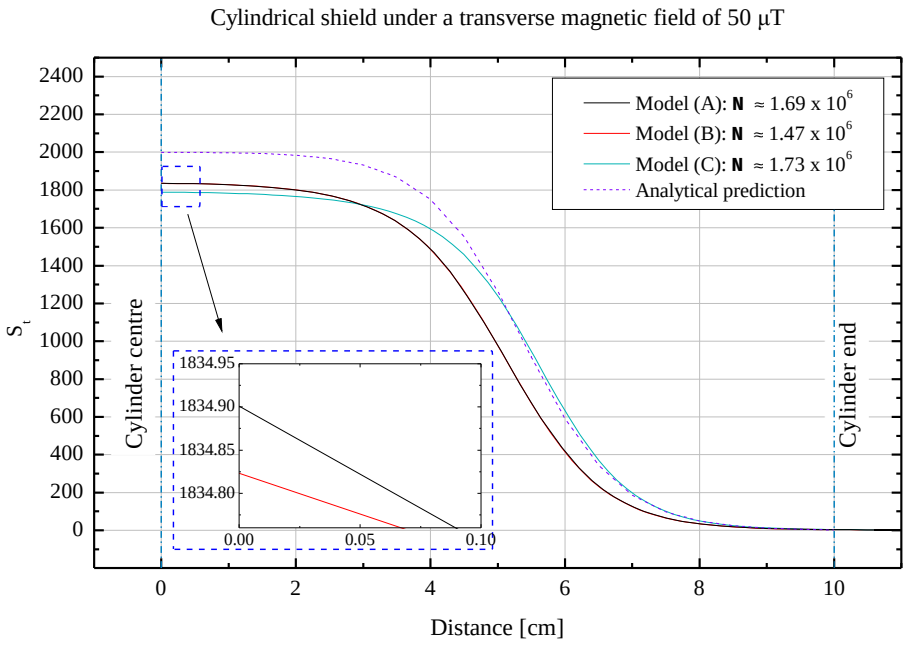

Figure 4.6: Validation tests on the full geometry model (A), half-quarter geometry model (B) and a model without the use of the *"Magnetic Shielding"* boundary condition (C). Each curve represents the shielding factor along the shield's longitudinal semi-axis, with the dashed curve indicating the analytical prediction for comparison. The simulated geometry consists of a cylinder with dimensions of $l = 20$ cm, $D = 5$ cm, $t = 2$ mm and $\mu_r = 50000$, under a transverse field of 50 μT.

characteristics of interferometry tube, as shown in fig. 3.9. Three nested cylinders were simulated by varying the wall thickness and shell separation, but keeping the inner shell dimensions constant to $l_1 = 66$ cm and $ID = 15$ cm. The model geometry exploits symmetry planes, as described in the above discussion. A typical value of $\mu_r = 50000$ was used for the mu-metal, while the external field was defined in the transverse direction with a constant magnitude of 50 μT.

Figure 4.7 (left) shows the simulated transverse shielding factor (circular data points) at the centre of the shield for different shell separations, in the range of 1 - 5 cm and a constant wall thickness of $t = 1$ mm. The corresponding analytical values derived from (4.13) are plotted in the same graph, represented by the square data points. The comparison of the absolute values between the two curves shows that both results are of the same order of magnitude, with the analytical values being higher than the corresponding numerical data by almost a factor of 2. In addition, the numerical values seem to have a very small variation over layer separations between 5 - 10 mm, and they drop rapidly for layer separations of $\lesssim 5$ mm. This is expected, since the multi-shielding effect will be suppressed as the air gap approaches zero. However, this trend is not resolved in the analytical approximations. A discussion on the sources of these discrepancies is presented at the end of this section. Finally, a separation of 10 mm was chosen for the purchased shield. The reason for

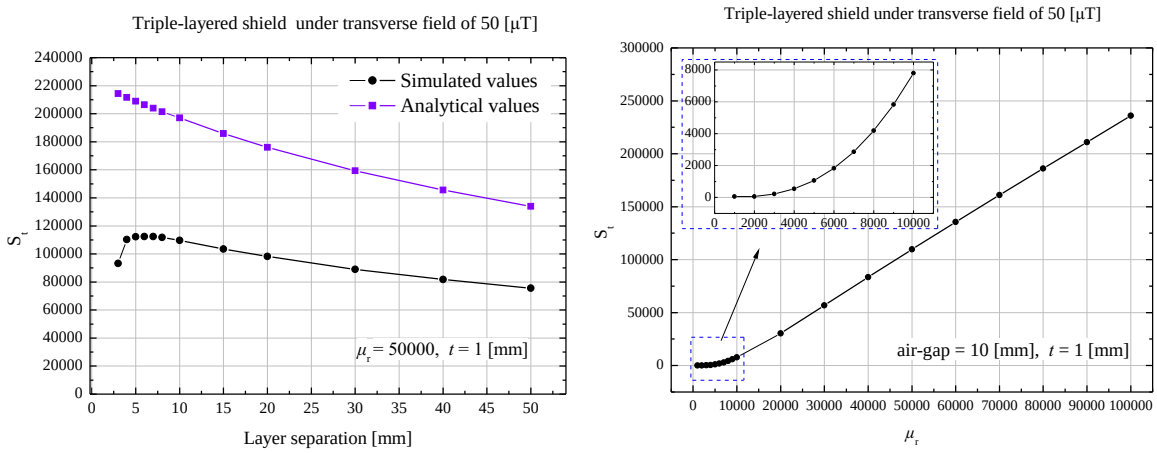

Figure 4.7: Parametric simulations of the shielding efficiency at the centre of the shield as a function of different shell separation (left) and permeability values (right), respectively. A transverse field of 50 μT is considered in both cases.

this choice is because an increase in the spacing between the layers tends to reduce the effect of the openings, by limiting the field fringing effects in the regions closer to the shield's ends. This has a positive effect on the residual field profile along the shield's axis, because it increases the extent of the region where the field attenuation reaches its maximum values. In addition, this layer separation would make shield assembly easier during its integration with the interferometer.

A second series of parametric simulations were performed, this time by varying the permeability value, starting from 10^3 to 10^4 by an increment of 10^3, and then from 10^4 to 10^5 by an increment of 10^4. The shielding factor values below $\mu_r \approx 10^4$ demonstrate a second power low growth, which becomes linear for higher permeability values.

Lastly, the impact of the material thickness was examined in the range of 0.5 - 2.5 mm, by an increment of 0.25 mm, while the air gap was kept at a constant value of 10 mm. The derived results are shown in fig. 4.8 along with the corresponding analytical values. The latter were calculated by using the expressions for the finite multi-layered shield (4.13), (4.14) and (4.17). The aspect ratio values of the nested layers here correspond to $L_i/D_i \approx 3.5 - 4.7$, which yield the same shielding factor values when computed individually by both (4.7) and (4.17), with a relative difference of $< 1\%$. The total shield weight m_{tot} that corresponds to each case is indicated in the top horizontal axis. Observation of the analytical and corresponding numerical values shows deviations of an order of magnitude or higher, for both the transverse and axial factors. In addition, this divergence demonstrates an increasing trend as the wall thickness increases. A potential reason for this is that although the theory predicts that the $S_{t/s}$ will increase linearly as a function of the wall

thickness, the total mass of the material will also increase. As the mass of the material rises, the shield will "attract" a larger amount of magnetic field flux from its environment, due to the hight permeability of mu-metal. Therefore, the rate of increase of the shielding factor will drop for higher layer thickness values. This can explain the trend of the data points in the plot, which the simplified analytical approximations cannot resolve very accurately.

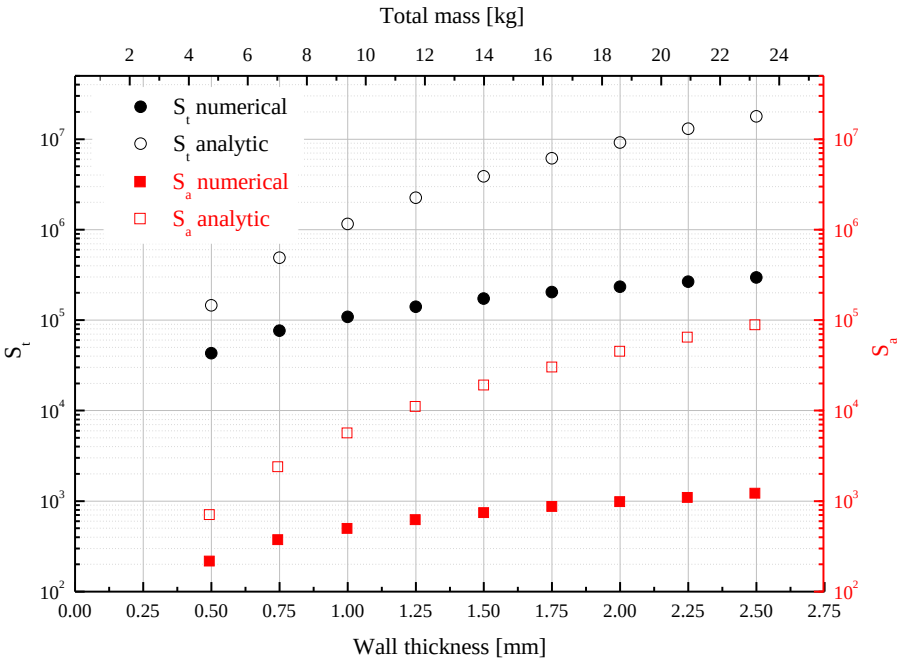

Figure 4.8: Parametric simulations of the shielding efficiency for different layer wall thickness. The corresponding shielding factor values for a transverse and axial field of 50 µT are indicated on the left and right vertical axes, respectively. The top horizontal axis shows the shield's total mass as the wall thickness increases.

Some common factors that could be responsible for the observed discrepancies between the simulated and analytical results in all of the above studies are discussed below. Firstly, although the analytical expression considers the field decay at the shield's ends, it does not account for any field fringing effects. However, these effects are expected to affect the calculated values of the residual field. In the example of the single cylinder shown in fig. 4.6, the relative difference between the numerical and analytical results was $\sim 8\%$. Although this is within the typically "acceptable" margin of error, when the calculated $S_{t,i}$ values for the individual layers are combined in the formula for the $S_{t,tot}$, these errors propagate (see (4.13)). By taking into account that the shielding factors of the individual nested layers act multiplicatively, it can be deduced that even small errors can cause significant deviations in the derived results.

Another observation is that the derived values indicate very high shielding efficiencies, which seem to

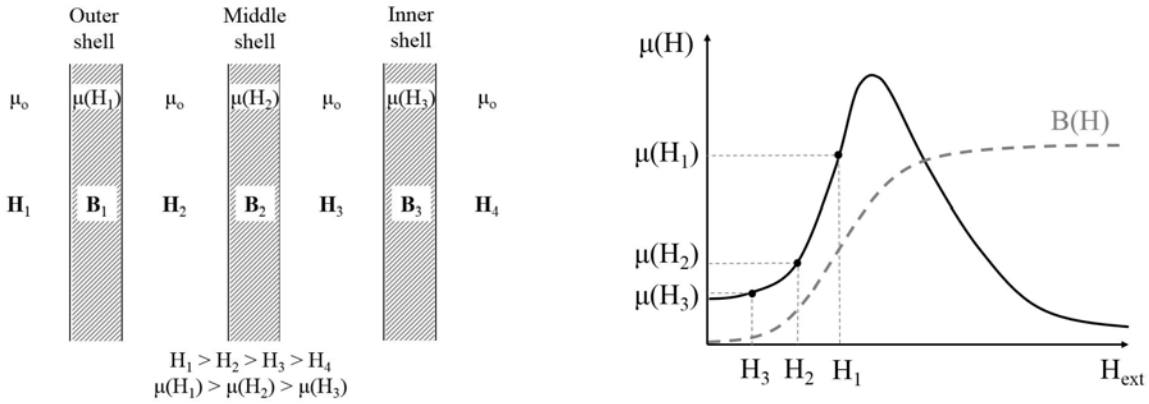

(a) Successive shielding layers.

(b) Non-linear permeability curve.

Figure 4.9: (a) Schematic representation of successive magnetic field attenuation through a triple layered shield. Each layer experiences a different external field of a decreasing amplitude towards the centre. (b) Since the material permeability varies as a function of the local field, its value will be different for each shell and will drop accordingly. This will yield a lower total shielding efficiency compared to what most simplified theoretical models suggest, which consider a constant μ instead.

be unrealistic when compared with real shields. One of the main reasons is that the relative permeability of a real ferromagnet is a non-linear function of the magnetising field. Therefore, a good knowledge of the material's B(H) curve would offer a more realistic approach, especially at very low field conditions. Figure 4.9 illustrates a qualitative example of how the relative permeability varies among the different shells of a triple-layered shield in practice. Even for each individual shielding layer, there are certain regions where the magnetic flux contained within the material takes higher or lower values. An example of this can be seen in fig. 4.5c. This produces zones of different relative permeability across the shield, which will have different contributions to the shielding factor. However, such effects are ignored in the analytical formulae, causing the calculated results to deviate. In addition, no remanence is considered in the above models, resulting in more optimistic predictions for the shielding effectiveness. This becomes more apparent in multi-layered shields, where the residual field becomes very low. For instance, residual flux densities below the level of $\sim 30\,\mathrm{nT}$ are difficult to reach in real shields, without the aid of degaussing. This is true even for shields incorporating three layers, where the theoretically predicted field values are typically at least an order of magnitude lower. This has been verified through observations on different shields that are used in other experiments within the same group. Ultimately, a wall thickness of 1 mm was chosen for each individual shell of the purchased shield, which provides sufficient structural integrity while keeping the total weight below 10 kg.

A final example highlighting the benefits of using FEM simulations as a study tool is given below. The key advantage here is that the model can provide information about the variation of the physical quantities

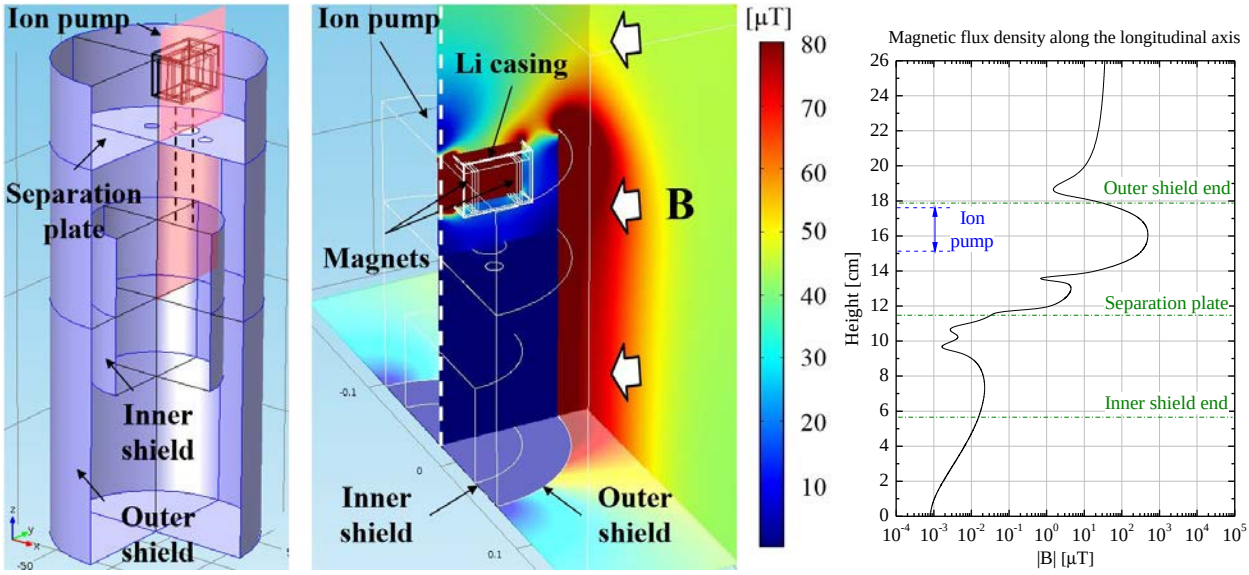

Figure 4.10: Right: Simulated geometry of a dual-layered shielding housing encompassing a hypothetical compact vacuum chamber, not shown in the schematic. The model features an ion-pump mounted at the top of the chamber with an offset from its centre. A circular plate including three feedthroughs is separating the ion-pump from the main chamber. Centre: Simulated results shown on the one quarter of the geometry. The colour map illustrates the distribution of the magnetic flux density magnitude in space. The white dash-line indicates the longitudinal semi-axis. Left: Plot of the magnetic field flux density norm along the shield's longitudinal semi-axis.

in space and resolve local effects. Figure 4.10 shows an example of a case study for a compact chamber of a cold atoms experiment which needs to be shielded. However, the influence of the magnetic field produced by the magnets of an ion-pump close to it could cause issues. By experimenting with several parameters in the design, it is possible to predict the field's behaviour and establish certain design principles to overcome potential issues. In addition, useful information can be extracted with regards to the impact of access openings required for laser light, wiring or tubing.

4.4 Shielding the GGtop Interferometer

A triple-layered mu-metal shield was chosen for the GGtop (see fig. 4.11), in order to provide the required shielding efficiency of the order of 10^3. Each shell has a wall thickness of $t = 1$ mm, with dimensions $l_1 = 66$ cm, $ID_1 = 15$ cm for the inner shell, $l_2 = 67$ cm, $OD_2 = 17$ cm for the middle shell and $l_3 = 68$ cm, $OD_3 = 19$ cm for the outer shell, respectively.

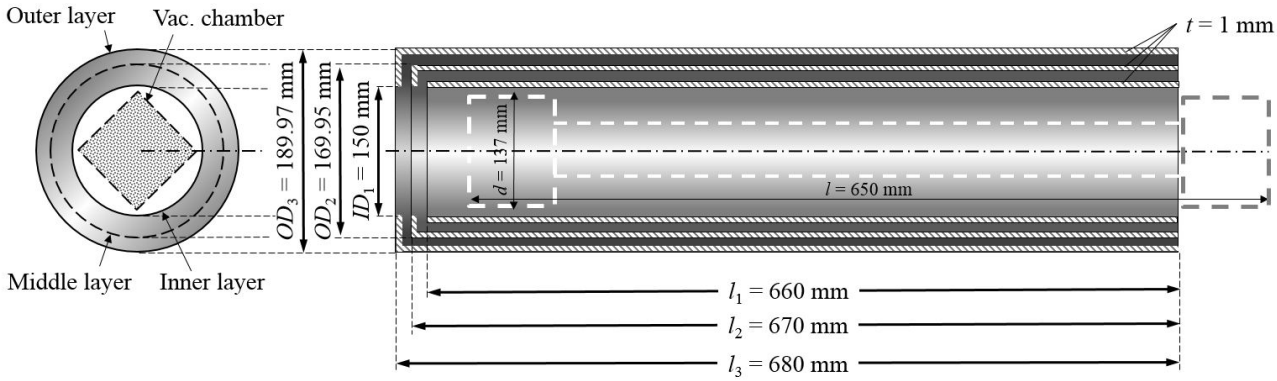

Figure 4.11: Schematic of the triple layered GGtop magnetic shield (drawing not in scale). The interferometry tube is indicated with dashed lines at the centre.

4.4.1 Calculations

The final shield design was simulated on COMSOL before the shield was purchased, in order to make an initial estimate of the expected performance. As discussed previously, each layer will experience a successively lower magnetic field towards the shield's interior and will behave differently. Since no detailed data of the low field B(H) curve was available, an "effective" permeability value was used for the three layers as a running parameter, within the range of $\mu_{\mathrm{r}}^{(\mathrm{eff})} = 10^4 - 10^5$. The derived attenuation factors along the shield's longitudinal axis are shown in fig. 4.12 for a transverse and axial external field of 50 µT, respectively. The derived results seem very optimistic when compared with experimental data, where a shielding factor of 10^3 for a typical permeability value of approximately 40,000 is a challenge. The main reason for this is because no material remanence is considered in the above calculations. A good knowledge of the material's behaviour at low fields is a requirement in order to make relevant implementations in the model.

4.4.2 Experimental Results

The GGtop shield was purchased from the MuShield company and was installed in the sensor directly after delivery, without any bench top testing due to tight timeliness with the project. However, there was a concern for mu-metal being magnetised over the time, mainly by the MOT coils and the internal bias coil around the interferometry tube. Eventually, the magnetic tests were performed two months later and are described below.

Due to the relatively large shield size, the measurements were taken under the ambient field, with the assembly standing on the floor inside the lab environment. The sensor used for all of the magnetic tests in this work was the uniaxial Stefan–Mayer Fluxmaster magnetometer. The magnetic field profile was acquired

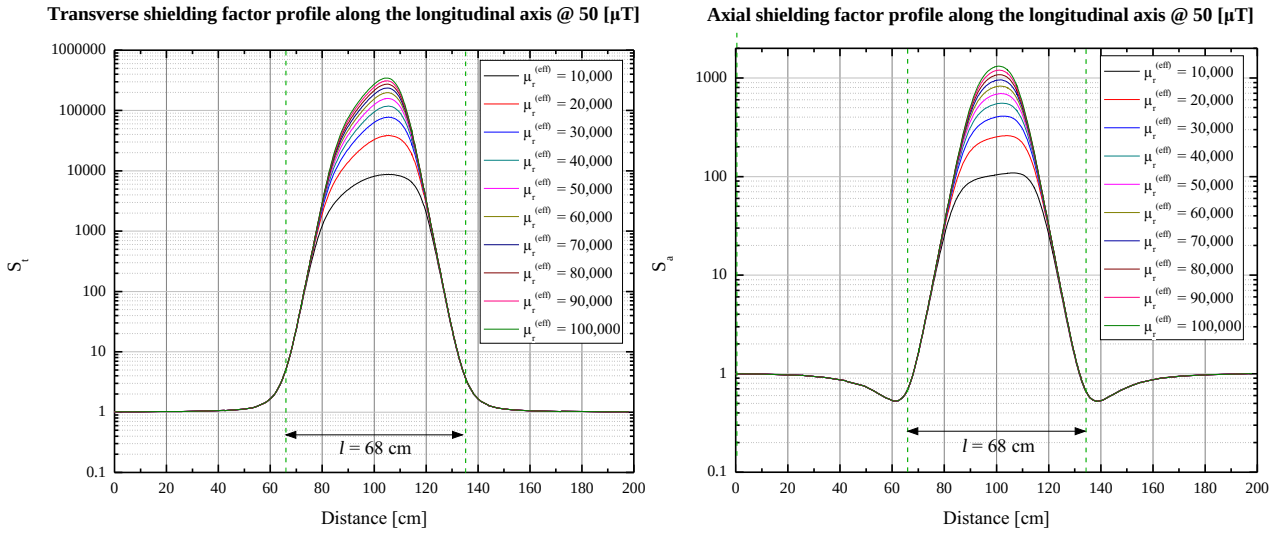

(a) Transverse shielding factor.

(b) Axial shielding factor.

Figure 4.12: Parametric simulations on the concept design for the triple layered GGtop shield. Graphs show the shielding factor profile along the shield's longitudinal axis under a transverse (left) and axial (right) magnetic field of 50 μT, respectively. Since each shielding layer experiences a different magnetising field, an effective relative permeability value was used as a running parameter.

by sliding the sensor along the shield's longitudinal axis with the aid of a meter stick, suspended on an aluminium frame. In order to derive the horizontal field component, two measurements were taken at each point, with the sensor pointing in the NE and then in the SE direction. Finally, the vertical component was acquired to derive the total field amplitude along the cylinder's axis. The derived shielding factor is presented in fig. 4.13 (left), where each data set corresponds to measurements taken by adding the shielding layers in the assembly one by one.

A noticeable feature on the two last data sets is the sudden inversion of the derived curve at the central region. This is owed to the zero crossing of the vertical field component, as shown in fig. 4.13 (right). The most probable cause of this effect is accumulated material remanence that becomes apparent at very low residual field levels, when two or three layers are assembled. Depending on its amplitude and orientation it may cause zero crossings, as in this case. A way to come around this issue is to repeat the measurements for each point by flipping the shield's ends. Then, by adding the corresponding values together, components owed to the shield's remanence will drop out (see also appx. B). The fact that the zero crossing was owed to the vertical field component, could be an indication of magnetisation caused by the solenoid around the tube. Handling during postage and mounting can also cause remanence. A common practice followed for optimising the shield in these cases is degaussing. At this stage, the interferometric measurements had to be resumed due to time limitations related to the progress of the GGtop project. Consequently, the shield was

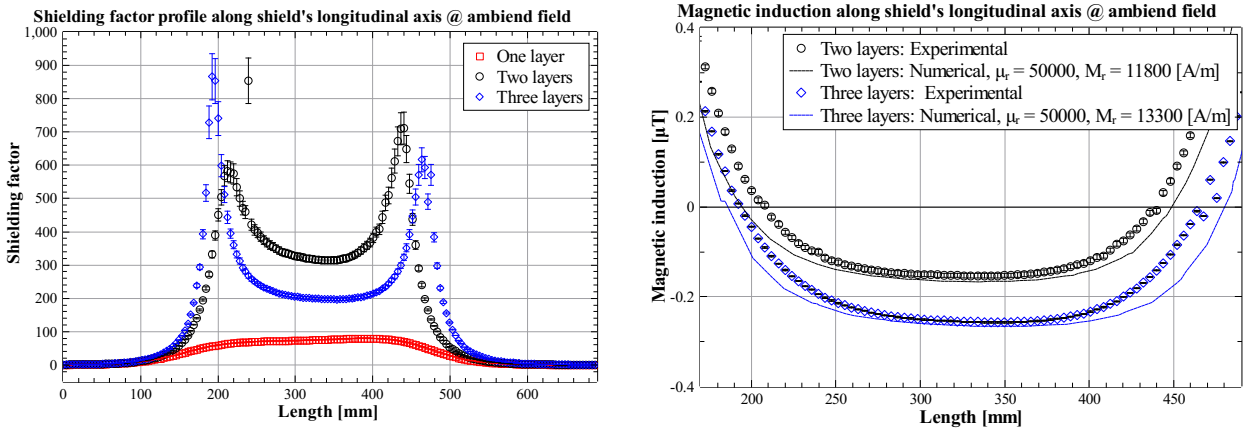

Figure 4.13: (Left) Shielding factor profile along the shield axis under ambient magnetic field. The number of layers is increased by one for each data set. The inversion effect at the central region is owed to the zero crossing of the measured vertical field component. (Right) Magnetic field magnitude profile along the shield axis under ambient magnetic field. The zero crossing for the dual and triple layer assembly can be explained by a potential material remanence effect, which can produce a remanent net magnetic field $\mathbf{B}_\mathrm{r}$. Depending on its magnitude and orientation it can cause a zero crossing like the one observed. Dashed curves represent simulation results that approximate the measured values, by assigning remanence values M_r to the material.

reinstalled in the system and further measurements had to be postponed for a later time in the future.

Finally, an effort was made to approximate potential remanence effects according to the above observations, by adding a remanent magnetisation $\mathbf{M}_\mathrm{r}$ in the material properties of the simulated model.The constitutive relation in this case becomes $\mathbf{B} = \mu_0\mu_\mathrm{r}\mathbf{H} + \mathbf{B}_\mathrm{r}$, with $\mu_\mathrm{r} = 50000$ while $\mathbf{M}_\mathrm{r} = \mathbf{B}_\mathrm{r}/\mu_0$. The case of 2 layers was approximated by using a remanent magnetisation value of $\mathrm{M}_\mathrm{r} = 11800$ A/m, while the 3 layer case with $\mathrm{M}_\mathrm{r} = 13300$ A/m, indicated with the dashed curves in 4.13 (right). This magnetisation corresponds to a remanent magnetic induction B_r of the order of ~ 10 mT. This magnitude is comparable to typical magnetic induction values inside the shield's material without remanence. However, the above values should only be considered as "effective" values, since the distribution of $\mathbf{M}_\mathrm{r}$ inside the material or the layers of the real shield is not expected to be uniform and further investigation is required to define it.

4.5 Conclusions

The material of the current chapter is divided in two parts. In the first part a theoretical overview on magnetic shielding problems was given, by presenting the fundamental formulation, along with some complementary information on certain practical aspects. Then, a numerical approach was discussed by using finite element analysis, along with certain techniques that can optimise accuracy and solving time.

The established models were used for the design of the GGtop shield and were then compared with the experimental data in the second part of the chapter.

Although the available analytical formulas throughout the literature can provide a relatively good approximation for most of the simple geometries, they are based on various assumptions like infinite length, certain aspect ratios, etc. As a consequence, when the shield's geometry deviates from these considerations, formulas do not work very well and in some cases they might even be in a poor agreement with each other. The initial purpose of the presented numerical models was to derive an order of magnitude approximation of the expected performance of a shield. However, a numerical analysis like FEM can be a very useful tool for studying more complex problems, that involve features like multiple apertures, different external field sources, joints, material remanence, etc.

Initially, a brief example of the mesh optimisation process was presented, along with three test models to validate the symmetry planes technique and the *"Magnetic Shielding"* boundary condition, respectively. The results from both methods were in a good agreement with each other, as well as with the analytical prediction and therefore these can be used accordingly in demanding simulations. In the next step, a series of parametric simulations were performed on the final 3D model to assist with the GGtop triple-layered shield design. The derived results indicated that the field attenuation factor gradually degreases as the air-gap among the layers becomes larger. Therefore, adopting a small air-gap of $\lesssim 2\,\mathrm{cm}$ can provide a relatively high shielding factor by keeping the overall size at a minimum. The trials with varying wall thickness showed that the shielding efficiency improves for a thicker material, as expected, but with a cost in the total weight. Consequently, the approach of using multiple nested thin layers is more efficient than a combination of fewer and thicker layers. Both numerical and analytical calculations indicated efficiencies of orders of magnitude higher than the requirements, however these needed to be verified experimentally. It was observed that in most cases, the derived values of the shielding factor for the triple-layered shield were an order of magnitude lower than the corresponding analytical predictions. A possible reason for this is that the numerical model calculates the distribution of the magnetic field around the shield and can capture features like the end effects at the shield's openings. The common analytical formulas do not consider these effects, however these can affect the residual field inside the housing. The impact of such inaccuracies in the results of a single shell might be relatively small. However, these effects become more significant in problems involving multiple layers. Finally, a case study on a more complicated geometry of a compact quantum sensor was presented, in order to demonstrate the benefits of using the finite element method for capturing and visualising local effects.

The second part of this chapter is associated with the experimental approach for shielding the GGtop

interferometer. A shielding factor of at least 1000 is required for the sensor in order to allow for gravity measurements of human size targets, typically of the order of $\sim 10^{-9}g$. A triple-layered shield was purchased according to the theoretical concept and went through an initial cycle of magnetic tests to evaluate its field attenuation performance. All layers have a wall thickness of 1 mm, while their dimensions are $l_1 = 660$ mm, $ID_1 = 150$ mm for the inner shell, $l_2 = 670$ mm, $ID_2 = 168$ mm for the middle shell and $l_3 = 680$ mm, $ID_3 = 188$ mm for the outer shell, respectively. The testing process started by measuring the residual magnetic field inside the inner layer and was then repeated by adding the remaining layers successively. The derived results indicated that the shield had developed magnetic remanence during its use on the interferometer, along the longitudinal axis. This had a negative impact on the field attenuation performance, yielding shielding factor values of ~ 200 across the central section of the shield. The main reasons for this are the magnetic fields produced in a close proximity to the shield by the MOT and the interferometry tube coils. Also, handling during shipping and the installation process can potentially induce mechanical stresses on the shielding material that degrade its magnetic permeability and produce magnetisation. Apparently, time constrains related to the progress of the GGtop project did not allow for further tests at this point and the shield had to be reinstalled in the system, in order to resume the trials on interferometric signal acquisition. The remanent magnetisation was determined with the aid of numerical simulations, where different values of M_r were assigned to the shielding material properties, in order to replicate the experimental observations. The best fit to the experimental data was achieved by $M_r = 13\,300$ A/m. However, it should be noted that this is an "effective" value which was used for all of the layers. The distribution of the magnetisation in the real shield is not expected to be uniform, as certain sections are closer to the coils and have experienced different mechanical stresses due to handling before and during the installation.

The outcome of the work undertaken on the numerical simulations and the GGtop shield characterisation have indicated areas for future work. Some further implementations on the work related to the numerical simulations could be the following. Using a reliable B(H) curve instead of a constant permeability value would provide a more realistic approach to the problem, especially for a multi-layered shielding structure. This is because each layer experiences a different magnetic field magnitude, which decreases from the outside to the inside of the structure. Since the magnetic permeability depends on the local field, its value will vary for each shell accordingly, yielding a lower total shielding factor than the one predicted by the simplified linear model. Also, real materials tend to store some remanent magnetisation which also affects the shielding performance. Statistical knowledge of typical remanence values would allow for implementing these effects in the simulated models, providing more representative results for real life applications. Finally, a relation of

the permeability dependence on tensile stresses or temperature variations could be implemented for studying various mounting configurations and the impact of the environmental conditions on the shielding performance during a field survey.

Regarding the experimental section, further tests can be conducted on the the magnetic characterization of the GGtop shield. A way to determine the shield's remanence is by flipping its ends and repeating the measurements. Then, the remanence can be extracted by the sum of the two field values measured at each point, divided by two (see appx. B). Although the system is currently operating inside a controlled lab environment, poor shielding performance during a survey is expected to have a significant impact on the gravitational measurements. A common approach to the above issues is degaussing, which can potentially bring the material to optimum performance, unless significant mechanical stresses have been induced on the structure, like in the case of a shock due to an accidental impact. In the latter case, annealing is recommended that can release the stresses and restore the material's magnetic properties. In addition, designing a degaussing system that allows for easy application would be very beneficial, as the system is expected to develop remanence more easily when operating in the field, requiring this treatment more frequently.

The shielding method presented here is the traditional approach used on quantum sensors. As quantum technology is currently moving towards miniaturization, portable sensors could benefit from certain trends of other shielding materials and techniques that can offer more flexibility in design complexity and weight reduction. The focus of the next chapter is the investigation of such alternative methods by using Metglas foil and 3D printing of permalloy metal powder.

CHAPTER 5

EXPLORING ALTERNATIVE MAGNETIC SHIELDING TECHNIQUES

One of the main objectives of this work was to explore alternative materials with the potential of achieving shielding efficiencies similar to mu-metal but without its disadvantages. Although mu-metal shields are used widely, they are characterised by a relatively high weight and the inflexibility to adapt to small and complex geometries, due to manufacturing limitations. The next sections are dedicated to two alternative shielding techniques that were explored during the work on this thesis. The first is the use of highly permeable Metglas foil to form lightweight shielding housings, while the second method exploits a 3D-printing process of permalloy powder for producing solid shielding structures. The latter project was performed in collaboration with the department of Metallurgy & Materials of the University of Birmingham, under the Quantum Hub partnership aiming towards the development of miniaturised quantum sensors.

5.1 Lightweight Metglas Shielding Structures

One of the main restrictions on the design of a mobile quantum sensor is its weight. A lighter material with the ability to provide a shielding efficiency similar to mu-metal would be particularly beneficial. In that view, Metglas 2705M foil was tested as a potentially alternative material. Metglas is a cobalt-based material with a relative permeability of $\mu_r = 600000$ (annealed), according to manufacturer's data sheet [6]. It is produced in the form of thin foil ribbons of 22 µm thickness and 5 cm width. Although its density of 7.8 gr/cm^3 is similar to mu-metal (~ 8.7 gr/cm^3), its higher permeability would require less material to achieve a similar field attenuation for a given geometry. Should this technique prove to be effective, it will provide sufficient shielding performance but with reduced added weight on the sensor and at a lower cost. In addition,

due to its flexibility Metglas can potentially adapt to relatively complex surfaces.

5.1.1 Experimental Results

As stated at the beginning of this section, Metglas is applied in the form of ribbons wound around the shield structure. In the following tests, a plastic cylinder with a length of $l = 500\,\text{mm}$ and outer diameter of $OD = 110\,\text{mm}$ was used to provide support to the foil windings. Similar experiments through the literature [75, 85] have shown that variations on the winding orientation of the Metglas foil around a housing result in a different shielding behaviour (see fig. 5.1). This can be explained by the magnetic leakage and fringing effects caused by the slits among the foil strips. When the magnetic field flux that flows inside the highly permeable metal ($\mu_\text{r} \sim 10^6$) meets a slit, it suddenly reaches a region of air where $\mu_\text{air} \approx 1$. This spatial discontinuity in the magnetic permeability causes a part of the magnetic flux to leak through the shield's surface, creating magnetic flux fringes. As a result, the flux density inside the material is reduced and the shielding factor of the housing degrades. The impact of this effect is stronger when the flow of the field flux is perpendicular to the slit and becomes less significant for a tangential field. As a consequence, the circular and helical windings are more effective under a transverse external magnetic field, whereas the longitudinal windings work best under axial fields. Comparison from preliminary tests between circular and helical windings indicated that the first perform slightly better under transverse fields with the latter having a small benefit under axial fields. Taking this into consideration, it was decided to use a combination of successive helical and axial windings in the effort to achieve as uniform coverage as possible. Care was taken so that successive winding layers of the same kind have an off-set of a half ribbon-width. In addition, opposite helicity was used between successive helical layers. The adjacent ribbons of the same winding were overlapped for about 1 cm and stuck together with tape along the seam-line, in order to achieve a better coupling and reduce local field gradients formed by pronounced edges.

The experimental setup used for all of the following magnetic shielding measurements is shown in fig. 5.2. It consists of three pairs of square coils that can produce the desired magnetising field, in the three axes. The specimen to be tested is based on an aluminium rail of 1,5 m length, allowing it to slide through the central axis of the coils. The magnetic sensor used in the previous chapter, was suspended on a wooden meter-stick and kept fixed at the centre of the coil system. The magnetising field is controlled by a programmable four-channel power supply (Rohde & Schwarz HMP4040) connected to the coils. Initially, a compensating field is produced by the coils in order to reduce the ambient field within the coil region as much as possible. Then, the desired bias is applied to the specimen for acquiring the residual field under different external field

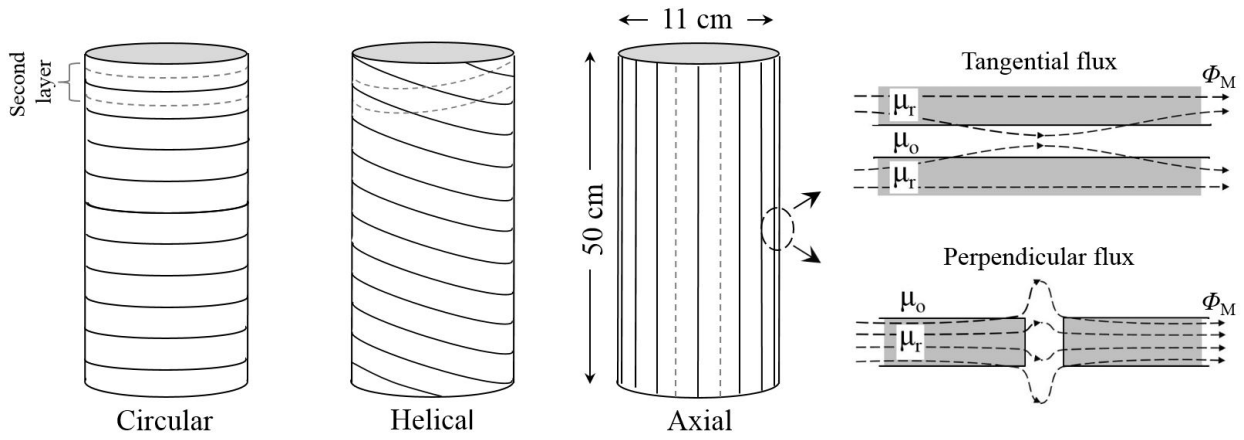

Figure 5.1: Metglas foil in circular, helical and axial winding orientations, respectively. Each configuration results in a different shielding behaviour. When the magnetic field flux is perpendicular to a slit between two strips, a part of it will leak outside the material causing the shielding efficiency to degrade. In the case where the magnetic field is tangential to the slit, the above effect has a smaller impact. As a result, the circular and helical windings perform best under a transverse external field, while the axial windings work best under a longitudinal field. An off-set between successive windings can reduce the field inhomogeneities caused by the material discontinuities.

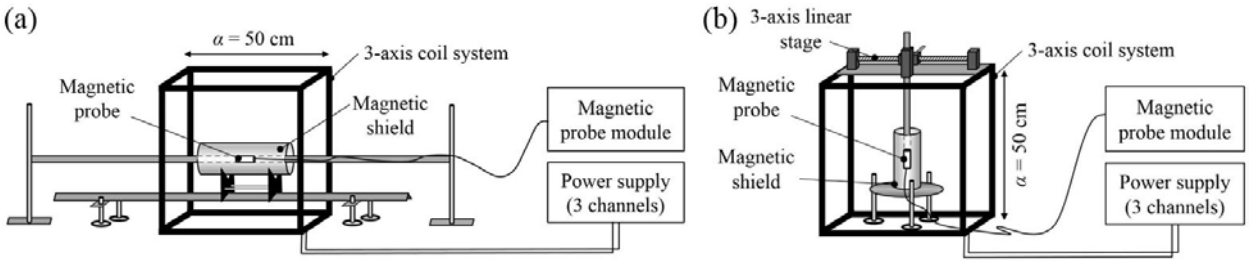

Figure 5.2: (a) Schematic representation of the experimental setup used for magnetic shielding measurements. The apparatus comprises of a 3-axis coil system, magnetic probe and a special base with rail that allows for easy movement of the shield along the central axis of the coil system. (b) Alternative setup configuration for measuring smaller shields. The sensor is suspended from a 3-axis linear stage, mount on a plate that rests on top of the coil system.

amplitudes. Successive measurements can be taken at different points along the shield axis, by sliding the base on the rail to acquire the residual field profile. The shielding factor (4.5) along the shield axis can then be derived by dividing the external field amplitude by the measured values. However, a real shield might have small inhomogeneities as well as magnetised regions due to handling and structural imperfections. For this reason, two values were measured at each point by inverting the field bias, for both field orientations, at the same amplitude. Since the measured field $B_{meas.} = B_{res.} + B_r$, the results were corrected by $B_{corr.} = (B^{+}_{meas.} - B^{-}_{meas.})/2$, where $B_{res.}$ the residual from the attenuated external field and B_r the field owed to remanence, while the superscripts (+/-) indicate the bias field polarisation. More details on this technique can be seen in appx. B.

The first cycle of measurements was performed on a single cylinder with the interest of studying the impact of the number of windings on the field attenuation. Figure 5.3 shows a comparison of the shielding factor profile along the cylinder axis for different number of wrappings under the same field, respectively. The results showed that the increase in Metglas layers clearly improves the shielding efficiency. The increased fluctuations at the highest values are owed to the fact that these data points correspond to residual fields of $\leq 100\,\mathrm{nT}$ and hence are more affected by factors like magnetic noise, local material magnetization and inhomogeneities. In addition, the observed change in the skew between the cases of 24 and 34 windings, is owed to differences in the coupling and distribution of the Metglas strips across the cylinder. These are created during construction and can affect the field attenuation profile of the shield. In order to form a more quantitative picture of how the shielding factor improves as a function of the number of wrappings, the average efficiency at the central region of the cylinder is plotted in fig. 5.4, under the same external field conditions. Figures 5.5 and 5.6 show the transverse and axial shielding factors achieved by 34 windings, with typical values of $S_t \approx 400$ and $S_a \approx 170$ at $50\,\mu\mathrm{T}$, respectively.

After having added a total number of 34 windings onto the cylinder's surface it was clear that even with an increase up to 50 windings, it would still be difficult to achieve a shielding factor of the order of 10^3. In addition, the shield weight would increase significantly, disqualifying it from one of the initial objectives of being a lightweight structure. At this point, as layering of windings proved to be a tedious and time consuming process, it was decided to move on to a double-layered configuration. Half the number of windings was removed from the initial shield and was wound around a coaxial cylinder of the same length with an outer diameter of 76 mm, in the same manner. This allowed to investigate the impact of an air gap on field attenuation by separating the same amount of shielding material in two shielding layers. The derived results for a transverse and axial magnetic field are shown in fig. 5.7 and 5.8, respectively. Significantly

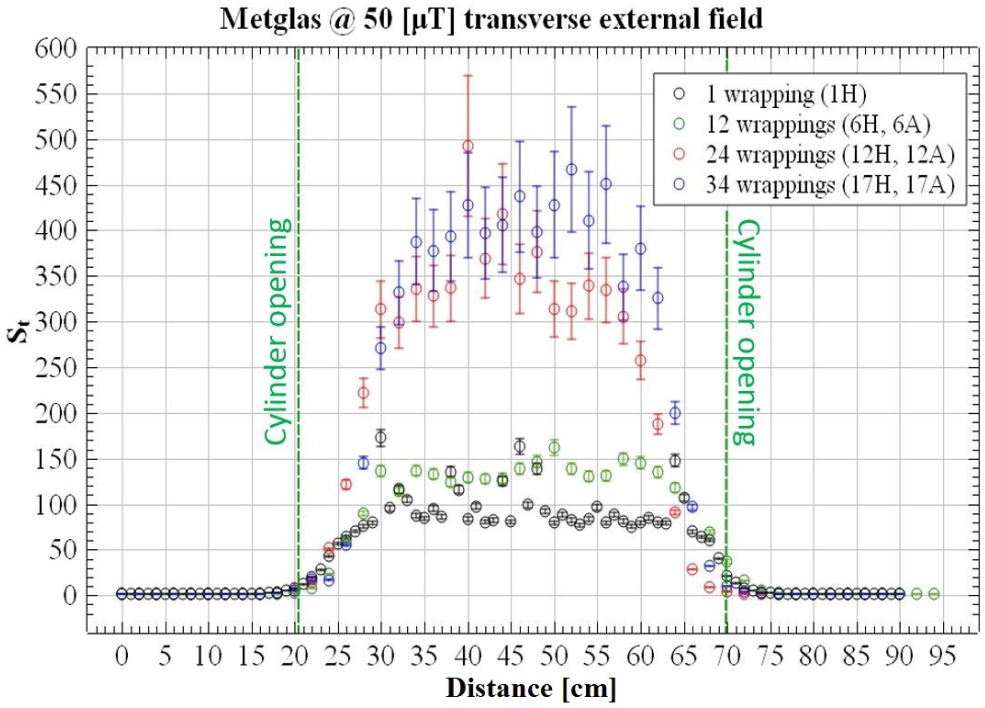

Figure 5.3: Comparison of the mean transverse shielding factor profiles for different number of Metglas windings, under an external field of 50 µT. The change in the plot skew between the 24 and 34 windings is owed to differences in the coupling and distribution of the foil strips across the cylinder.

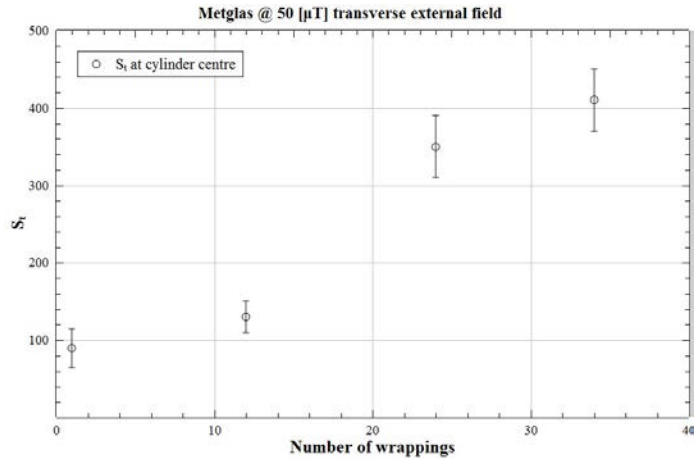

Figure 5.4: Comparison of the mean transverse shielding factor at the central area of the cylinder for different number of Metglas windings, under an external field of 50 µT, respectively.

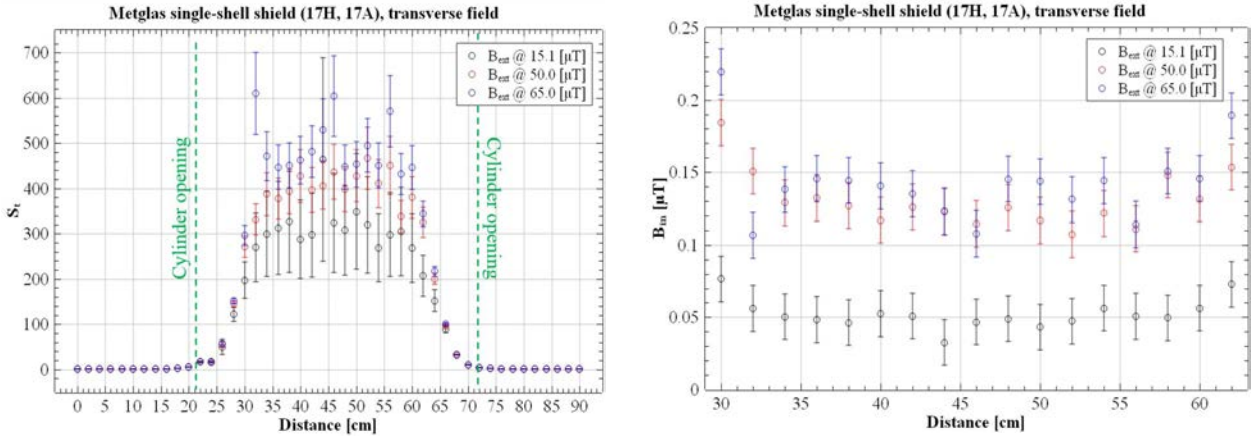

Figure 5.5: (Left) Shielding factor of the single-shell Metglas shield along its axis, for different amplitudes of transverse external magnetic field, respectively. (Right) Plot of the measured residual magnetic field magnitude along the shield's axis, focusing on its central region.

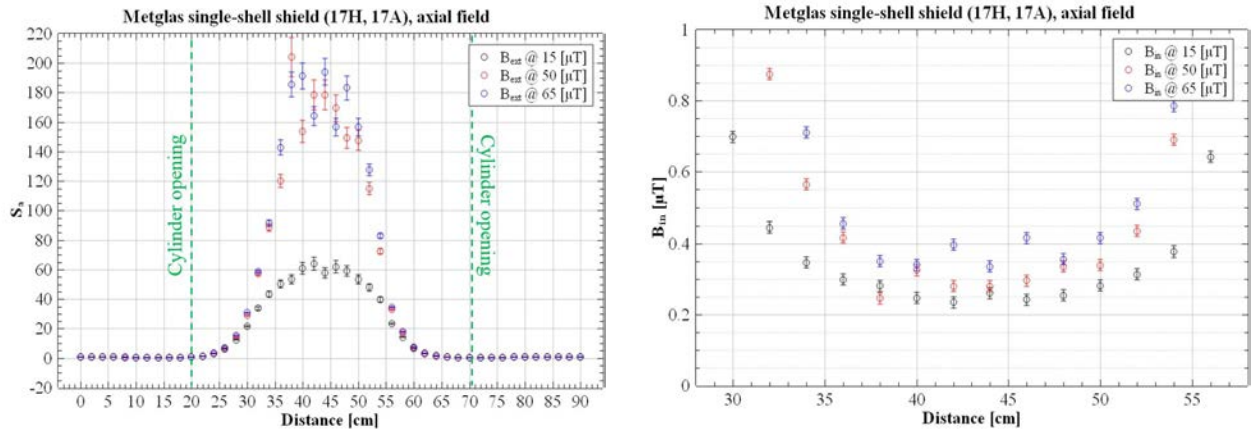

Figure 5.6: (Left) Shielding factor of the single-shell Metglas shield along its axis, for different amplitudes of axial external field, respectively. (Right) Plot of the measured residual magnetic field magnitude along the shield's axis, focusing on its central region.

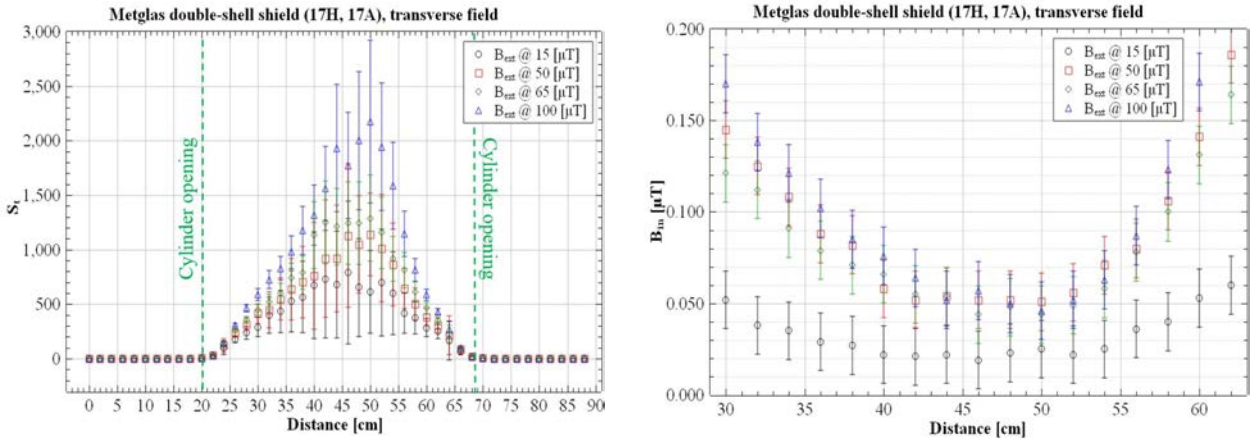

Figure 5.7: (Left) Shielding factor of the double-shell Metglas shield along its axis, for different amplitudes of transverse external field, respectively. (Right) Plot of the measured residual magnetic field magnitude along the shield's axis, focusing on its central region.

higher shielding factors were indicated for the first case, reaching values of around 10^3. In these plots it is evident that for residual field values below 0.05 µT the magnetic noise levels affect the derived shielding efficiency error values quite heavily. An environment with lower ambient magnetic noise like a magnetically shielded chamber would be ideal for these measurements. A comparison between the axial shielding factors of the single and dual layer case (fig. 5.6, 5.8), shows an improvement by a factor of 2 for a low field of 15 µT with an $S_a^{(single)} \approx 60$ and $S_a^{(dual)} \approx 115$, respectively. At 50 µT the results seem to be very similar to lead to certain conclusions. A notable difference however is that the shielding factor grows more rapidly from the open ends towards the centre in the case of the dual-layered shield. A benefit of this is the extension of the high attenuation region over a larger volume. However, the corresponding efficiencies are well below 10^3 in both cases. A comparison plot between the single and double-shell efficiencies is presented in fig. 5.9.

5.1.2 Conclusions

Although Metglas possesses the benefits of high relative permeability and very low coercivity, it gets magnetised easily even under relatively low fields of magnitudes similar to the geomagnetic field. Its ribbon form, as provided by the manufacturer, makes the winding process quite a tedious task for a large area, while making the appearance of tiny slits and material thickness inhomogeneity unavoidable. Non-perfect coupling among the ribbons causes material discontinuities that lead to magnetic flux leakage through the housing. In addition, the sharp foil edges cause local field gradients, especially at the ends of the shield. However, it was observed that the addition of shielding layers generally improves the field homogeneity of the shield. If

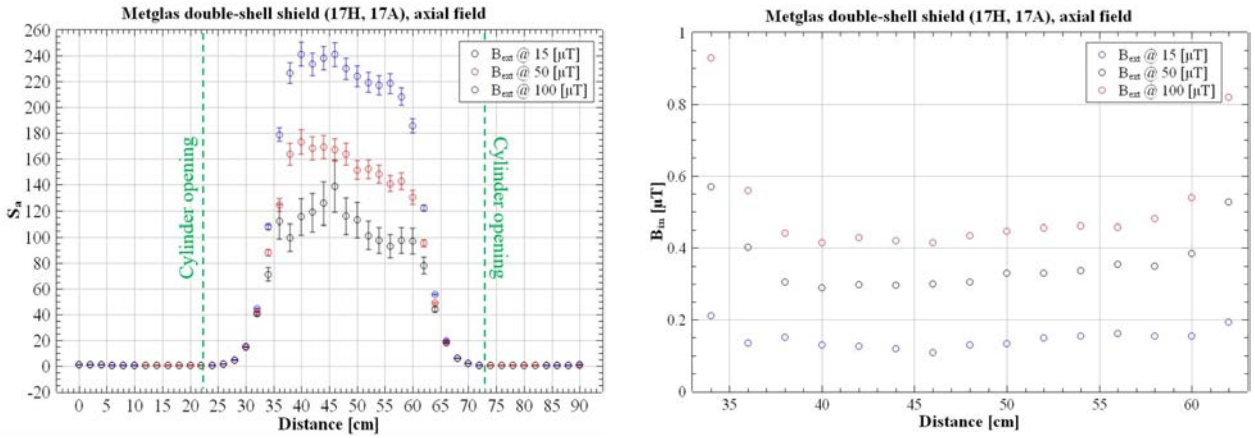

Figure 5.8: (Left) Shielding factor of the double-shell Metglas shield along its axis, for different amplitudes of axial external field, respectively. (Right) Plot of the measured residual magnetic field magnitude along the shield's axis, focusing on its central region.

this proves to be sufficient enough for keeping the local field gradients at a minimum, then the impact on cold atoms might not be very significant.

The benefit of the material's high permeability became apparent when a transverse shielding factor of about 25 was achieved under fields between 40 - 60 µT by using just a single helical wrapping of the 22 µm thin foil. However, although the material saturates easily, the shield's saturation point increases when adding more wrappings. Initially, a maximum number of 34 wrappings was used on a single cylinder which were then separated in two coaxial cylinders. The single-shell housing reached a transverse shielding factor of ~ 400 under an external field of 50 µT. Considering the weight of the used shielding material, this is approximated to ~ 1.3 kg, where $\sim 30\%$ is concentrated at the foil overlaps. A similar shielding factor with the above is predicted to be achieved by a mu-metal shield of the same dimensions, with a wall thickness of 1 mm and $\mu_r \approx 50000$. The mass of this shield calculates to ~ 1.5 kg, which is very close to the Metglas prototype. For this reason, no additional foil wrappings were tested and a double-shell configuration was investigated instead, with the same total number of wrappings. The new configuration reached values around the desired shielding factor of 10^3, under the same conditions, demonstrating the benefit of the multi-shielding effect. This is a good indication that a triple-layered shield would improve the results even further. It should be noted that the rate of improvement becomes limited when the residual field drops bellow the level of 10^2 nT, Under these conditions, factors like material remanence and imperfections become more evident. During the course of the above experiments, such effects were removed by post-processing the acquired data. Therefore, the derived results can be considered as the expected behaviour of the shield in a more idealised case. Experimentally,

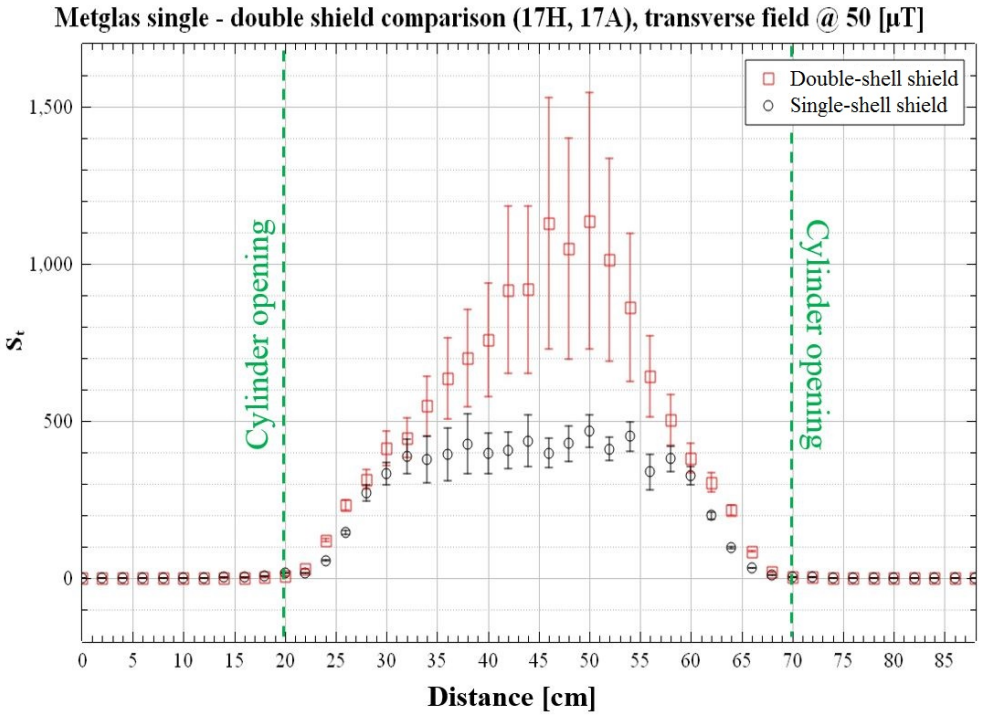

Figure 5.9: Comparison between the transverse shielding factors for single and double-shell Metglas shields with the same total number of windings, under an external magnetic field of 50 µT.

optimisation techniques like degaussing can be applied in order to suppress these negative effects.

The previous experimental observations have shown that apart from its peculiarities, Metglas could still have some potential for the intended application. Future work could include further investigation on the multi-shielding technique, by dividing the material in three or more nested shells and assess the results both in terms of field attenuation and homogeneity. In the case where the shielding factor increases but the local field gradients still cause issues, then the use of this material could still provide some benefits if combined with mu-metal. For example, in the case of a multi-layered shield of mu-metal, one or more of the intermediate layers could be replaced by Metglas, aiming to weight reduction. The fact that Metglas saturates easily, makes it a non-ideal choice as an external layer which acts as a first barrier against the external magnetic fields. Using it as an inner layer would not be a good choice either, since the field gradients that it produces could cause issues during the interferometric measurements. Finally, the initial plan for verifying the feasibility of this technique, was to perform interferometric measurements on the GGtop sensor by using a commercial mu-metal shield first and then replaced it with the Metglas prototype to compare the results. However, good atom launch control had not been established by the end of this thesis, leaving these tests to future work.

5.2 3D-Printed Magnetic Shields for Compact Quantum Sensors

The focus of this project relates to one of the main goals of the QT Hub, which is the development of portable cold atom sensors for applications such as gravimetry, time keeping, magnetometry and others. In particular, the interest was to explore the potential of 3D-printing in the fabrication of magnetic shielding housings. This could open new possibilities in custom-printing shielding housings that can easily adapt to complex geometries, especially beneficial in the efforts towards sensor miniaturisation. Such geometries could deviate from commonly used shapes such as cylinders or cuboids, to tear-drop ellipsoids, or even more shapes following contours that are difficult to machine otherwise. Also, this method enables the printing of structures of varying wall thickness that could prove advantageous in both weight and shielding optimisation. For instance, an increased wall thickness could provide an enhanced field attenuation at the experimental region, while other non-critical regions could be made of a thinner material. In addition, an atomic sensor requires multiple apertures for optical access, wiring and tubing feedthroughs. These features combined with the small size of a portable sensor set 3D-printing ahead from the traditional mu-metal manufacturing methods. By utilising the above considerations, an expected weight reduction by $\sim 20\%$ seems feasible, depending on the system geometry.

The 3D-printing technique tested in this experiment is the *selective laser melting* (SLM) process [91,107], which is a relatively new method compared to conventional techniques such as machining, metal forging or casting. Main benefits of this technique are the flexibility to produce complex geometries fast, by using the desired alloy in the form of atomised powder. This enables for optimal customisation and further experimentation on the alloy composition, while the printing parameters are proved to be affecting the material's microstructural characteristics [15, 26], and hence its magnetic properties [83, 106]. In addition, the fabrication of the parts in argon atmosphere is expected to reduce the amount of oxygen and other impurities within the material. The initially identified challenges for the success of this technique are the high residual stresses that are formed within the crystal lattice by the process and the structural defects, which can affect the material's magnetic properties.

A schematic representation of the main components of a typical SLM is depicted in fig. 5.10. The processing chamber consists of two containers of varying depth and is fed by argon gas. The bottom of each compartment is a moving platform based on a piston, enabling it to move from its bottom end to the top end. Initially, the first compartment which serves as the powder dispenser is filled with the metal powder, while the second compartment where the printing process takes place is empty with its platform fully extended to the top. A small quantity of powder is collected by a scraper arm or roller from the dispenser and is deposited

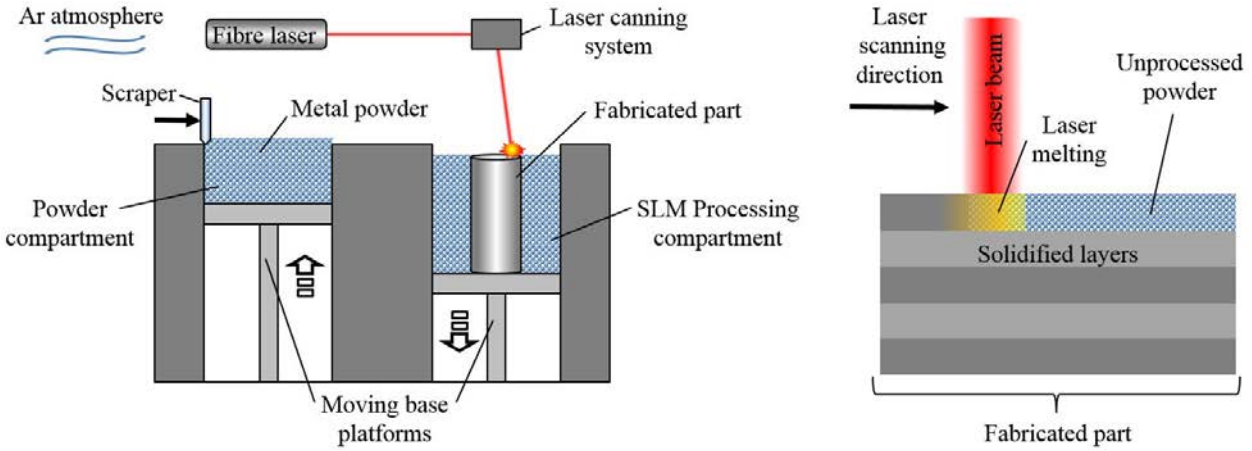

Figure 5.10: Schematic representation of the SLM process system. A quantity of metal powder is collected by a scraper from the powder container surface and is deposited at the top of the fabrication compartment, in the form of a thin layer. A scanning laser is locally melting the powder creating a 3D structure in a layer by layer fashion, as shown in the left figure.

on the second platform, in the form of a thin layer of a couple of microns. Then, the powder grains are locally melted by a high-power laser beam which scans the powder surface. As a result, the scanned pattern forms a thin solid structure after solidification. Then, the dispenser platform moves a step higher while the printing platform an equal step lower, and a new powder layer is spread on its surface again. Repetition of the above process produces a 3D structure which is printed in a layer-by-layer fashion, based on the CAD model which is imported to the computer that controls the scanning laser. Results of this method are strongly correlated to the main process parameters which are discussed in the following subsection.

5.2.1 SLM Process Parameters

At this point it is instructive to make a brief introduction to the SLM parameters that play a critical role on the printed material properties, before moving on to the experimental procedure. These parameters are namely the laser power (P), laser scanning speed (s) and the spacing between parallel laser traces on the powder surface or hatching (h). These three parameters indicate the energy density (ED) input to the material surface during the printing process which is given by [27, 77]

$$\mathrm{ED} = \frac{(\text{laser power})}{(\text{scanning speed}) \times (\text{hatching})} = \frac{P}{s \times h}. \tag{5.1}$$

Here, ED represents a two-dimensional factor since a thin layer of 25 μm was used during the printing process. Each parameter has an effect on the solidification rate of the molten metal, which has been proven to affect

the metal local composition, its lattice constant and grain size. It should be noted that the novelty of the current project was not on the use of 3D-printing to produce a material of optimum mechanical properties but on applying this technique on a soft magnetic material for magnetic shielding applications. The following information is a summary of the findings taken from sources [83, 106].

For a given beam power, as the laser scanning speed increases the power input to the melting and alloying process decreases. At the same time, the temperature gradient increases resulting to a rapid cooling rate for the material, known as *quenching*. High scanning speeds are proven to produce increased porosity and defects in the structure which results to an increase in H_c. In particular, research results so far have led to the following conclusions. The crystallite size increases for higher scanning velocities and low laser power, while the lattice constant decreases, respectively. In the aspect of magnetic properties, higher laser power results to higher saturation magnetisation values. By increasing the scanning velocity starting from very low values, the saturation point increases until it reaches a maximum value and then it drops down again for higher velocities. In terms of coercivity, although it is not very clear how much the laser power affects its behaviour, the laser speed shows an inverse effect compared to the previous case. Relatively high H_c values are observed after using very low scanning speeds and then drop rapidly until they reach a minimum. Further increase in the laser beam speed will start increasing the coercivity values again.

Using the above information as a reference, a series of experiments was planned with the goal of printing a shielding housing prototype that can achieve equivalent performance to the traditional mu-metal shields.

5.2.2 Experimental Results

The material used in the following tests was the Ni-5Mo-15Fe alloy (or permalloy-80), purchased from the TLS Technik company. The powder composition is very similar to mu-metal with particle size of 25 - 50 µm, suitable for SLM processing. All testing samples were produced on the SLM 500 HL 3D printer, hosted in the School of Metallurgy & Materials department facilities, University of Birmingham. At this point, two things need to be noted. By the time of this work there were not many references in literature regarding the SLM processing on permalloy-80. In addition, this was the first time for the collaborating team at the Met. & Mat. department to work on the specific material and perform a magnetic study. Considering this, three production cycles were planned. The first was to familiarise with the material behaviour and perform parametric study.

For this reason, each sample was produced under different SLM parameters which were initially simulated by energy density model. For this reason, the SLM parameters were initially approximated by energy

density modelling simulations [27] and a number of test samples was fabricated under different parameter combinations. A second production cycle would refine the processing parameters to define the optimum conditions. Then, a final magnetic shield prototype would be produced by using these parameters to compare its shielding performance against standard mu-metal shielding housings.

The first optimisation cycle is related to the porosity and cracking within the fabricated structure, which is a function of ED [26, 96]. A porous material develops increased internal stresses and allows impurities to settle in the structure more easily, hindering the magnetic domain wall motion (see §4.1.3). As a result a higher energy is required to magnetise or demagnetise the material, degrading its permeability. The first step was to print a number of small bulk samples with different values of ED until the minimum porosity percentage is achieved. Typically, low ED leaves the melting and recrystallisation process incomplete, while very high ED produces undesired effects during the process like turbulence in the metal liquid, splashes etc. affecting process control and structure homogeneity. The optimum ED value corresponding to the minimum porosity can be found between the two previous extremes. Finally, a heat treatment under hot isostatic pressing (HIP) in argon (Ar) atmosphere was performed for releasing the material's internal stresses and heal most of the pores, which improves the results further.

The first batch of test samples consisted of 18 small bulk cylinders with dimensions of $l = 2\,\text{cm}$, $D = 1\,\text{cm}$ (see fig. 5.11a) which were used for structural and magnetic characterisation, as described below. In addition, 6 larger cylindrical shells of $l = 8\,\text{cm}$, $OD = 5\,\text{cm}$ and wall thickness $t = 3\,\text{mm}$ (see fig. 5.11b) were produced in two versions and used for preliminary shielding tests. The two cylinders were produced with open ends and the other four with closed ends, incorporating an aperture of 3 cm in diameter on the one side, which allows access for the magnetic sensor. The above parts were printed in a single cycle with a production time of approximately two days. However, this time will increase when printing larger structures. In the second batch 63 different rectangular samples of approximately 1 cm width were produced (see fig. 5.11c), this time by varying the parameters close to those corresponding to the best results of the first cycle. At the initial stage of characterization, all parts were tested as built, before applying any heat treatments.

Structural Characterisation

The structural characterisation was initially performed on the optic microscope followed by image analysis. The examined specimen is cut into thin dyes which are polished and then examined on an optical microscope. Pictures are taken from different sections and are analysed by an imaging software which estimates the percentage of porosity. With this relatively simple method it is possible to form a good idea about the

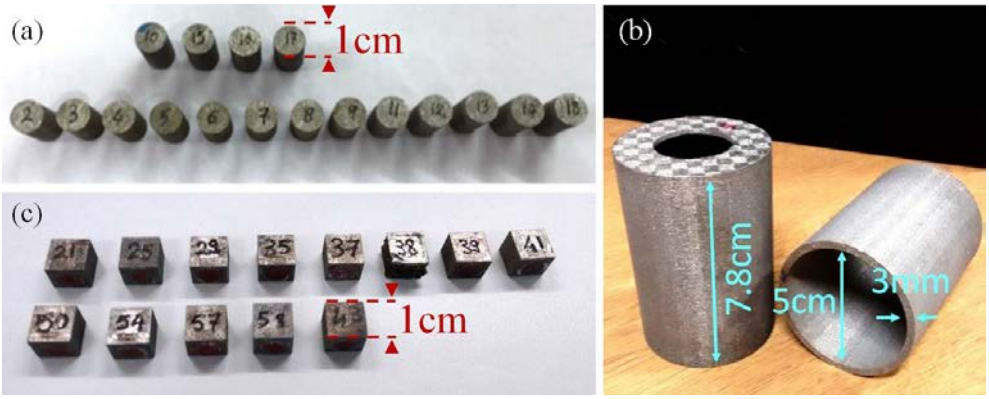

Figure 5.11: 3D-printed samples under different SLM parameters. Bulk samples (a), (c) were used for structural and magnetic characterisation, while the cylindrical shells (b) were tested for shielding efficiency.

structure uniformity and how this is affected by the printing conditions. Figure 5.12 shows an example of pictures captured on microscope. Samples 1, 4 and 5 were printed under the same conditions under ED = 2.033 J/mm^2 resulting to poor reproducibility. Their structure is characterised by pores with unconsolidated particles and cracks. Sample 10 was printed under ED = 4.893 J/mm^2 showing the best results with negligible porosity and only few cracks, typically parallel to the printing direction. However, this method is based on

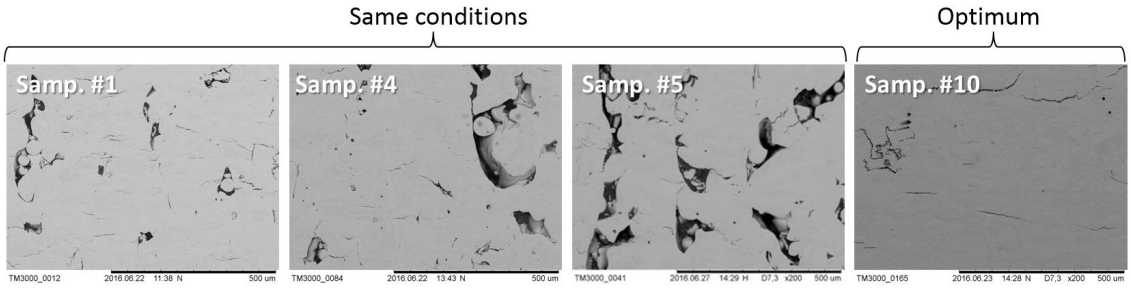

Figure 5.12: Pictures captured by optic microscope on different 3D-printed samples revealing structural defects. Samples 1, 4 and 5 were produced under the same parameters while sample 10 was produced under optimum parameters.

statistical values of porosity derived from certain cross-sections. A more accurate method that considers full sample volume is the Archimedes density measurement which was performed later. Decrease in density means larger number of pores and cracks. In addition, material composition and crystallographic texture were characterised by the X-ray diffraction (XRD) method. The material is polycrystalline and has a face cubic centred (FCC) crystal structure. In this case, not all of the diffraction peaks can be seen, unless the condition that the *Miller indices hkl* [14] are all odd or all even is satisfied. The detected diffraction peaks showed significant variations in the ratio between the two crystallographic orientations (200) and (111) among the printed samples. This ratio would span from approximately 0.5 to 4.7. Furthermore, it was also

varying when testing the same sample in two different planes (see fig. 5.13). This observation raised questions about potential correlations of the material magnetic properties to that variation. For normal XRD tests,

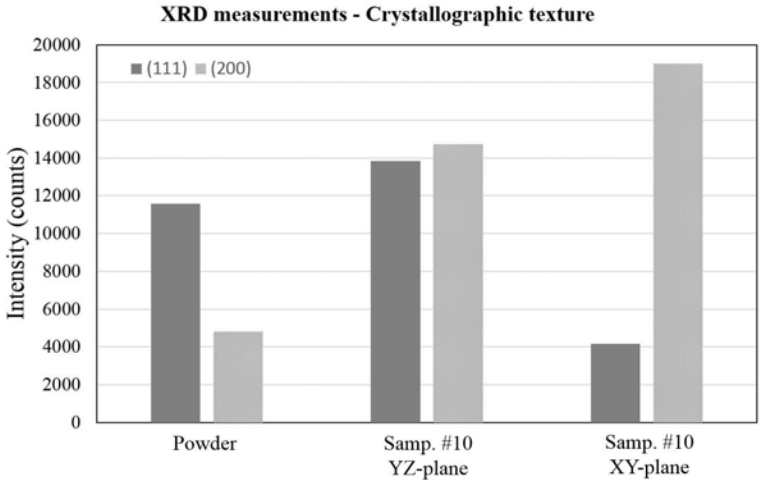

Figure 5.13: Comparison among the results derived from the XRD tests on the the unprocessed permalloy-80 powder and sample 10, along the XY and YZ planes, respectively. Each peak represents the intensity of the detected regions with the same crystallographic orientation. Although both phases are almost equally distributed on the YZ-plane, the (200) orientation dominates in the XY plane.

only micro-stress could be detected by the broadening of the diffraction peaks. However, there are other alternatives to determine different levels of residual stress in the part by using X-ray [95, 124], which have been planned for future work.

Magnetic Characterisation

The magnetic properties for each sample were tested on a vibrating sample magnetometer (VSM), while magnetic shielding tests were performed on the same coil setup used in the previous experiments.

VSM Results

In the standard SLM procedure the percentage in porosity is used for defining the "sweet spot" on the ED diagram. Since the magnetic properties are also investigated in this experiment, the magnetic coercivity was plotted as a function of ED, as shown in fig. 5.14. This way, any correlations of H_c with the printing parameters and structural defects can become more clear. The ED plot in fig. 5.14 can be divided in three main regimes. In the low energy regime (I) the reproducibility is poor and the metal consolidation is inefficient. This results in high H_c values, which indicate a negative impact on the "soft" magnetic properties of the printed parts. A better process control is achieved in regime (II) and therefore the optimum parameters

lie within this region. This is depicted by the low H_c values that were achieved for these samples. The high energy regime (III) starts with loss in geometry control and eventually the results become chaotic due to the high power of the laser beam that causes phenomena like splashes and turbulence in the liquid metal. Results from VSM measurements on both sample batches were plotted as a function of ED and compared with literature [106], showing a good agreement.

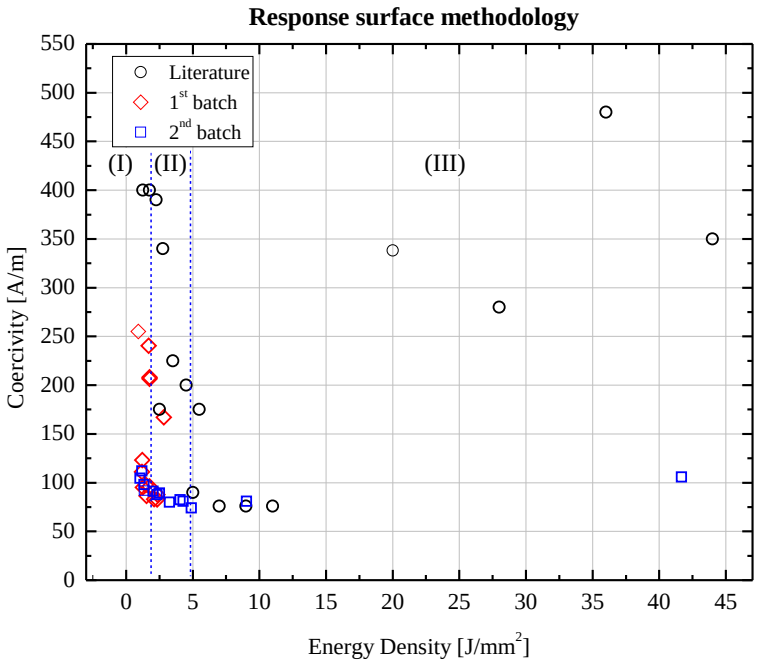

Figure 5.14: Measured magnetic coercivity values as a function of the energy density input during the printing process. VSM results from the first (diamond) and second (square) batch of bulk samples are compared with values sourced from the literature (circle).

In order to investigate the impact of the observed structural anisotropy on the magnetic properties, each sample was measured on VSM in both XY and YZ planes. The derived results are presented in fig. 5.15 where both density and coercivity are plotted simultaneously as a function of ED. This plot is focused in the ED range from 0 to 10 J/mm^2 where circular data points correspond to density values, squares to coercivity in the XY plane and diamonds to coercivity in the YZ plane, respectively. The general trend is that for very low ED values, the density is reduced due to porosity, while the coercivity values are increased. The highest density was achieved in sample 10 under ED = 3.5 J/mm^2. VSM measurements confirmed that variation in the crystallographic structure between the two planes affects the coercivity values. Sample 10 shows relatively low H_c values with small variation in both axes, which is a sign of good "soft" magnetic properties. However, it should be noted that any residual internal stresses that were produced during the SLM process

within the material's structure, will also affect the coercivity values. Therefore, no safe conclusions should be made at this point, as these results might be misleading. The same tests had to be repeated after the HIP treatment. Figure 5.16 shows a comparison plot of the coercivity values prior (open) and post (solid)

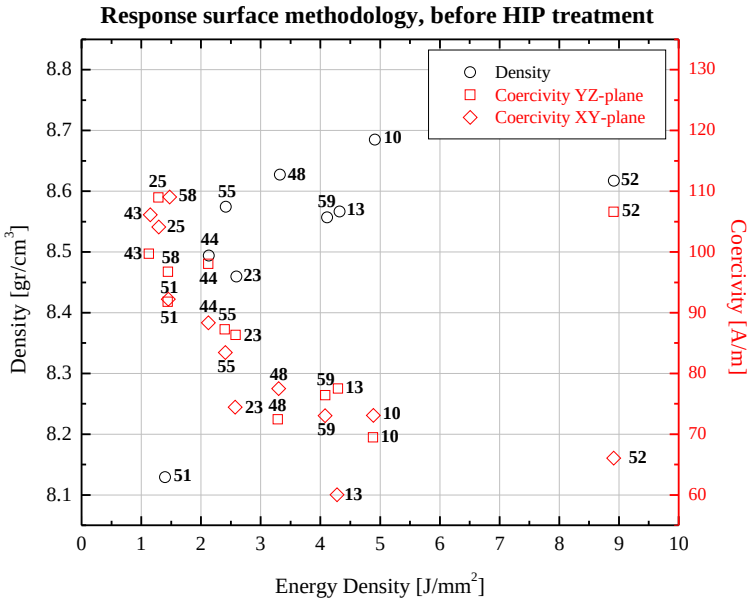

Figure 5.15: Comparison plot showing correlations between sample density (circles) and coercivity values as measured on VSM in the YZ (squares) and XY (diamonds) planes, respectively.

HIP treatment in the YZ (square) and XY (triangle) plane, respectively. As a first observation, a lower H_c was found for all samples. The initial values between $H_c \approx 70 - 110$ dropped between $H_c^{(HIP)} \approx 60 - 40$ after HIP, approximately. In addition, optical images showed pore/crack elimination after HIP-ing. However, the lowest H_c values correspond to the samples at low ED conditions this time and more detailed investigation is required in order to explain this mechanism. Comparison on the H_c difference between the two planes showed a standard deviation of 14 A/m before HIP and 6.7 A/m after the treatment, indicating a drop of the orientation effect. This is an indication of internal stress relaxation that allows for an easier magnetic domain boundary movement in both axes.

Magnetic Shielding Tests

The six printed cylindrical shells were tested for their magnetic shielding effectiveness prior to any kind of heat treatment. The SLM conditions used for each sample are shown in appx. C. In preparation to shielding measurements, all samples were demagnetised after production by using a small degausser. Figure 5.17 shows the shielding factor of the closed (top left) and open (top right) ended samples along the longitudinal axis,

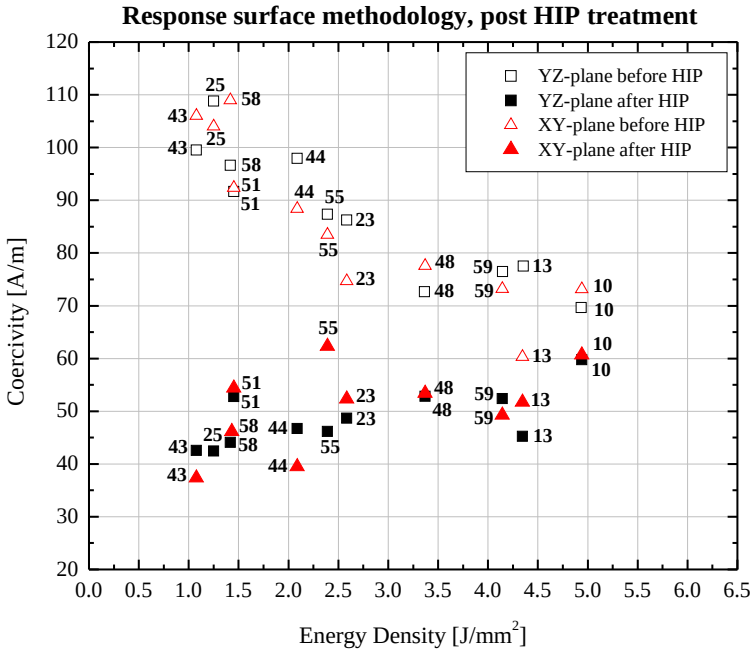

Figure 5.16: Comparison plot showing the coercivity values for the bulk samples prior (open) and post (solid) HIP treatment in the YZ (square) and XY (triangle) planes, respectively.

under a transverse magnetic field of 50 µT. The closed cylinders reached shielding factor values between $S_t = 20 - 25$ at their central region, with increasing values close to their bottom end. Results from the open cylinders were very similar to each other, reaching a shielding factor of $S_t = 14$ at their centre.

In the next experimental step, all of the printed shields apart for sample 1 received a special heat treatment by atomic diffusion in dry hydrogen, which is a standard practice followed in magnetic shield manufacturing. The applied annealing cycle is shown in appx. D. According to the previous discussion, this treatment was expected to improve material permeability and therefore its shielding effectiveness. Samples were retested after annealing under the same conditions as previously and the derived results are presented in the second row of fig. 5.17 for comparison. All samples demonstrated a significant improvement from the initial tests by a factor of approximately 14. In particular, the closed cylinders (mid-left) achieved a shielding factor between $S_t = 250 - 350$ at their central region, while the open cylinders (mid-right) reached a value of approximately $S_t = 200$. The values measured at the bottom end and next to the narrow opening of the closed cylinders are significantly high as the field fringing effect was strong at these regions.

In order to investigate the impact of the HIP treatment on the shielding performance and identify potential differences with the above annealing process, sample 4 went through an intermediate step of HIP treatment prior to the final annealing. The HIP cycle parameters were the same as for the bulk prism samples, shown

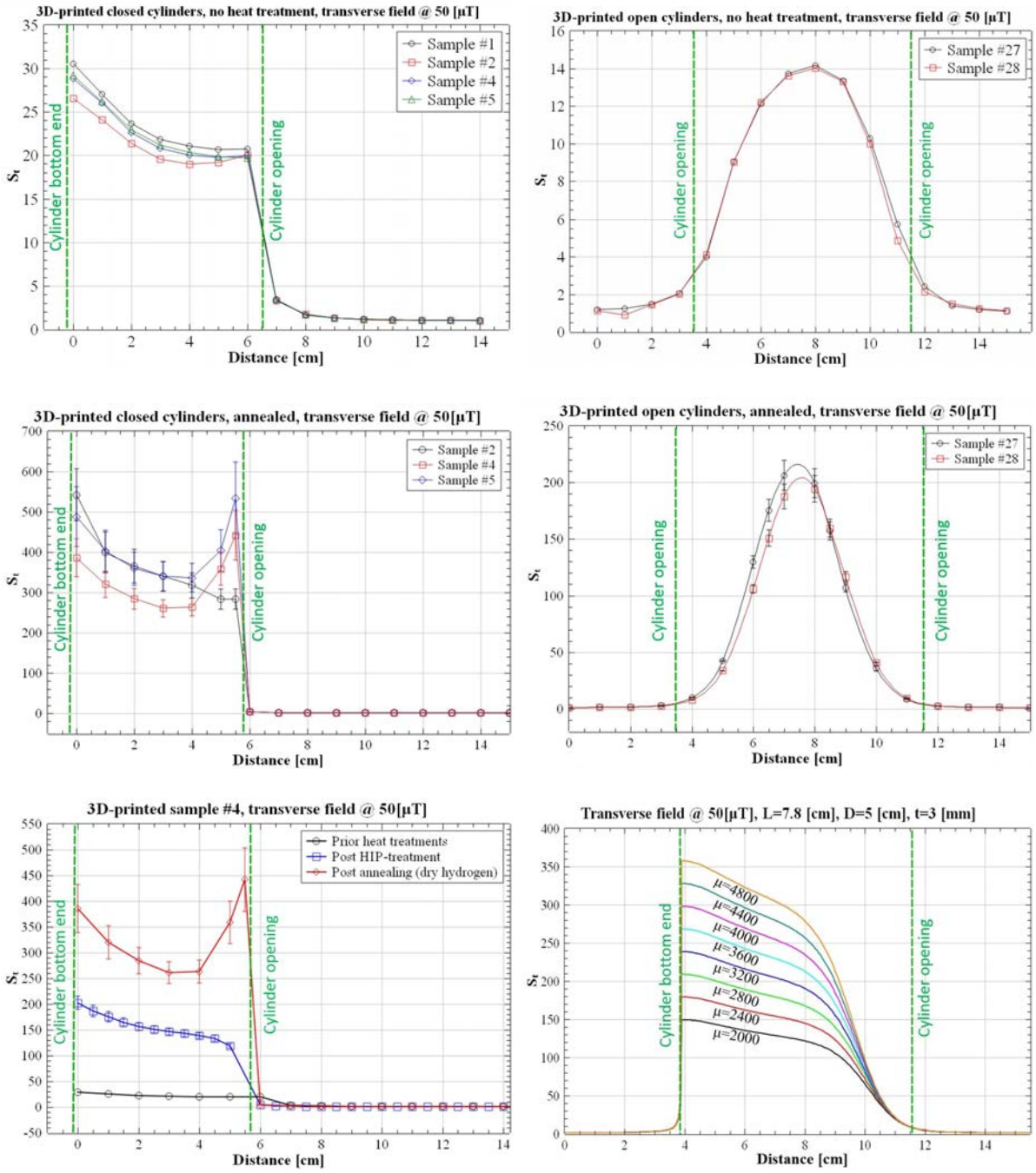

Figure 5.17: Measured shielding factors along the 3D-printed samples' longitudinal axes, under an external magnetic field of 50 μT. Plots at the top row show comparative results among the closed and open cylinders prior to heat treatment, respectively. Post heat treatment results are presented in the graphs of the second row. The first graph of the third row demonstrates the impact of two successive heat treatments on the shielding efficiency of sample 4 (line traces are just to lead the eye). Numerical results from a parametric simulation over different relative permeability values are presented on the right for comparison.

in appx. D . The results derived from magnetic testing in each experimental step are summarised in the plot at the bottom left of fig. 5.17. The shielding factor increased by a factor of 7 after HIP-ing, reaching a value of $S_t \approx 150$ at the cylinder's central region. This factor was then doubled right after annealing, reaching a shielding efficiency of $S_t = 260$, approximately. The fact that all of the other samples demonstrated a very similar performance without undergoing the HIP treatment, could be an indication that this intermediate step might not be necessary for magnetic shielding applications. In that case, opting to follow only one heat treatment instead of two, could potentially reduce the production cost in the future. Finally, a parametric numerical simulation was realised by varying the relative permeability value, in order to derive an "effective" value that matches the above experimental results. The theoretical curves are presented in the lower right plot of fig. 5.17, next to the experimental plot for comparison. According to these results, the permeability of the sample after the HIP treatment can be approximated by the $\mu_r = 2400$ curve, while the results derived after the final annealing can be approximated by the $\mu_r = 4000$ curve. Although these values indicate a significant improvement, they are still lower than the typical permeability values of mu-metal, by an order of magnitude.

The axial shielding factors were also measured at this final step, even though these were expected to be significantly lower than for the transverse field, which are illustrated in fig. 5.18.

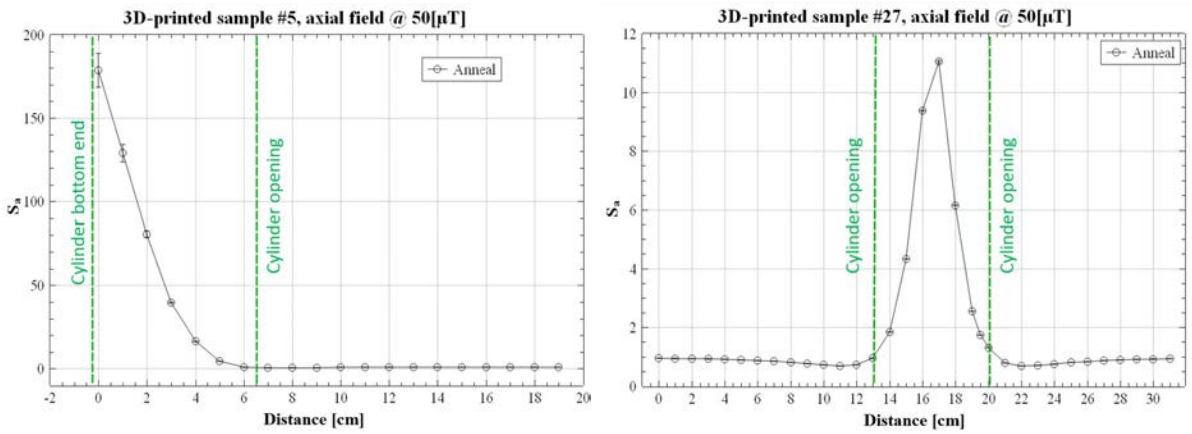

Figure 5.18: Measured shielding factors along the 3D-printed samples' longitudinal axes under an axial external magnetic field of 50 μT.

The plan for the final step of this project was to produce a final shield prototype with optimum SLM conditions and geometry. Shielding efficiency evaluation will define the potential of this technique for magnetic shielding applications. Results from this final step were not yet available by the end of the present thesis and are not presented here.

5.2.3 Conclusions

The above feasibility study showed some encouraging results, indicating that additive manufacturing could be a potential alternative for building magnetic shields for compact quantum sensor applications. However, there are certain areas where more detailed investigation is required to identify all involved mechanisms and establish a robust manufacturing process. In particular, 3D printing was tested as an alternative method for producing magnetic shielding housings, based on selective laser melting process of Ni-5Mo-15Fe alloy powder. The main benefit of the SLM technique over traditional methods is its potential for design customisation that can adapt to complex sensor geometries and minimise the shield weight, whilst ensuring the necessary field attenuation at the experimental region. Although practical demonstrator parts of 3D-printed shields for portable atomic sensors are not available at the moment, a potential weight reduction by $\sim 20\%$ is expected to be feasible by this method.

The printing parameters affect the material microstructure and magnetic properties and had to be optimised first, before printing the final shield prototype. For this reason, a total number of 81 small bulk samples was produced under different conditions for structural and magnetic characterisation. After production, the printed samples were examined under the optical microscope for structural defects, while XRD was used to extract crystallographic and phase information. The results showed that higher mass densities were achieved by an energy density input of 3.5 J/mm^2 or higher. Lower mass densities relate to increased porosity and cracks. In addition, XRD characterisation indicated deferences in crystallographic texture in the XY and YZ - plane, for most of the samples. The magnetic properties were tested on VSM showing a correlation between structural defects and coercivity values. Samples with low porosity indicated lower H_c values, while similar variations between the two orientation planes were observed as with the XRD characterisation. This confirmed that the magnetic properties are affected by the material's microstructural characteristics, which depend on SLM parameters.

The structural defects were almost eliminated for most of the samples after the HIP treatment, while the coercivity values dropped considerably for all samples. In addition, the orientation effect was also minimised. However, although the samples that were produced under low ED values showed the highest initial H_c values, after the HIP treatment they demonstrated the lowest values. Therefore, intermediate ED conditions achieved the best structural characteristics but the best magnetic properties were observed at the low ED region. Further investigation is currently in process in order to establish a better understanding of this mechanism. The samples that were produced under intermediate ED conditions of $\sim$3.5 - 5 J/mm^2, showed the best structural characteristics.

Apart from the small samples, six cylindrical shells were also printed in two versions for preliminary shielding tests. The two samples were built with closed ends, while the other four with open ends. The shields with closed ends reached shielding factor values of $S_t \approx 20 - 25$ under a transverse field of $50\,\mu T$, while for the open ended cylinders $S_t = 14$, respectively. The importance of heat treatment became clear through the findings in the next step, where HIP and annealing in dry hydrogen were applied. Although the HIP treatment is essential for healing the structural defects in the printed alloy, the annealing process had the highest impact, demonstrating an improvement in shielding performance by a factor of ~ 15. The relatively low impact of HIP in the magnetic properties of the material could be an indication that its importance might not be very significant for the particular application. This could potentially decrease the overall production cost in the future.

There is still ongoing work for producing a final shield prototype with both optimum geometry and printing conditions. The new shield will undergo the above heat treatments and will be evaluated for its shielding performance. Apart from bench top tests, the prototype is planed to be used in a simple spectroscopy experiment containing an atom shell for demonstration. Future tests that could be of interest would be to polish the surface of the printed cylinders and investigate if surface roughness affects shielding effectiveness. In addition, 3D-printing provides the essential flexibility enabling for clever joining design solutions for complex enclosure structures. Therefore, further investigation could be led towards this direction as well.

CHAPTER 6

FINAL DISCUSSION

The current experiment was initiated by the Gravity Gradient Technologies and Opportunities Programme (GGtop), aiming to develop a mobile gravity gradient sensor, with the prospect of achieving a sensitivity of $\sim 1\,\mathrm{mE}/\sqrt{\mathrm{Hz}}$. The system has been used as a test-bed for new compact technologies exploiting Raman interferometry on free falling cold atoms of the rubidium-87 species. Some of the expected applications of this sensor include, but are not limited to, sectors such as resource exploration, civil engineering, archaeology and navigation.

The focus of this work is on the magnetic shielding aspects of compact atomic sensors, as part of the development of the GGtop interferometer. Stray magnetic fields are known to cause Zeeman shifts [69, 80] on the internal energy levels of the atoms and undesired accelerations that can affect a cold atom experiment in several ways. The impact of the first order Zeeman effect can be suppressed by using atoms prepared in a magnetically insensitive state; however, they are still susceptible to the second order Zeeman effect which is non-zero. External fields can affect the MOT by imposing limitations in the cooling efficiency and shifting the cloud position. For this experiment, the required temperature to allow for sensitive gravity measurements is of the order of a few µK. In addition, magnetically induced inertial forces have a negative impact on the atom launching control, as well as in the efficiency of the interferometric measurement, where the atom quantisation axis needs to be well defined. As a consequence, shielding a mobile sensor while operating in the field becomes more challenging. In addition, magnetic shields of mu-metal tend to be bulky and heavy. Therefore, a compact design is required for the GGtop interferometer. The required field attenuation for allowing gravitational measurements of human-size targets ($\sim 10^{-9} g_0$) outside the lab environment was determined to be of the order of 10^3. The initial approach was to develop a theoretical model based on the

finite element method (FEM), to aid in the design of a compact magnetic shield of mu-metal, suitable for the GGtop. The study was then extended to alternative methods of magnetic shielding for next generation compact atomic sensors. The main aim was to develop components that could support sensor miniaturization, which is one of the main goals of the Birmingham led UK National Quantum Technology Hub in Sensors and Metrology (QT Hub). In the first method, highly permeable Metglas foil [6] was used to build lightweight shielding housings. Although the use of this material has been demonstrated in other applications [36,75,85], the challenge was to assess its suitability for an atom interferometer where the field uniformity could be compromised due to potential field gradients and leakage caused by the foil windings. The second method that was investigated was additive manufacturing (AM), by using the selective laser melting (SLM) process of permalloy-80 powder, to 3D-print compact shielding housings. The field attenuation becomes a more challenging task as sensor dimensions shrink, exhibiting more complex geometries, while the requirements in weight and size become more stringent. One of the main benefits of 3D-printing is that it enables the production of structures that can adapt to such small and complex geometries. Until the time of this thesis, this was the first attempt of using the SLM technique for magnetic shielding applications on atomic sensors, and therefore no previous references were available in the literature. The main challenge of this method was that the magnetic properties of the processed structure depend on the printing parameters [27, 106]. Therefore, the appropriate process had to be determined for replicating properties equivalent of mu-metal.

6.1 Summary on Findings and Considerations

6.1.1 GGtop Experiment

The GGtop apparatus is organised in two main packages; the physics package and the electronics package, where the priority was given to system compactness, stability and low energy consumption. The physics package comprises of the ultra high vacuum system, and the laser system module. The laser system incorporates three diode laser sources along with the corresponding TAs that provide for the reference, cooling and re-pumper light, respectively. The light distribution was based on a fibre optics network that is carried in the sensor frame together with the spectroscopy box and beat locking electronics box. The Raman light for the interferometer was generated by an external bench-top system based on free space optics, which is planned to be substituted with a more compact system in the future. In order to realise the gradiometer juggling scheme, a 2D-MOT is used as a rapid source of pre-cooled atoms that facilitates the high atom loading rate requirements of at least 10^9 atoms/s. The atoms are transferred to the 3D-MOT for the state preparation,

final cooling stage and launch inside the interferometry tube for realising gravitational measurements. Lastly, the devices in the electronics package are carried on a rack, including the FPGA, DDS's, AOM amplifiers, laser servo controllers, MOT coil current supplies, UPS's and the oscilloscope.

A 3D-MOT with a number of atoms of the order of $\sim 10^8$ and a cloud temperature of $\sim 4\,\mathrm{mK}$ was initially realised. This temperature can be reduced further down to $\sim 50\,\mu\mathrm{K}$ at the final cooling stage, by using the polarisation gradient cooling technique. Although this temperature was still an order of magnitude higher than the required one, it allowed for atom cloud launch and preliminary interferometry tests. The atom launching was performed by using the moving molasses technique, demonstrating tunable initial cloud velocities of the order of $\sim$ 1 - 4 m/s, as in similar experiments [65, 101]. Rabi oscillations were initially observed by illuminating the atoms with Raman light to induce stimulated transitions between the two ground states. An exposure time of $\tau_{\pi/2} \approx 24\,\mu\mathrm{s}$ was determined for setting the population to a linear superposition between the two states [54, 86]. Typical values in similar experiments are kept below $100\,\mu\mathrm{s}$ [65, 115]. This was used in the following preliminary interferometric measurements, where a sequence of two successive $\pi/2$-pulses was applied onto the atoms separated by a time T ($\gg \tau_{\pi/2}$), while scanning the frequency detuning of the Raman light with respect to the atomic resonance ($\delta = \omega_0 - \omega_\mathrm{L}$). Ramsey fringes were acquired by a separation time of $T \approx 130\,\mu\mathrm{s}$, which despite the fair contrast proved that the current experimental setup is capable of realising interferometric measurements.

During the course of the above work, the system encountered stability issues that limited the control and reproducibility of the experimental process. The achieved atom number in the MOT was an order of magnitude lower than the desired one, whilst the position of the atom cloud fluctuated to form varying trapping patterns. From data taken over a period of 40 min [86], drifts of the cloud's centre by $\sim 5\,\mathrm{mm}$ and $\sim 3\,\mathrm{mm}$ were observed in the x and y directions, respectively. One of the consequences of the cloud position shifts is that the spatial light intensity profile "seen" by the atoms between successive measurements will vary significantly, since the beams used for the MOT and the interrogation sequence are Gaussian. In addition,the minimum achieved temperature was limited to $\sim 20\,\mu\mathrm{K}$, which is an order of magnitude higher than the experimental requirements for gravity sensing, as seen in similar experiments [60, 65, 101].

The main factor that has been identified as responsible for these issues is related to light polarisation fluctuations. The light distribution system is based on polarisation maintaining optical fibres which can be affected by environmental temperature fluctuations and mechanical stresses. Temperature variations can affect the refractive index of an optical fibre causing polarisation drifts. These changes can either be local in different sections of the setup, or environmental and they vary hourly and daily. The splitting ratio of the

light in the fibre splitters is also affected by temperature variations, resulting in intensity imbalances of the light among the MOT telescopes. Measurements on the impact of temperature variations that were conducted inside the lab environment in previous work on GGtop [86], showed typical light power drifts of $\sim 15\%$, over the course of a day. In addition, the optical fibres are connected with the individual optical components like the fibre splitters, light extinction switches and the AOMs via splicing. Any imperfections in the splices produce errors that build up across the system, affecting both the output power and polarisation [54]. Furthermore, any applied mechanical stresses onto an optical fibre can cause birefringence and affect the supported mode of the propagating light. This can result in light leakage and generation of parasitic modes which will interfere with the supported mode. An investigation on how these stresses can affect a 3D-MOT telescope fibre was conducted in previous work [54], which showed light power drifts of the order of $\sim 2.7\%$. In order to correct for potential polarisation errors, a polariser is placed at the input of each telescope. As a result, any relative phase offsets of the laser light across the fibre network will translate as intensity variations in the MOT light beams. This can have a significant impact on the cooling efficiency that will affect the atom launching control and the interferometric measurements. This can produce a residual horizontal force at the centre of the MOT that apart from the cooling efficiency, will lead to atom loss during the cloud expansion after launching. In the same work, it was estimated that this force could reach values of up to $\sim 500\,\mathrm{m/s^2}$, which is enough to cause the atoms to collide with the chamber's walls after launching, making an interferometric measurement impossible.

Apart from the effects on the optical components, stray magnetic fields can also affect the shape, position and temperature of the atom cloud. As the MOT coils are switched off during the sub-Doppler cooling stage, any externally induced magnetic forces will accelerate the atoms affecting the cooling efficiency and the atom number, since a fraction of the population will escape from the cooling region. In addition, local magnetic fields can compromise the launching control by imposing horizontal accelerations on the atoms that will distort their trajectory. Lastly, the bias field that determines the atom quantization axis was poorly controlled at this stage, degrading the efficiency of atom interactions with the Raman light during the interferometry stage.

As a final remark, the experimental progress was hindered by frequent failures that occurred on the mechanical fibre switches in the laser distribution system, which are used for complete light extinction. The replacement of these components is a tedious and time consuming task that requires integration in the fibre network through splicing.

6.1.2 Magnetic Shielding

In the first part of the study, a theoretical approach of magnetic shielding problems was performed to derive an order of magnitude approximation of the expected performance of a passive shield against an ambient DC or extremely low frequency (ELF) magnetic field. Many analytical formulae predicting the shielding factor of passive shields can be found in literature, covering the most common basic geometries like nested spherical shells [103], open-ended nested cylindrical shields of infinite and finite length [114, 125], nested cylindrical shells with holes along their axis [89], and others. However, these formulae cannot describe more complex problems involving features such as multiple apertures, joints, localised magnetic field sources, material remanence, etc. As the material and the production of a magnetic shield are expensive (cost of mu-metal, $\sim$ £50/kg), a common practice is to use sophisticated mathematical tools for predicting the performance before manufacturing.

The analysis in this work was based on FEM simulations by using the COMSOL Multiphysics package. Initially, two methods were investigated for reducing the required computational resources and hence the solving time during demanding simulations. The first method takes advantage of the symmetries in the physical problem and simulates a fraction of the full geometry. This is achieved by applying certain symmetry boundary conditions, from which derived solutions can be expanded in the full space. The second technique is related to the *"Magnetic Shielding"* boundary condition, which is available in COMSOL. This condition enables modelling of a thin sheet of metal in the form of a 2D face (or shell), embedded in a 3D geometry. This way, the wall thickness of the simulated shielding housing can be assigned just as a parameter, considerably reducing the number of elements that would be required to mesh a thin 3D wall otherwise. The above techniques were demonstrated in a simple problem of a single cylinder of mu-metal, under a typical background field of 50 µT. The derived results from both cases were compared with the full geometry model and the analytical prediction, showing a good agreement. The established models were used for the design of the GGtop shield and were compared with the experimental data in the next step.

The results from the parametric study confirmed that a shield consisting of multiple nested thin layers would be more efficient than a combination of fewer and thicker layers, with the same weight. A triple-layered shield with 1 mm gauge mu-metal (used for structural integrity) and a layer separation of $\lesssim$ 20 mm, could provide the required shielding factor, while keeping the total weight close to 10 kg. Although the preliminary models of the single-layered shield were in a good agreement with the analytical prediction, it was observed that the derived values for the triple-layered shield were lower than the corresponding analytical ones, in most cases by an order of magnitude. A possible reason for this is that the analytical formulas do not capture

the end effects at the openings as the simulated model does. As a result, even small inaccuracies in the analytical shielding factor values for each individual layer will become more significant when calculating the total shielding factor. Finally, a case study on a more complicated geometry of a compact quantum sensor was presented, in order to demonstrate the benefits provided by the finite element method for capturing and visualising local effects.

A triple-layered mu-metal shield was purchased for the GGtop with a layer thickness of 1 mm and dimensions of $l_1 = 660\,\text{mm}$, $ID_1 = 150\,\text{mm}$ for the inner layer, $l_2 = 670\,\text{mm}$, $ID_2 = 168\,\text{mm}$ for the middle layer and $l_3 = 680\,\text{mm}$, $ID_3 = 188\,\text{mm}$ for the outer layer, respectively. Due to constraints related to the project time lines, the shield was fitted on the interferometer promptly after its arrival and it was characterised a couple of days later. The derived results indicated that the shield had developed magnetic remanence during use with the experiment, yielding a field attenuation factor of ~ 200 at its central region, which is smaller than the required efficiency by an order of magnitude. The main sources are the magnetic fields generated by the MOT coils and the solenoid along the interferometry tube, which defines the quantisation axis for the atoms. Other potential causes could be mechanical stresses induced on the structure during shipping and handling that can cause magnetisation due to magnetostriction. The level of remanence was approximated with the aid of numerical simulations, yielding an "effective" value of $\text{M}_\text{r} = 13\,300\,\text{A/m}$, along the vertical axis. However, the distribution of the magnetisation in the real shield is expected to be non-uniform and depends on factors like the proximity of certain sections to the coils and the different mechanical stresses that each layer has experienced during its use.

The second part of this study is dedicated to alternative passive shielding techniques that aim to weight reduction and enhanced design customisation for portable atomic sensors. The first technique involved the use of Metglas foil to investigate building lightweight shielding housings, by winding multiple strips around a plastic cylinder with a length of $l = 500\,\text{mm}$ and outer diameter of $OD = 110\,\text{mm}$. In previous works it has been demonstrated that the axial windings work best against an axial magnetic field, while the circular windings are more effective against a transverse field [31,75,85]. After confirming these results experimentally, a combination of successive helical and axial windings was decided for the experimental prototype, aiming to produce a more uniform shielding effect. Several trials were performed by adding strips of Metglas on a single cylinder and testing the magnetic field attenuation against a DC external field. A total number of 34 windings yielded a shielding factor of $\text{S}_\text{t} \approx 400$ against a transverse external field of 50 µT and $\text{S}_\text{a} \approx 170$ under the same field magnitude in the axial orientation. It was observed that the relative improvement in shielding efficiency after the addition of 20 windings was gradually becoming smaller, indicating that more than 80

windings would be required in order to reach a shielding factor of the order of 10^3. For this reason it was decided to split half of the shielding material into two nested shielding shells and assess the improvements due to the introduced air-gap. The dimensions of the dual-layered configuration were $l_1 = 500\,\text{mm}$, $OD_1 = 76\,\text{mm}$ for the inner and $l_2 = 500\,\text{mm}$, $OD_2 = 110\,\text{mm}$ for the outer layer. The new shield was tested under the same conditions as previously, yielding shielding efficiencies of $S_t \approx 1000$ and $S_a \approx 170$ for transverse and axial fields, respectively. Although this prototype reached the target performance under a transverse field, its attenuation factor against the axial field remained the same as the initial configuration. However, a notable improvement was observed in terms of the residual field profile, which drops more rapidly from the shield's ends towards its centre. This resulted in an increase in the width of the shielding factor profile at the central area by a factor of ~ 3.5. The above findings indicate that the shielding performance could potentially improve even further by using a triple-layered configuration.

Some peculiarities that are related to Metglas imposed certain challenges in achieving the experimental goal. Although Metglas demonstrates high magnetic permeability and very low coercivity, it is very thin and saturates easily, even under typical background magnetic fields of less than $100\,\mu\text{T}$. In addition, it is provided in the form of a 50 mm wide ribbon, which makes its application process over larger structures relatively impractical. Another challenge is the non-perfect coupling between the foil strips that form the shield. These material discontinuities lead to magnetic field flux leakage through the housing and produce local field gradients. Such effects are expected to have a negative impact on the performance of an atom interferometer like the GGtop. However, an encouraging observation was that the addition of nested shielding shells generally improves the field homogeneity inside the shield. This indicates that the undesired field gradients could be reduced even further.

In the last part of this study, 3D printing was tested as an alternative method for producing magnetic shielding housing out of metal powder. The used alloy was the permalloy-80 (Ni-5Mo-15Fe) which has a very similar composition to mu-metal. The structural and magnetic characteristics of the printed structures are affected by the process parameters which had to be optimised first. A total number of 81 small bulk samples was produced under different conditions for structural and magnetic characterisation. The values of the energy density (ED) input on the powder bed that were used to produce the test samples ranged between $\sim 1 - 45\,\text{J/mm}^2$. Depending on these values, the results can be divided in three regimes. In the low energy regime of ED $\approx 1 - 2.5\,\text{J/mm}^2$, the metal consolidation was inefficient with poor reproducibility, increasing structural defects like porosity and cracks. For ED $\approx 2.5 - 5\,\text{J/mm}^2$, the results showed a significant improvement, achieving a good process control with reduced defects. These defects became minimal for values

higher than $3.5\,\mathrm{J/mm^2}$. Lastly, the values of ED $\geq 5\,\mathrm{J/mm^2}$ proved to be too high for the process by initially causing loss of geometry control, until the results become chaotic at the highest values. The results from the XRD characterisation indicated variations in the ratio between the (200) and (111) crystallographic phases, approximately ranging from 0.5 to 4.7. Furthermore, these ratios varied when testing the same sample along the XY and YZ planes, with the z-axis being the printing axis.

In order to evaluate the "soft" magnetic properties of the material, the magnetic coercivity values H_c were extracted from measurements on a vibrating sample magnetometer (VSM), prior to any heat treatments. The derived magnetic coercivity values were compared with results from the literature [106], showing a good agreement. The samples with low porosity demonstrated a lower H_c value, indicating that the material retains a very low remanence and can be easily magnetised, whereas the samples with increased structural defects require a higher magnetisation energy and had the highest H_c values. In addition, by measuring the coercivity values along the XY and YZ planes it was observed that these were correlated with the corresponding structural variations along the same orientations. Therefore, the conducted experiments confirmed that the magnetic properties are affected by the material's microstructural characteristics, which depend on the SLM parameters.

The above measurements were repeated after applying the hot isostatic pressing (HIP) treatment in argon atmosphere. The results showed that the structural defects were almost eliminated for most of the samples. The coercivity values were also reduced considerably, while the differences between the to orientations were minimised. By comparing the general trend of the results prior and post HIPing, it was observed that the samples that were produced in the low ED regime had initially demonstrated the highest H_c values. In contrast, the same samples were the ones with the lowest H_c values after the heat treatment. Therefore, the best structural characteristics were achieved under intermediate ED conditions, while the best magnetic properties were achieved at the lower ED region. The responsible mechanism for this behaviour is currently unclear and further tests are being conducted.

In addition to the above test samples, six cylindrical shells were also manufactured for preliminary shielding tests. The four shields were built with closed ends and showed an initial shielding efficiency of $S_t \approx 20-25$ under a transverse field of $50\,\mu\mathrm{T}$. The other two prototypes with open ends reached $S_t = 14$, respectively. The importance of the heat treatment became clear through the findings in the next step, where HIP and annealing in dry hydrogen were applied. Although HIP is essential for healing structural defects through the printed alloy, the latter technique had the highest impact, demonstrating an improvement in shielding performance by a factor of ~ 15. The relatively low impact of HIP by a factor of ~ 7 in the achieved shielding

ADVANTAGES	DISADVANTAGES
Mu-metal	
Homogeneous material providing field uniformity.	Heavy structures.
Can produce structures in virtually any size.	Difficult to manufacture small and complex geometries.
Commercially established – existing know-how.	Many tooling steps involved during production.
Metglas	
Lightweight shielding structures.	Reduced field uniformity due to windings.
Can form small or intermediate sized shields for transportable sensors.	Impractical for relatively large structures.
High relative magnetic permeability ($\sim 10^5$).	Very thin, it saturates easily.
Flexible, can follow contours easily.	It requires a support structure for the windings.
	Shielding efficiency varies with different winding orientation.
3D-printing	
Can adapt to complex geometries.	Shield size limited by the dimensions of the printing compartment (here, $\sim 25\,\mathrm{cm}^3$).
Rapid manufacturing for bespoke parts.	Cost per kg of Permalloy powder is at least 2 times higher than bulk mu-metal.
Suitable for portable/miniaturised sensors.	Requires HIPing which increases the process steps and cost.
Can print composite shielding structures with embedded layers of different materials or/and vacuum separations.	Structural and magnetic characteristics depend on the printing conditions; further optimisation required to reach mu-metal performance.
Wall thickness can be varied at certain sections for increasing the field attenuation and reducing weight.	

Table 6.1: Summary of the key findings of the investigated shielding methods.

factor could be an indication that it could potentially be skipped for this application, reducing the production cost in the future. It should be noted that the conditions that were chosen for the above heat treatments are standardised for similar materials and are not optimised for 3D-printed permalloy-80. A summary of the advantages and disadvantages for each of the three examined shielding methods is presented in tab. 6.1.

6.2 Recommendations for Future Work

6.2.1 GGtop Experiment

The issues that were highlighted in the above discussion indicate that there is plenty of experimental room for future work on improving the current state of the atomic sensor. One of the key causes that limited the performance of the experiment was the light polarisation instability. Therefore, further work needs to be undertaken on improving the laser distribution system. An effective way to mitigate this would be by redesigning the system in order to reduce its complexity and number of components, where possible. A more simplified setup is expected to demonstrate reduced errors and power losses, while further research is required in order to find more reliable replacements for the mechanical fibre switches. A new scheme that uses a single laser for atom cooling and Raman transitions has been proposed for the GGtop to substitute the existing laser sources, aiming towards this direction. A preliminary work on this has already been initiated and can be found in [54]. In addition, as the focus of the experiment is on the applications, its setup was based on readily available commercial components. However, there is ongoing research in novel technologies which can be used in the future to shrink an entire optical system to a system integrated on a chip. Some early examples can be found in [13,70]. Therefore, the all-in-fibre approach should not be abandoned, as it has high potential benefits in terms of portability and robustness. Instead, a careful choice of reliable components and special care during assembly, combined with a refined scheme are expected to make a significant improvement.

Further improvements can also be made on the system's electronics. For instance, the control sequence of the final sub-Doppler cooling stage could be optimised further, enabling for a smoother ramping on frequency and intensity. This could potentially improve the cooling efficiency and reproducibility.

The next area for future work is related to the protection of the system from external factors, such as the temperature variations, mechanical vibrations and magnetic fields. A task related to the first case is to build a temperature stabilisation system to suppress temperature drifts. The implementation of such a system will improve the light beam balance and enable for fine tuning the temperature conditions inside the laser distribution box. In this way, the light intensity balance among the MOT telescopes can be optimised even further. Regarding the mechanical vibrations, these can be suppressed by the installation of a stabilisation platform with vibration isolation capability. Finally, the work related to magnetic shielding is discussed in the following subsection.

6.2.2 Magnetic Shielding

The outcome of the work undertaken on the numerical simulations and the GGtop shield characterisation have indicated areas for future work. Some suggested implementations on the work related to the numerical simulations are outlined below. Using a reliable B(H) curve instead of a constant permeability value would provide a more realistic approach to the problem, especially for multi-layered shielding structures. This is because each layer experiences a different magnetic field magnitude, which decreases from the outside to the inside of the structure. Since the magnetic permeability depends on the local field, its value will vary for each shell accordingly, yielding a lower total shielding factor than the one predicted by the simplified linear model. Also, real materials tend to store some remanent magnetisation which also affects the shielding performance. Statistical knowledge of typical remanence values would allow for incorporation of these effects in the simulated models, providing more representative results for real life applications. Finally, a relation of the permeability dependence on tensile stresses or temperature variations could be implemented for studying various mounting configurations and the impact of the environmental conditions on the shielding performance during a field survey.

Moving on to the experimental stage, the GGtop interferometer is currently shielded by a triple-layered shield of mu-metal. Further characterisation is required in order to determine the level and the distribution of the remanence that was observed during the preliminary tests. The next step would be to restore the magnetic properties by degaussing, which is commonly used in other experiments as well [10, 120]. In addition, a shield operating on a mobile sensor in the field is expected to develop remanence more often than in the case of a lab-based experiment. Therefore, an easily integrable degaussing system would be beneficial. The 3D-MOT section is another area which requires magnetic shielding. The implementation of an active compensation system or an additional passive shield, is expected to improve the MOT efficiency and atom launch control.

It should be noted that the above work focused on the magnetic shielding technique against DC (or ELF) fields. However, AC fields are also present during the experimental process. As the shielding method against these fields relies on different mechanisms, these were not examined here. Therefore, a topic for future research could focus on shielding techniques against AC fields.

With regards to the alternative shielding techniques, the experimental observations showed that apart from its peculiarities, Metglas could still have some potential for the intended application. Future work could include further investigation on the multi-shielding technique, by dividing the material into three or more nested shells and assess the results both in terms of field attenuation and homogeneity. In the case where the shielding factor increases but the local field gradients still cause issues, then the use of this material

could still provide some benefits if combined with mu-metal. For example, in the case of a multi-layered shield of mu-metal, one or more of the intermediate layers could be replaced by Metglas, aiming to reduce weight. The fact that Metglas saturates easily makes it a non-ideal choice as an external layer which acts as a first barrier against the external magnetic fields. Using it as an inner layer would not be a good choice either, since the field gradients that it produces could cause issues during the interferometric measurements. Finally, the initial plan for verifying the feasibility of this technique was to test it on the experiment, while measuring gravity. The results derived by using a commercial mu-metal shield would be compared with the results derived after substituting it with the Metglas prototype. However, by the end of this thesis, good launch control of the atoms had yet to be established and therefore these experiments should be considered in the future work.

There is still ongoing work on producing a final shield prototype with optimised geometry and printing conditions. A part of this work should also involve an investigation in optimising the applied heat treatments, since these proved to have a significant impact on the results. The performance of the final prototype will be compared to a mu-metal replica in order to evaluate its performance. The prototype could be used in a simple spectroscopy experiment containing an atom shell for demonstration. Future tests that could be of interest would be to polish the surface of the printed cylinders and investigate if surface roughness affects the shielding effectiveness. In addition, 3D-printing provides the essential flexibility enabling for clever joining design solutions for complex enclosure structures. Therefore, further investigation could be led towards this direction as well.

6.3 Future Milestones

The vision of the QT Hub [113] is to provide the supply chain of technologies for components that will be used for system prototyping, aiming to develop sophisticated modules that will exceed the current state-of-the-art systems. The final aim is to build a market with new solutions on applications for end-users, based on quantum technology. Some examples of such applications are underground mapping for civil engineering and archaeology, climate space missions and navigation systems. GGtop is one of the key systems among these programmes that is used as a test-bed for developing novel portable technologies for the next generation gravity sensing devises.

Once gravity sensing is established on GGtop inside the lab, then the sensor will operate in gradiometer mode. The next goals are to deploy the optimised system for field measurements at known targets and make a direct comparison with the commercial spring based gravimeter Scintrex CG-5 [79], which is operated by

project partners in the Civil Engineering department of the University. The site that is planned for the initial outdoor measurements is the University's mines, with tunnels of $\sim 1.5\,\mathrm{m}$ in diameter, buried at a similar depth.

Once operation in the field is successful, then the sensor will be calibrated in terms of absolute gravity sensing against another system used as a standard. A proposed candidate location for this task is the Natural Environment Research Council (NERC) geodesy facility at Herstmonceux in Sussex, UK, which hosts an FG5-X free falling corner-cube interferometer [3, 24].

The high sensitivity of the atomic sensors against stray magnetic fields, combined with fact that magnetic shielding becomes more challenging in applications concerning portable systems, is expected to attract more interest in the near future. Therefore, the development of more efficient methods like 3D-printing to produce robust and efficient magnetic shielding structures with clever joining techniques is prone to become a standard requirement.

Further investigation in the SLM process parameters combined with optimised heat treatments can potentially enable these structures for reaching shielding efficiencies similar to mu-metal, with the benefit of achieving higher geometrical complexity, suitable for compact systems.

6.4 Other Positive Outcomes

The project on 3D-printing for magnetic shields opened new opportunities for collaborations, attracting industrial interest as well. The Metallurgy & Materials department was the initial partner from the start of this work while Magnetic Shields Ltd. joined both the project and Quantum Hub during the second stage. In addition, a joined Innovate UK proposal was submitted by the same partners for the continuation of this study under the name of "QT Shield" and has been accepted.

APPENDIX A

COMMON MAGNETIC SHIELDING MATERIALS

High magnetic permeability materials are being used for magnetic shielding DC or extremely low frequency (ELF) fields. In the case of AC and RF fields however, the shielding mechanism is achieved by induced eddy currents under the surface of the shielding housing. High electrical conductivity materials are being used in these applications instead. Table A.1 shows a comparison of the initial magnetic relative permeability and electrical conductivity of different materials.

Table A.1: Comparison among typical values of initial magnetic relative permeability and electrical conductivity of different materials (information sourced from [121]).

Source	Initial relative permeability	Conductivity (% IACS[2])
Annealed copper (100 Cu)	1	100
Cold-rolled steel (0.5 Mn, 0.06 C)	200	12
Commercial iron (99.8 Fe)	250	16
Purified iron (99.95 Fe)	10000	18
Supermalloy (79 Ni, 5.0 Mo, 15 Fe)	100000	2.87
78 Permalloy (78.5 Ni, 21.5 Fe)	8000	10.8
Mumetal (77 Ni, 5 Cu, 2 Mo, 15 Fe)	20000	2.87

[2]International Annealed Copper Standard, defined at 20° ($\times$ 1.7241 $\cdot 10^{-6}$ S/m)

APPENDIX B

MAGNETIC MEASUREMENTS

More than one field contributions are involved during a practical measurement of the magnetic field magnitude $B_{meas.}$, inside a magnetic shield. The first is the attenuated or residual field $B_{res.}$ which comes from the outside, while the second one is the field component owed to shield's remanence $B_{sh.}$.

The technique used to filter out the field contributions due to shield remanence was to acquire two field readings $B^{+}_{meas.}$ and $B^{-}_{meas.}$ at the same position, by inverting the magnetising field direction through the coils. Then, the corrected field value was taken as $B_{corr.} = (B^{+}_{meas.} - B^{-}_{meas.})/2$. This technique is schematically represented in fig. B.1, along with a similar one where the shield's ends are flipped instead.

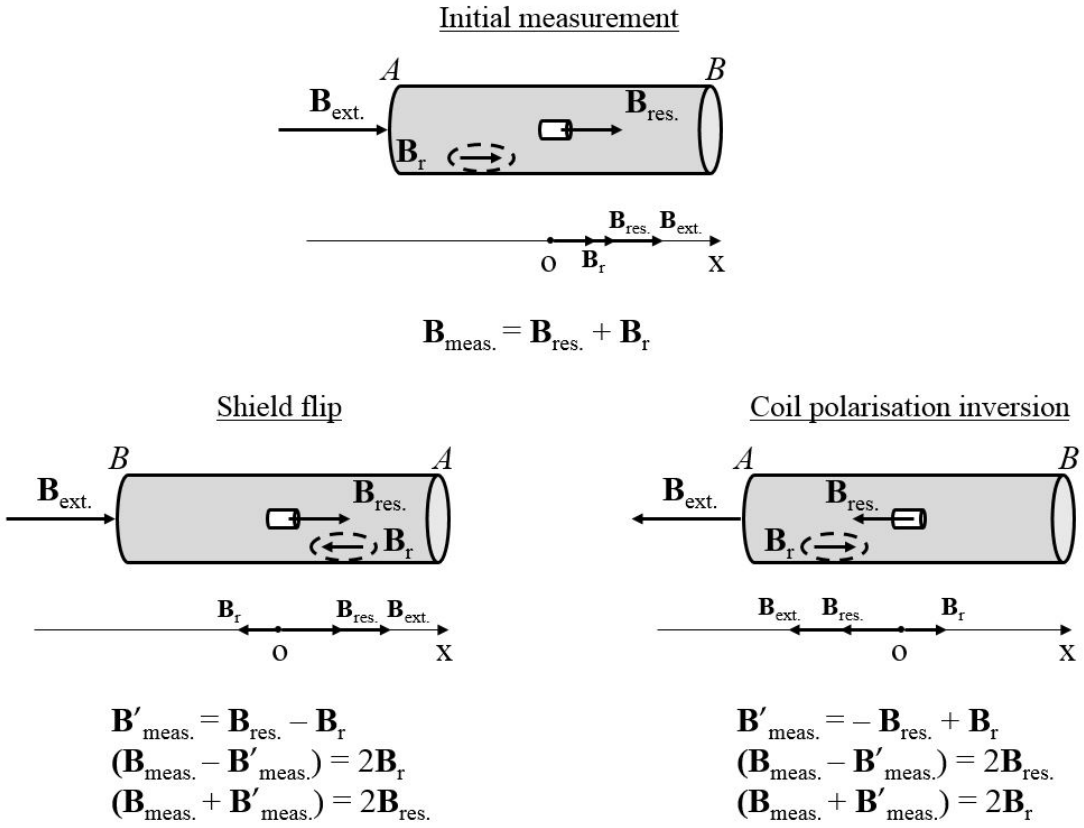

Figure B.1: Schematic representation of the techniques used for identifying the contributions from the shield's remanence during a magnetic test. The first figure represents an example of the first take. Then, repeating the measurement by flipping the shield's ends, allows for identifying the magnetic field component B_r owed to remanence. A similar technique is shown in the next sub-figure, where the field polarisation is inverted instead.

APPENDIX C

SLM PARAMETERS FOR 3D PRINTED SHIELDS

The initial 3D printed shield prototypes were produced along with the first batch of the small bulk samples, in order to be used for preliminary shielding tests. Each sample was produced under different SLM parameters which are summarised in table C.1.

Table C.1: SLM parameters used during the initial process optimisation study. Parameter AR stands for the laser beam diameter to hatch spacing ratio, while ED is the energy density input of the melting laser beam onto the metal powder surface.

Sample No	Power [W]	Scan Speed [mm/s]	AR	ED [J/mm^2]	Ends
1	265	1000	0.35	5048	Closed
2	265	1000	0.5	3533	Closed
3	110	400	0.5	3667	Closed
4	265	1000	0.5	3533	Closed
5	265	1000	0.5	3533	Closed
27	200	1600	0.5	1667	Open
28	200	1734	0.5	1538	Open

APPENDIX D

PERMALLOY–80: HEAT TREATMENT CYCLES

Special heat treatments are commonly used to alter/enhance the physical properties of a material. Two different types of heat treatment were applied to the samples produced by SLM manufacturing of permalloy–80.

The first method is known as hot isostatic pressing (HIP) and was performed at the School of Metallurgy & Materials, University of Birmingham. The process parameters are shown in the time–temperature diagram in fig. D.1. The selected cycle for this design of experiments is typically used for 3D printed materials of similar composition, predominantly to eliminate structural defects. However, this process is not yet optimised with regards to the magnetic properties of the material.

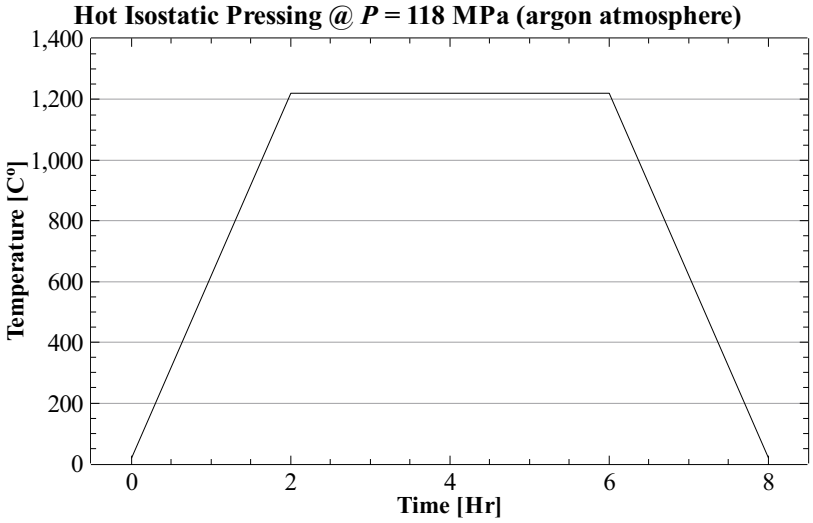

Figure D.1: Hot isostatic pressing process cycle in argon atmosphere for the 3D printed samples, as performed at School of Met. & Mat., UoB.

The second method is annealing in pure dry hydrogen, which was undertaken at the Magnetic Shields Ltd. facilities. This cycle is being used commercially by the company for bringing mu-metal shields to optimum magnetic performance as the final step after manufacturing. The relevant parameters are shown in fig. D.2.

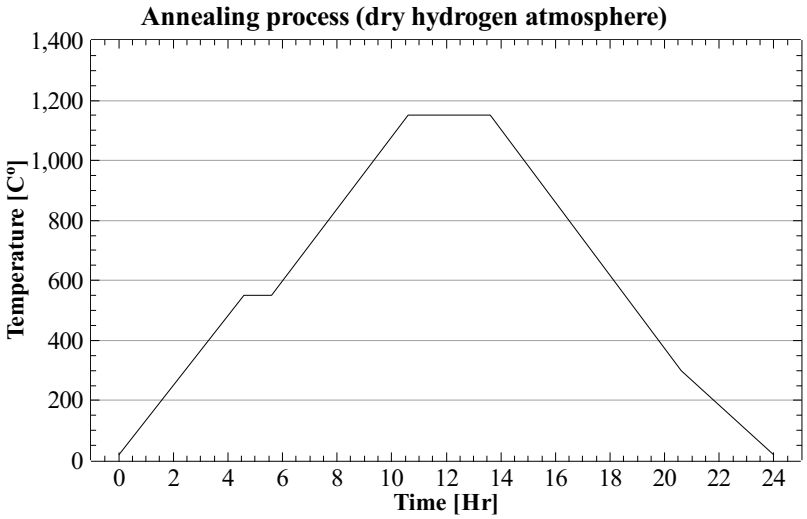

Figure D.2: Annealing treatment cycle in pure hydrogen atmosphere for the 3D printed samples, as performed at MSL.

LIST OF REFERENCES

[1] AOSense - Sensors for a Quantum World. http://aosense.com/solutions/. Accessed: 10-08-2016.

[2] COMSOL Multiphysics User's Guide (Version 4.3). people.ee.ethz.ch/∼fieldcom/pps-comsol/documents/User%20Guide/COMSOLMultiphysicsUsersGuide.pdf. Accessed: 16-01-2014.

[3] FG5-X Absolute Gravimeter. http://www.microglacoste.com/fg5x.php. Accessed: 10-07-2013.

[4] gPhoneX Gravimeter. http://www.microglacoste.com/gPhoneX.php. Accessed: 10-07-2013.

[5] Magnetic Shields Ltd., B(H) Curves. http://magneticshields.co.uk/index.php/en/technical/b-h-curves. Accessed: 15-01-2014.

[6] Metglas 2705m technical bulletin. http://www.metglas.com/assets/pdf/2705m.pdf. Accessed: 20-01-2014.

[7] μQUANS Precision Quantum Sensors. https://www.muquans.com/index.php/products. Accessed: 10-08-2016.

[8] Twinleaf - Vector SERF magnetometers. http://www.twinleaf.com/magnetometer/vector/. Accessed: 07-07-2016.

[9] World Health Organization. http://www.who.int. Accessed: 13-09-2016.

[10] I. Altarev, E. Babcock, D. Beck, M. Burghoff, S. Chesnevskaya, T. Chupp, S. Degenkolb, I. Fan, P. Fierlinger, A. Frei, and E. Gutsmiedl. A magnetically shielded room with ultra low residual field and gradient. *Review of scientific instruments*, 85(7):075106, 2014.

[11] I. Altarev, P. Fierlinger, T. Lins, M. Marino, B. Nießen, G. Petzoldt, M. Reisner, S. Stuiber, M. Sturm, J. Taggart Singh, and B. Taubenheim. Minimizing magnetic fields for precision experiments. *Journal of Applied Physics*, 117(23):233903, 2015.

[12] M. Amalvict. Absolute gravimetry at BIPM, sèvres (France), at the time of Dr. Akihiko Sakuma. In *Gravity, Geoid and Earth Observation*, pages 83–91. Springer, 2010.

[13] B. Arar, H. Wenzel, R. Güther, O. Brox, A. Maaßdorf, A. Wicht, G. Erbert, M. Weyers, G. Tränkle, H. Fernando, and A. Peters. Double-heterostructure ridge-waveguide GaAs/AlGaAs phase modulator for 780 nm lasers. *Applied Physics B*, 116(1):175–181, 2014.

[14] N. W. Ashcroft and N. D. Mermin. *Solid State Physics*. HBW international editions. Holt, Rinehart and Winston, 1976.

[15] M. M. Attallah, R. Jennings, X. Wang, and L. N. Carter. Additive manufacturing of Ni-based superalloys: The outstanding issues. *MRS Bulletin*, 41(10):758764, 2016.

[16] P. R. Berman. *Atom interferometry*. Academic press, USA, 1997.

[17] Y. Bidel, O. Carraz, R. Charrière, M. Cadoret, N. Zahzam, and A. Bresson. Compact cold atom gravimeter for field applications. *Applied Physics Letters*, 102(14):144107, 2013.

[18] C. J. Bordé. Atomic interferometry with internal state labelling. *Physics Letters A*, 140(1-2):10–12, 1989.

[19] C. J. Bordé, C. Salomon, S. Avrillier, A. Van Lerberghe, C. Bréant, D. Bassi, and G. Scoles. Optical ramsey fringes with traveling waves. *Physical Review A*, 30(4):1836, 1984.

[20] J. Bork, H. D. Hahlbohm, R. Klein, and A. Schnabel. The 8-layered magnetically shielded room of the PTB: Design and construction. In *Biomag2000, Proc. 12th Int. Conf. on Biomagnetism*, pages 970–73. Espoo, Finland, 2001.

[21] J. Bouman, M. Fuchs, E. V. Ivins, W. Wal, E. V. Schrama, P. N. A. M. Visser, and M. Horwath. Antarctic outlet glacier mass change resolved at basin scale from satellite gravity gradiometry. *Geophysical Research Letters*, 41(16):5919–5926, 2014.

[22] S. Branca, D. Carbone, and F. Greco. Intrusive mechanism of the 2002 NE-Rift eruption at Mt. Etna (Italy) inferred through continuous microgravity data and volcanological evidences. *Geophysical Research Letters*, 30(20), 2003.

[23] E. Calvo, M. Cerrada, I. Gil-Botella, C. Palomares, I. Rodríguez, F. Toral, and A. Verdugo. Passive magnetic cylindrical shielding at gauss-range static fields. *Nuclear Instruments and Methods in Physics Research Section A: Accelerators, Spectrometers, Detectors and Associated Equipment*, 600(3):560–567, Mar. 2009.

[24] M. V. Camp, O. de Viron, H. Scherneck, K. Hinzen, S. D. P. Williams, T. Lecocq, Y. Quinif, and T. Camelbeeck. Repeated absolute gravity measurements for monitoring slow intraplate vertical deformation in western Europe. *Journal of Geophysical Research: Solid Earth*, 116(B8).

[25] W. H. Campbell. *Introduction to geomagnetic fields*. Cambridge University Press, 2003.

[26] L. N. Carter, C. Martin, P. J. Withers, and M. M. Attallah. The influence of the laser scan strategy on grain structure and cracking behaviour in slm powder-bed fabricated nickel superalloy. *Journal of Alloys and Compounds*, 615:338 – 347, 2014.

[27] L. N. Carter, X. Wang, N. Read, R. Khan, M. Aristizabal, K. Essa, and M. M. Attallah. Process optimisation of selective laser melting using energy density model for nickel based superalloys. *Materials Science and Technology*, 32(7):657–661, 2016.

[28] S. Celozzi, G. Lovat, and R. Araneo. *Electromagnetic Shielding*. Wiley Online Library, 2008.

[29] R. Chang, A. L. Hoendervanger, Q. Bouton, Y. Fang, T. Klafka, K. Audo, A. Aspect, C. I. Westbrook, and D. Clément. Three-dimensional laser cooling at the Doppler limit. *Physical Review A*, 90(6):063407, 2014.

[30] D. X. Chen, J. A. Brug, and R. B. Goldfarb. Demagnetizing factors for cylinders. *IEEE Transactions on magnetics*, 27(4):3601–3619, 1991.

[31] M. F. Cheung. *Zero Magnetic Field Environment for EDM Measurement*. PhD thesis, University of Hong Kong, 2003.

[32] S. Chikazumi and C. D. Graham. *Physics of Ferromagnetism 2e*. Number 94. Oxford University Press on Demand, 2009.

[33] J. Coulomb. A methodology for the determination of global electromechanical quantities from a finite element analysis and its application to the evaluation of magnetic forces, torques and stiffness. *IEEE Transactions on Magnetics*, 19(6):2514–2519, 1983.

[34] J. Dalibard and C. Cohen-Tannoudji. Laser cooling below the Doppler limit by polarization gradients: simple theoretical models. *JOSA B*, 6(11):2023–2045, 1989.

[35] L. De-Sheng, Q. Qiu-Zhi, W. Bin, Z. Jian-Bo, L. Liang, and W. Yu-Zhu. Improvement on temperature measurement of cold atoms in a rubidium fountain. *Chinese Physics Letters*, 28(6):063201, 2011.

[36] S. Dickerson, J. M. Hogan, D. M. S. Johnson, T. Kovachy, A. Sugarbaker, S. W. Chiow, and M. A. Kasevich. A high-performance magnetic shield with large length-to-diameter ratio. *The Review of Scientific Instruments*, 83(6):065108, June 2012.

[37] S. M. Dickerson, J. M. Hogan, A. Sugarbaker, D. M. Johnson, and M. A. Kasevich. Multiaxis inertial sensing with long-time point source atom interferometry. *Physical review letters*, 111(8):083001, 2013.

[38] E. A. Donley, E. Hodby, L. Hollberg, and J. Kitching. Demonstration of high-performance compact magnetic shields for chip-scale atomic devices. *The Review of scientific instruments*, 78(8):083102, Aug. 2007.

[39] M. Dransfield and B. Milkereit. Airborne gravity gradiometry in the search for mineral deposits. In *Proceedings of exploration*, volume 7, pages 341–354, 2007.

[40] D. Dubbers. Simple formula for multiple mu-metal shields. *Nuclear Instruments and Methods in Physics Research Section A: Accelerators, Spectrometers, Detectors and Associated Equipment*, 243(2-3):511–517, 1986.

[41] G. Durin and S. Zapperi. Barkhausen noise in soft amorphous magnetic materials under applied stress. *Journal of Applied Physics*, 85(8):5196–5198, 1999.

[42] R. V. Eötvös. *Mathematische und naturwissenschaftliche berichte aus ungarn.* The presentation held at the Hungarian Academy of Sciences, 1890.

[43] A. Einstein. On the relativity principle and the conclusions drawn from it. Yearbook of radiactivity and electronics (in German). Cited after A. Einstein, L. Infeld. *The evolution of physics: from early concepts to relativity and quanta*, 1907.

[44] S. N. Erne, H. D. Hahlbohm, and H. Lübbig. Biomagnetism. In *Proceedings Third Int'l Workshop on Biomagnetism Berlin (West), pp. Title p.-137*, 1981.

[45] R. P. Feynman. Space-time approach to non-relativistic quantum mechanics. *Reviews of Modern Physics*, 20(2):367, 1948.

[46] J. B. Fixler, G. T. Foster, J. M. McGuirk, and M. A. Kasevich. Atom interferometer measurement of the Newtonian constant of gravity. *Science*, 315(5808):74–77, 2007.

[47] C. J. Foot. *Atomic physics*, volume 7. Oxford University Press, 2005.

[48] J. R. Gauger. Household appliance magnetic field survey. *IEEE Transactions on Power Apparatus and Systems*, (9):2435–2444, 1985.

[49] T. L. Gustavson, A. Landragin, and M. A. Kasevich. Rotation sensing with a dual atom-interferometer sagnac gyroscope. *Classical and Quantum Gravity*, 17(12):2385, 2000.

[50] K. I. Harakawa, G. Kajiwara, K. Kazami, H. Ogata, and H. Kado. Evaluation of a high-performance magnetically shielded room for biomagnetic measurement. *IEEE Transactions on Magnetics*, 32(6):5256–5260, 1996.

[51] P. Hariharan. *Basics of interferometry.* Academic Press, 2010.

[52] J. Hartwig, S. Abend, C. Schubert, D. Schlippert, H. Ahlers, K. Posso-Trujillo, N. Gaaloul, W. Ertmer, and E. M. Rasel. Testing the universality of free fall with rubidium and ytterbium in a very large baseline atom interferometer. *New Journal of Physics*, 17(3):035011, 2015.

[53] G. Hernández. *Fabry-perot interferometers*. Number 3. Cambridge University Press, 1988.

[54] A. Hinton. *Development of a Transportable Cold Atom Gradiometer*. PhD thesis, University of Birmingham, 2016.

[55] J. D. Jackson. *Classical Electrodynamics.*, volume 3. John Wiley & Sons, New York, 1998.

[56] Z. Ji, J. Yuan, Y. Zhao, X. Chang, and Y. Yang. Optimization and analysis of experimental parameters for polarization gradient cooling in optical molasses. *arXiv preprint arXiv:1304.7066*, 2013.

[57] J. M. Jin. *The Finite Element Method in Electromagnetics*. John Wiley & Sons, New York, 2015.

[58] M. Kasevich and S. Chu. Atomic interferometry using stimulated Raman transitions. *Physical Review Letters*, 67(2):181, 1991.

[59] M. Kasevich and S. Chu. Measurement of the gravitational acceleration of an atom with a light-pulse atom interferometer. *Applied Physics B*, 54(5):321–332, 1992.

[60] M. A. Kasevich. *Atom interferometry in an atomic fountain*. PhD thesis, Stanford University, 1992.

[61] K. Kato, K. Yamazaki, H. Matsuba, C. Sumi, and S. Sato. Active magnetic shield for biomagnetic measurements. In *Proc. of the 12th Int. Conf. on Biomagnetism*, pages 965–967. Citeseer, 2000.

[62] V. Kelha, J. Pukki, R. Peltonen, A. Penttinen, R. Ilmoniemi, and J. Heino. Design, construction, and performance of a large-volume magnetic shield. *IEEE Transactions on Magnetics*, 18(1):260–270, 1982.

[63] J. R. Kellogg, D. Schlippert, J. M. Kohel, R. J. Thompson, D. C. Aveline, and N. Yu. A compact high-efficiency cold atom beam source. *Applied Physics B*, 109(1):61–64, 2012.

[64] M. Kobayashi and Y. Ishikawa. Surface magnetic charge distributions and demagnetizing factors of circular cylinders. *IEEE Transactions on Magnetics*, 28(3):1810–1814, 1992.

[65] G. Lamporesi. *Determination of the gravitational constant by atom interferometry*. PhD thesis, Università Degli Studi di Firenze, 2006.

[66] J. Le Gouët, T. Mehlstäubler, J. Kim, S. Merlet, A. Clairon, A. Landragin, and F. P. Dos Santos. Limits to the sensitivity of a low noise compact atomic gravimeter. *Applied Physics B*, 92(2):133–144, 2008.

[67] M. Lederer. Accuracy of the relative gravity measurement. *Acta Geodyn. Geomater*, 6(3):155, 2009.

[68] E. W. Lee. Magnetostriction and magnetomechanical effects. *Reports on Progress in Physics*, 18(1):184, 1955.

[69] R. B. Li, L. Zhou, J. Wang, and M. S. Zhan. Measurement of the quadratic Zeeman shift of 85 Rb hyperfine sublevels using stimulated Raman transitions. *Optics Communications*, 282(7):1340–1344, 2009.

[70] J. O. Maclean, M. T. Greenaway, R. P. Campion, T. Pyragius, T. M. Fromhold, A. J. Kent, and C. J. Mellor. III-V semiconductor waveguides for photonic functionality at 780 nm. In *Integrated Optics: Devices, Materials, and Technologies XVIII*, volume 8988, page 898805. International Society for Optics and Photonics, 2014.

[71] A. Mager. Magnetic shielding efficiencies of cylindrical shells with axis parallel to the field. *Journal of Applied Physics*, 39(3):1914–1914, 1968.

[72] A. Mager. Magnetic shields. *IEEE Transactions on Magnetics*, 6(1):67–75, 1970.

[73] C. Mahadeswaraswamy. *Atom interferometric gravity gradiometer: Disturbance compensation and mobile gradiometry.* PhD thesis, University of Stanford, 2009.

[74] J. I. Malcolm. *Construction of a portable platform for cold atom interferometry.* PhD thesis, University of Birmingham, 2016.

[75] S. Malkowski, R. Adhikari, B. Hona, C. Mattie, D. Woods, H. Yan, and B. Plaster. Technique for high axial shielding factor performance of large-scale, thin, open-ended, cylindrical metglas magnetic shields. *Review of Scientific Instruments*, 82(7):075104, 2011.

[76] S. Malkowski, R. Y. Adhikari, J. Boissevain, C. Daurer, B. W. Filippone, B. Hona, B. Plaster, D. Woods, and H. Yan. Overlap Technique for End-Cap Seals on Cylindrical Magnetic Shields. *IEEE Transactions on Magnetics*, 49(1):651–653, Jan. 2013.

[77] H. Meier and C. H. Haberland. Experimental studies on selective laser melting of metallic parts. *Materialwissenschaft und Werkstofftechnik*, 39(9):665–670, 2008.

[78] S. Merlet, Q. Bodart, N. Malossi, A. Landragin, F. P. Dos Santos, O. Gitlein, and L. Timmen. Comparison between two mobile absolute gravimeters: optical versus atomic interferometers. *Metrologia*, 47(4):L9, 2010.

[79] S. Merlet, A. Kopaev, M. Diament, G. Geneves, A. Landragin, and F. P. D. Santos. Micro-gravity investigations for the LNE watt balance project. *Metrologia*, 45(3):265, 2008.

[80] H. J. Metcalf and P. Van der Straten. *Laser Cooling and Trapping.* Springer, New York, 1999.

[81] N. Metje, P. R. Atkins, M. J. Brennan, D. N. Chapman, H. M. Lim, J. Machell, J. M. Muggleton, S. Pennock, J. Ratcliffe, M. Redfern, and C. D. F. Rogers. Mapping the underworld–state-of-the-art review. *Tunnelling and underground space technology*, 22(5):568–586, 2007.

[82] A. A. Michelson and E. W. Morley. On the relative motion of the Earth and of the Luminiferous Ether. *Sidereal Messenger, vol. 6, pp. 306-310*, 6:306–310, 1887.

[83] C. V. Mikler, V. Chaudhary, T. Borkar, V. Soni, D. Choudhuri, R. Ramanujan, and R. Banerjee. Laser additive processing of Ni-Fe-V and Ni-Fe-Mo Permalloys: Microstructure and magnetic properties. *Materials Letters*, 192:9–11, 2017.

[84] J. Müller, M. Naeimi, O. Gitlein, L. Timmen, and H. Denker. A land uplift model in fennoscandia combining grace and absolute gravimetry data. *Physics and Chemistry of the Earth, Parts A/B/C*, 53:54–60, 2012.

[85] K. Nagashima, I. Sasada, and K. Tashiro. High-performance bench-top cylindrical magnetic shield with magnetic shaking enhancement. *IEEE Transactions on Magnetics*, 38(5):3335–3337, 2002.

[86] A. Niggebaum. *Towards mobile quantum sensors for gravity surveys.* PhD thesis, University of Birmingham, 2016.

[87] E. Paperno, H. Koide, and I. Sasada. A new estimation of the axial shielding factors for multishell cylindrical shields. *Journal of Applied Physics*, 87(9):5959–5961, 2000.

[88] E. Paperno, S. Peliwal, M. V. Romalis, and A. Plotkin. Optimum shell separation for closed axial cylindrical magnetic shields. *Journal of Applied Physics*, 97(10):10Q104, 2005.

[89] E. Paperno, M. V. Romalis, and Y. Noam. Optimization of five-shell axial magnetic shields having openings in the end-caps. *IEEE Transactions on Magnetics*, 40(4):2170–2172, 2004.

[90] E. Paperno, I. Sasada, and K. Tashiro. Shielding Equation. 38(5):3324–3326, 2002.

[91] L. L. Parimi. Additive manufacturing of nickel based superalloys for aerospace applications. Embargo expiry:30/04/2018, July 2014.

[92] A. Peters, K. Y. Chung, and S. Chu. Measurement of gravitational acceleration by dropping atoms. *Nature*, 400(6747):849–852, 1999.

[93] A. Peters, K. Y. Chung, and S. Chu. High-precision gravity measurements using atom interferometry. *Metrologia*, 38(1):25, 2001.

[94] W. D. Phillips and H. Metcalf. Laser deceleration of an atomic beam. *Physical Review Letters*, 48(9):596, 1982.

[95] A. Pinkerton, J. Shackleton, R. Moat, L. Li, P. Withers, M. Preuss, J. Allen, P. Hilton, and R. Folwell. The effect of process parameters on residual stresses within an inconel 718 part produced by the direct laser deposition process. 2005.

[96] C. Qiu, C. Panwisawas, M. Ward, H. C. Basoalto, J. W. Brooks, and M. M. Attallah. On the role of melt flow into the surface structure and porosity development during selective laser melting. *Acta Materialia*, 96:72 – 79, 2015.

[97] J. Ramirez-Serrano, N. Yu, J. M. Kohel, J. R. Kellogg, and L. Maleki. Multistage two-dimensional magneto-optical trap as a compact cold atom beam source. *Optics letters*, 31(6):682–684, 2006.

[98] T. Rikitake. *Magnetic and Electromagnetic Shielding*. Springer, New York, 1987.

[99] G. Rosi, F. Sorrentino, L. Cacciapuoti, M. Prevedelli, and G. M. Tino. Precision measurement of the Newtonian gravitational constant using cold atoms. *Nature*, 510(7506):518–521, 2014.

[100] R. Rummel. Geoid and gravity in Earth sciences–an overview. *Earth, Moon, and Planets*, 94(1-2):3–11, 2004.

[101] M. Schmidt. *A mobile high-precision gravimeter based on atom interferometry*. PhD thesis, Humboldt-Universitt zu Berlin, 2011.

[102] M. Schmidt, A. Senger, M. Hauth, C. Freier, V. Schkolnik, and A. Peters. A mobile high-precision absolute gravimeter based on atom interferometry. *Gyroscopy and Navigation*, 2(3):170–177, 2011.

[103] F. Schweizer. Magnetic shielding factors of a system of concentric spherical shells. *Journal of Applied Physics*, 33(3), 1962.

[104] I. I. Shapiro, C. C. Counselman III, and R. W. King. Verification of the principle of equivalence for massive bodies. *Physical Review Letters*, 36(11):555, 1976.

[105] J. H. Shirley. Modulation transfer processes in optical heterodyne saturation spectroscopy. *Optics Letters*, 7(11):537–539, 1982.

[106] I. Shishkovsky and V. Saphronov. Peculiarities of selective laser melting process for permalloy powder. *Materials Letters*, 171:208–211, 2016.

[107] I. V. Shishkovsky, A. P. Nazarov, D. V. Kotoban, and N. G. Kakovkina. Comparison of additive technologies for gradient aerospace part fabrication from nickel-based superalloys. *Superalloys. InTech Publ*, pages 221–245, 2015.

[108] E. Smith. Calculations of magnetic shield effectiveness for long μ-metal cylinders.

[109] D. J. Snee. Effects of composition and cooling rate on the initial permeability of mumetal. *Journal of Applied Physics*, 38(3):1172–1173, 1967.

[110] F. Sorrentino, Q. Bodart, L. Cacciapuoti, Y. H. Lien, M. Prevedelli, G. Rosi, L. Salvi, and G. M. Tino. Sensitivity limits of a Raman atom interferometer as a gravity gradiometer. *Physical Review A*, 89(2):023607, 2014.

[111] A. M. Steane, M. Chowdhury, and C. J. Foot. Radiation force in the magneto-optical trap. *J. Opt. Soc. Am. B*, 9(12):2142–2158, Dec 1992.

[112] D. A. Steck. Rubidium 87 D Line Data. available online at http://steck.us/alkalidata (revision 2.1.5, 13 January 2015). Accessed: 15-05-2015.

[113] T. Stephen and P. Jonathan. UK Quantum Technology Landscape 2016. http://uknqt.epsrc.ac.uk/resources/publications/. Accessed: 15-03-2018.

[114] T. Sterne. Multi-lamellar cylindrical magnetic shields. *Review of Scientific Instruments*, 6(10):324–326, 1935.

[115] A. Sugarbaker. *Atom interferometry in a 10-m fountain.* PhD thesis, Stanford University, 2014.

[116] A. Sugarbaker, S. M. Dickerson, J. M. Hogan, D. M. S. Johnson, and M. A. Kasevich. Enhanced atom interferometer readout through the application of phase shear. *Physical Review Letters*, 111(11):113002, 2013.

[117] T. J. Sumner, J. M. Pendlebury, and K. F. Smith. Convectional magnetic shielding. *Journal of Physics D: Applied Physics*, 20(9):1095, 1987.

[118] H. J. M. Ter Brake, H. J. Wieringa, and H. Rogalla. Improvement of the performance of a mu-metal magnetically shielded room by means of active compensation (biomagnetic applications). *Measurement Science and Technology*, 2(7):596, 1991.

[119] F. Thiel. Demagnetization of Layered Ferromagnetic Structures for Magnetically Shielding : Frequency Considerations. *IEEE Transactions on Magnets*, 45(12):5307–5314, 2009.

[120] F. Thiel, A. Schnabel, S. Knappe-Grüneberg, D. Stollfuß, and M. Burghoff. Demagnetization of magnetically shielded rooms. *Review of Scientific Instruments*, 78(3):035106, 2007.

[121] X. C. Tong. *Advanced materials and design for electromagnetic interference shielding.* CRC press, 2016.

[122] J. Voigt, S. Knappe-Grüneberg, A. Schnabel, R. Körber, and M. Burghoff. Measures to reduce the residual field and field gradient inside a magnetically shielded room by a factor of more than 10. *Metrology and Measurement Systems*, 20(2):239–248, 2013.

[123] D. Von Lindenfels, M. Wiesel, D. A. Glazov, A. V. Volotka, M. M. Sokolov, V. M. Shabaev, G. Plunien, W. Quint, G. Birkl, A. Martin, and M. Vogel. Experimental access to higher-order Zeeman effects by precision spectroscopy of highly charged ions in a Penning trap. *Physical Review A*, 87(2):023412, 2013.

[124] B. Vrancken, V. Cain, R. Knutsen, and J. Van Humbeeck. Residual stress via the contour method in compact tension specimens produced via selective laser melting. *Scripta Materialia*, 87:29–32, 2014.

[125] W. G. Wadey. Magnetic shielding with multiple cylindrical shells. *Review of Scientific Instruments*, 27(11):910–916, 1956.

[126] B. Wu, Z. Wang, B. Cheng, Q. Wang, A. Xu, and Q. Lin. The investigation of a μGal-level cold atom gravimeter for field applications. *Metrologia*, 51(5):452, 2014.

[127] X. Wu. *Gravity gradient survey with a mobile atom interferometer*. PhD thesis, Stanford University, 2009.

[128] V. V. Yashchuk and E. Paperno. Magnetic shielding. In D. Budker and D. F. J. Kimball, editors, *Optical Magnetometry*, pages 104–124. Cambridge University Press, New York, 2013.

[129] K. P. Zetie, S. F. Adams, and R. M. Tocknell. How does a Mach-Zehnder interferometer work? *Physics Education*, 35(1):46, 2000.

[130] L. Zhou, Z. Y. Xiong, W. Yang, B. Tang, W. C. Peng, K. Hao, R. B. Li, M. Liu, J. Wang, and M. S. Zhan. Development of an atom gravimeter and status of the 10-meter atom interferometer for precision gravity measurement. *General Relativity and Gravitation*, 43(7):1931–1942, 2011.